

Characterization of Murine Astrocyte Cultures in 3D Hydrogel Matrices

An Approach to Nuclei Segmentation and Assisted Cell Classification

Maria Beatriz Sereno Fernandes

Thesis to obtain the Master of Science Degree in

Biomedical Engineering

Supervisors: Prof. Rui Miguel Carrasqueiro Henriques
Dr. Thomas Distler

Examination Committee

Chairperson: Prof. João Miguel Raposo Sanches
Supervisor: Prof. Rui Miguel Carrasqueiro Henriques
Member of the Committee: Prof. Daniel Pedro de Jesus Faria

March 2025

Declaration

I declare that this document is an original work of my own authorship and that it fulfills all the requirements of the Code of Conduct and Good Practices of the Universidade de Lisboa.

Acknowledgments

I would like to express my deepest gratitude to my family. Your unwavering support and love have been a constant throughout my life. You have taught me to endure challenges and always come through. Everything I am is a reflection of all your hard work and the result of what you inspire me to be. None of this would have been possible without you.

Namely, I would like to thank my father, whose introduction to Rammstein drove me to Germany 20 years later and made me fall in love with German culture. My mother, who always presents me with the simplest solutions for my most complex problems. We all know you're my guiding light. My sister, for being my equal, understanding me like no other, and giving me all the sweetness I need in my life. My avó Zé, who gives me the confidence to pursue everything I desire. And, lastly, my avó Gina, who has always been in my heart and is the source of my strength. Thank you for your resilience; I know it hasn't been an easy journey.

To the wonderful friends I made in Munich: To Kathi, whose companionship started at the workbench and went far beyond. You have been there through thick and thin since day one, and I'm so grateful to have you as a friend. To Deepti, whose light soul inspired me, gave me motivation whenever I doubted, and made me admire the bright side of problems. To Deniz, my desk mate, who kickstarted my days with the best mood and with whom I could talk in a language only a few understood. To Alp, Merle, and Vasiliki, whose unparalleled spirits are a breath of fresh air every day. And last but not least, to Olli, who gave me strength whenever I wavered, opened my eyes when I lacked vision, always believed in me, and shared my happiness and anguish. Thank you for standing beside me every day, for being my safe space, and making me feel at home.

Lastly, to Dr. Magdalena Götz, who welcomed me into her laboratory for the realization of this project. To Dr. Giacomo Masserdotti and Dr. Thomas Distler for their scientific expertise and support. To Dr. Rui Henriques, whose guidance and expertise have been instrumental in the successful completion of this thesis, and whose positivity and mentorship were invaluable. And to Dr. Amirhossein Kardoost for his collaboration in the development of the GUI.

Thank you all for playing a part in this journey and in this chapter of my life. I look forward to continuing to share adventures and challenges with you.

Abstract

Three-dimensional (3D) cultures in hydrogel matrices provide a promising platform for studying astrocyte biology and advancing cell therapy applications as they can partially mimic the 3D environment found in the brain tissue. Nevertheless, further refinement and characterization are necessary to advance hydrogel platforms for astrocyte cultures. This study combines experimental and computational approaches to characterize postnatal murine astrocyte cultures in 3D alginate- and fibrin-based hydrogels. Experimentally, various hydrogel platforms, such as alginate, fibrin and fibrin-alginate composites, were evaluated for cell viability, morphology and astrocytic marker expression. Fibrin-alginate hydrogels crosslinked with 100 mM CaCl₂ were found to hold promising cell profiles, presenting a mean percentage of ramified cells exceeding 70%, 87% of SOX9⁺ cells and 89% of GFAP⁺/SOX9⁺ cells. Computationally, a 3D nuclei segmentation deep learning model was implemented using nnU-Net. Robust performance across diverse hydrogel-based datasets with error rates below 5% was achieved. Limited functionality was found for nuclei segmentation on tissue sample datasets with high cell density. To streamline data analysis and processing, a graphical user interface was developed enabling automatic nuclei detection and multi-label cell classification of z-stack microscopy images. This tool reduces manual effort on biological image analysis and enables the generation of classification datasets. The developed computational tools are specifically designed for astrocyte culturing in hydrogel matrices. Nevertheless, this project underscores the value of integrating computational tools for automated neural tissue profiling, contributing to downstream applications in neuroscience, regenerative medicine, and tissue engineering.

Keywords

3D astrocyte cultures, nuclei segmentation, deep learning, fibrin-alginate hydrogels, biological image analysis

Resumo

Culturas tridimensionais (3D) em hidrogéis são uma plataforma promissora para estudar astrócitos e avançar em terapia celular, mimetizando parcialmente o ambiente cerebral. No entanto, a otimização destas culturas requer caracterização detalhada. Este estudo combina abordagens experimentais e computacionais para caracterizar astrócitos de murinos pós-natais em hidrogéis de alginato e fibrina. Experimentalmente foram testados hidrogéis de alginato, fibrina e compósitos de fibrina-alginato, avaliando viabilidade celular, morfologia e expressão de marcadores. Hidrogéis de fibrina-alginato reticulados com 100 mM de CaCl₂ apresentaram perfis celulares promissores, com mais de 70% de células ramificadas, 87% de células SOX9⁺ e 89% de células GFAP^{+/SOX9⁺. Computacionalmente, foi implementado um modelo de aprendizagem profunda utilizando o nnU-Net para segmentação 3D de núcleos, com erro inferior a 5% em hidrogéis. No entanto, teve desempenho limitado em tecidos de alta densidade celular. Para otimizar a análise, foi criada uma interface gráfica para deteção automática de núcleos e classificação de células em imagens de microscopia z-stack, reduzindo o esforço manual e facilitando a geração de dados. As ferramentas computacionais desenvolvidas foram concebidas para culturas de astrócitos em hidrogéis. No entanto este projeto realça a importância da integração computacional na caracterização automatizada de tecidos neurais, contribuindo para a neurociência, medicina regenerativa e engenharia de tecidos}

Palavras Chave

culturas 3D de astrócitos, segmentação de núcleos, aprendizagem profunda, hidrogéis fibrina-alginato, análise de imagens biológicas

Contents

1	Introduction	1
1.1	Motivation	2
1.2	Research Objectives and Outcomes	3
1.3	Thesis Outline	4
2	Background and Theoretical Foundations	5
2.1	Astrocytes and Cell Culture in 3D Hydrogels	6
2.1.1	Astrocytes in Brain Function and Response to Disease	6
2.1.2	Astrocytes as Therapeutic Agents	9
2.1.3	3D Cell Cultures and Their Advantages	10
2.2	Foundations and Theoretical Concepts of Machine Learning	13
2.2.1	Core Mathematical Concepts in Machine Learning	13
2.2.2	Convolutional Neural Networks	18
2.2.3	Evaluation Metrics in Supervised Learning Settings	21
2.2.4	Data Augmentation, Transfer Learning and Fine-Tuning	23
3	State-of-the-Art Deep Learning Approaches in Biomedical Image Analysis	25
3.1	Deep Learning for Biomedical Imaging	26
3.2	Foundations of Computer Vision Tasks	27
3.2.1	Image Classification	28
3.2.2	Object Detection	29
3.2.3	Image Segmentation	31
4	Materials and Methods for Cell Culturing and Profiling	35
4.1	Primary Cultures of Mouse Cortical Astrocytes	36
4.2	Cell Cultures	36
4.2.1	2D Cell Cultures	36
4.2.2	Cell Embedding in 3D Sodium Alginate Hydrogels	36
4.2.3	Cell Embedding in 3D FibrinVLG and Fibrin Hydrogels	37
4.3	Cell Culture Characterization	37

4.3.1	Immunocytochemistry	37
4.3.2	LIVE/DEAD Viability Assay	38
4.3.3	Confocal Imaging of 3D Astrocyte Cultures	38
4.3.4	Cell Morphology and Markers Expression Quantification	38
5	Computational Solution for 3D Cell Culture Characterization	39
5.1	Deep Learning for Nuclei Segmentation	40
5.1.1	Baseline Solution	40
5.1.2	Improved Solution	44
5.2	GUI for 3D Cell Culture Image Annotation	51
5.2.1	Automatic Identification of Nuclei	53
5.2.2	Cell Labelling	54
5.3	Deep Learning for Cell Classification	55
6	Experimental Results	57
6.1	Cell Morphology and Astrocytic Markers Expression in Alginate and Fibrin-Alginate Hydrogels	58
6.2	Effects of CaCl_2 Crosslinking Concentrations on Cell Viability	62
6.3	Effects of CaCl_2 Crosslinking Concentrations on Cell Morphology and Astrocytic Markers Expression	64
7	Discussion	69
7.1	Discussion of the Computational Solutions	70
7.2	Discussion of the Experimental Results	74
8	Conclusion	77
8.1	Conclusions	78
8.2	Limitations and Future Work	79
Bibliography		81
A Key Resources Table		A1
B Additional Methods		B3
B.1	PDL Coating	B3
B.2	Fabrication of Glass-bottom Silicone Mini-wells	B4
C GUI User Guide		C5
C.1	Instalation	C6
C.2	Usage	C6
C.3	Shortcuts	C7

D Additional Methods for Nuclei Segmentation	D9
D.1 Dataset Processing and Annotation for Baseline Solution	D9
D.1.1 Image Processing using Fiji	D9
D.1.2 2D Nuclei Segmentation	D11
D.2 3D Nuclei Segmentation and Preparation for nnU-Net Input	D13

x

List of Figures

2.1	Scheme summarizing main astrocytic features and functions	7
2.2	Morphological features of astrocytes in the CNS.	8
2.3	Conformation monomers and blocks distribution of alginate polyssacharide.	11
2.4	Alginate hydrogel properties on crosslinking with calcium chloride and RGD peptide motif coupling.	12
2.5	Scanning electron micrograph of human fibrinogen.	12
3.1	A look into computer vision tasks of classification, object detection and image segmentation in the context of astrocyte culture characterization.	27
5.1	Summary and visualization of the performance of the tested models and architectures for two-dimensional (2D) nuclei segmentation.	44
5.2	Shapiro test analysis on datasets regarding mean standard deviation of image intensity. .	46
5.3	Comparison of nnU-Net, Stardist 3D and Cellstitch for 3D nuclei segmentation.	47
5.4	Comparison of nnU-Net models trained on different datasets regarding different performance metrics.	48
5.5	<i>T</i> -test statistics heatmaps comparing the performance of various nnU-Net segmentation models.	49
5.6	Maximum intensity projections of 12 μm in depth of exemplary images of each validation dataset.	51
5.7	Values of the <i>PR</i> across the different testing datasets using <i>model 5</i> as predictor.	51
5.8	Representation of the GUI's main window.	52
5.9	Representation of the GUI's main window with an image loaded and bounding boxes drawn.	53
5.10	Representation of the GUI's <i>Bounding Boxes</i> window.	54
5.11	Merging of cell features of image classification.	56
6.1	Illustrative procedure for the study of morphology and markers expression of astrocytes in alginate and alginate-fibrous hydrogels.	59

6.2 Qualitative analysis of MVG, VLVG and FibrinVLVG hydrogels.	60
6.3 Morphological cell analysis of MVG, VLVG and FibrinVLVG hydrogels.	61
6.4 Distribution of cell population regarding GFAP and SOX9 markers expression, in VLVG and FibrinVLVG hydrogels, and PDL cultures after 7 DIV.	62
6.5 Illustrative procedure for the study of cell viability in VLVG and FibrinVLVG hydrogels crosslinked with different concentrations of CaCl_2	62
6.6 Astrocytic markers expression characterization and classification based on viability markers.	63
6.7 Viability essay analysis on VLVG and FibrinVLVG hydrogels crosslinked with 5 mM, 50 mM, 100 mM, and 175 mM of Ca^{2+} , comparing to monolayer cell cultures of PDL coated coverslips. The error bars indicate the standard deviation for each viability state, centered on the corresponding mean.	64
6.8 Illustrative procedure for the study of cell morphology and astrocytic markers expression in Fibrin and FibrinVLVG hydrgels crosslinked with different concentrations of CaCl_2	65
6.9 Cell morphology analysis in Fibrin and FibrinVLVG hydrogels.	66
6.10 Astrocytic markers expression analysis on Fibrin and FibrinVLVG hydrogels crosslinked with 5 mM, 50 mM, 100 mM, and 175 mM of Ca^{2+} , comparing to monolayer cell cultures of PDL coated coverslips.	66
6.11 Correlation between morphology and astrocytic markers expression analysis on Fibrin and FibrinVLVG hydrogels crosslinked with 5 mM, 50 mM, 100 mM, and 175 mM of Ca^{2+}	67
B.1 Technical drawing of mini-well construction.	B4
D.1 Fiji preprocessing.	D11
D.2 2D nuclei profiling and statistics.	D12

List of Tables

3.1	Summary of the most common deep neural networks used for computer vision tasks in biological image analysis.	34
4.1	Composition of thrombin and fibrinogen solutions for Fibrin and FibrinVLG hydrogels casting.	37
5.1	Segmentation Mask R-CNN models.	42
5.2	Summary of the 2D nuclei segmentation models performance.	43
5.3	Validation of the architectures performance for 2D nuclei segmentation.	43
5.4	Depiction of the datasets generated for nnU-Net model optimization.	45
5.5	Scoring of trained nnU-Net models following a ranking system of each of the evaluation metrics.	49
5.6	nnU-Net testing datasets, spanning from cultures in hydrogels and murine tissue samples, accross different FOV and anisotropies.	50
A.1	Complete list of materials and chemicals.	A1
C.1	Comparison of the features in <i>GUI v1.0</i> and <i>GUI v2.0</i>	C5
C.2	Shortcuts for <i>GUI v1.0</i> and <i>GUI v2.0</i>	C8
D.1	Annotation and description of the secondary datasets.	D12

Acronyms

2D	two-dimensional
3D	three-dimensional
AD	Alzheimer's disease
AI	artificial intelligence
AF	alexa fluor
Aldh1L1	aldehyde dehydrogenase 1 family member L1
ALS	amyotrophic lateral sclerosis
ANN	artificial neural networks
AR	aggregation ratio
BBB	blood brain barrier
BSA	bovine serum albumin
CNN	convolutional neural networks
CNS	central nervous system
CT	X-ray computed tomography
DAPI	4',6-diamidino-2-phenylindole
DC	Dice coefficient
DSB2018	nuclear detection challenge 2018
DIV	days in vitro
DL	deep learning
ECM	extracellular matrix
EM	electron microscopy
FACS	fluorescent-activated cell sorting
FBS	fetal bovine serum

FOV	field of view
FN	false negative
FP	false positive
FM	fluorescence microscopy
FCN	fully connected networks
GFAP	glial fibrillary acidic protein
GFP	green fluorescent protein
GM	gray matter
GUI	graphical user interface
GPU	graphics processing unit
HA	hyaluronic acid
hBranched	highly branched
hiPSCs	human iPSCs
IoU	intersection over union
iPSC	induced pluripotent stem cells
LM	light microscopy
MAE	mean absolute error
mAP	mean average precision
ML	machine learning
MSE	mean squared error
MVG	medium viscosity grade
MRI	magnetic resonance imaging
NSCs	neural stem cells
PA	polyacrylamid
PCA	principal component analysis
PD	Parkinson's disease
PDL	poly-D-lysine
PEG	polyethylene glycol
PET	positron emission tomography

PFA	paraformaldehyde
P/S	penicillin–streptomycin
PR	prediction ratio
PI	propidium iodide
p5-7	postnatal day 5-7
ReLU	rectifier linear unit
RGD	arginylglycylaspartic acid
RMSE	root mean squared error
RT	room temperature
ResNet	residual networks
RPN	region proposal network
R-CNN	recursive convolutional neural network
SGD	stochastic gradient descent
SSE	sum of squared residual errors
SOX9	SRY (sex determining region Y)-box transcription factor 9
SVM	support vector machines
SPM	scanning probe microscopy
TP	true positive
VLVG	very low viscosity grade
VGG	very deep convolutional networks
FibrinVLVG	VLVG sodium alginate-fibrin
WT	wild type
YOLO	You Only Look Once

1

Introduction

Contents

1.1 Motivation	2
1.2 Research Objectives and Outcomes	3
1.3 Thesis Outline	4

1. INTRODUCTION

1.1 Motivation

Neurogenesis, the process by which new functional neurons are generated in the brain, while well-established in embryonic development, has garnered renewed interest since the recognition of its occurrence in the adult mammalian brain in the 1990s [1, 2]. Specifically, neurogenesis has been discovered to occur in two particular niches of the adult mammalian brain: the subventricular zone [3, 4] and subgranular zone of the hippocampal dentate gyrus [5, 6]. This pivotal discovery has shifted perspectives on brain plasticity, raising the potential for therapeutic applications in contexts such as injury, neurodegenerative diseases, and cognitive decline. Despite significant advances over the last years, the underlying mechanisms of neurogenesis remain insufficiently understood and present a key area of ongoing research [7].

Traditionally, neuroscience research has been predominantly centered on the study of neurons – the essential nervous system units responsible for transmitting messages throughout the body via chemical or electrical signals [8]. However, glial cells – historically regarded as mere supportive elements – have received increasing interest in modern research [9, 10]. Glial cells are now recognized as active contributors to the brain's homeostasis and plasticity, playing crucial roles in maintaining brain function, responding to trauma and in neurogenesis [11]. In particular, astrocytes – the most prominent glial cell type in the brain [12] – in addition to originating from neural stem cells (NSCs), similarly to neurons, have been shown to play critical roles in stress responses to neurodegeneration and brain injury [13, 14].

On the other hand, direct cell reprogramming, first demonstrated in vitro by [15], is the process by which a fully differentiated cell can be converted into a different cell fate without going through an intermediary pluripotent state. Thus, direct neural reprogramming refers to the process by which a fully differentiated cell can be converted into a neuron. This achievement was first accomplished in vitro through the induction of transcription factor PAX6 re-expression in postnatal astrocytes [16]. Direct neural reprogramming of astrocytes was further demonstrated in vivo [17], underscoring their potential as a viable therapeutic source for neuronal replacement in degenerative conditions and brain trauma [18]. However, fully harnessing the therapeutic potential of astrocytes as a source for replacing neurons requires a deeper understanding of the heterogeneity and complexity of this cell population [19].

To effectively study these complex intricacies, in vitro models must be optimized to closely replicate the cellular microenvironment of in vivo systems. Conventional two-dimensional (2D) or monolayer models often fall short in mimicking the complex architecture of the brain, leading to significant alterations in cell morphology and behavior that compromise the reliability of experimental data in reflecting in vivo conditions [20]. Recent advancements in three-dimensional (3D) culture systems, both scaffold-free and scaffold-based, have shown promise in offering more physiologically relevant models and an appealing alternative to animal models [21, 22]. Among these, hydrogels stand out, as they provide a biomimetic environment that better supports cellular dynamics, closely resembling the in vivo [23].

Hydrogel-based scaffolds consist of interconnected networks of polymers, either synthetic or naturally derived, capable of retaining large amounts of water [24]. This water-rich structure facilitates the exchange of nutrients and signaling molecules within the culture environment. In addition, their high versatility, that enables precise tuning of their physical and chemical properties, allows hydrogels to emulate extracellular matrix (ECM) structures across diverse *in vivo*-like tissues [25]. Synthetic polymer-based hydrogels offer fine control over the physical characteristics of the scaffold, while natural polymers and its functionalization provide essential biological cues that support cell attachment and model behavior [26]. In certain applications, hybrid hydrogels, combining synthetic and natural components, offer a dynamic solution for more accurate ECM modelling, demonstrating clear advantages over monolayer culture systems [27].

Despite the promising potential of hydrogel-based 3D culture systems, there remains a critical need for their comprehensive evaluation, particularly regarding their impact on cell behavior. Optimizing these scaffolds is a complex task, requiring attention to multiple interdependent conditions. Given the versatility of hydrogels, the parameters subjected to optimization are vast and varied [28].

The primary indicator of a hydrogel's effectiveness in mimicking the *in vivo* environment is the morphological response of cells when exposed to the scaffold's physicochemical cues. In the context of evaluating astrocytes for potential use in neuronal replacement therapies, assessing their morphology should be the initial step of the candidate system's evaluation. Studies on gene expression patterns and cell or tissue functional assays establish further validation of the scaffolds. Given the high heterogeneity and morphological complexity of astrocyte populations, several researchers have emphasized the importance of automated approaches, specifically using machine learning (ML) and deep learning (DL), for accurate astrocyte characterization [29, 30]. However, these methods face significant challenges due to the scarcity of annotated data, especially in 3D cell culture or tissue datasets, which hampers the generalization and robustness of ML algorithms in this context.

These challenges, coupled with the clear advantages that automated and versatile analysis of 3D cell cultures could offer to biological research, have driven significant interest among researchers in developing generalized tools for astrocyte culture image analysis [30]. Addressing this need is the central focus of this work. By providing insights of a flexible, automated tool for the characterization of astrocyte cultures, this project aims to accelerate the optimization of hydrogel-based cell culture systems, ultimately advancing their application in neuroscience and regenerative medicine.

1.2 Research Objectives and Outcomes

This project is divided into computational and experimental objectives. On the **computational side**, the key objectives were to **(1)** develop an approach for a high-throughput analysis pipeline tailored for the characterization of 3D hydrogel-based astrocyte cultures, and **(2)** develop a user-friendly graphical user

1. INTRODUCTION

interface (GUI) for culture annotation. On the **experimental side**, the key objectives were to **(1)** test different 3D hydrogel platforms for murine astrocyte culture, validating the matrices qualitatively and regarding cell morphology and astrocytic marker expression, and **(2)** test the effects of different calcium chloride crosslinking concentrations on cell viability, morphology and astrocytic marker expression.

Specifically, to tackle the first objective of the computational work, this project introduces an automated approach for cell detection in 3D murine astrocyte cultures embedded in hydrogel matrices, leveraging nuclei segmentation through DL models. Additionally, a framework has been established for the automated classification of astrocytes based on several key criteria: morphological features (e.g., round, branched, or highly branched), interactions with the environment (e.g., single cells or cell clusters), and marker expression patterns, focusing on the expression of SRY (sex determining region Y)-box transcription factor 9 (SOX9) and glial fibrillary acidic protein (GFAP).

Furthermore, the GUI was designed to enable biologists to efficiently annotate 3D fluorescent confocal images. This tool facilitates automatic identification of cell nuclei and supports cell-specific multi-labeling, while prioritizing ease of use and accessibility compared to the annotation tools of traditional biological image software, such as Fiji [31] and Imaris [32]. The tool's dual functionality allows for intuitive manual dataset annotation while streamlining statistical data analysis and the extraction of classification datasets for subsequent DL model training.

On the experimental side, murine-derived astrocytes were cultured on medium viscosity grade (MVG) and very low viscosity grade (VLVG) sodium alginate, pure fibrin, and VLVG sodium alginate-fibrin (FibrinVLVG) composite hydrogels, using poly-D-lysine (PDL) coated glass cover-slips as a control. Furthermore, 5 mM, 50 mM, 100 mM and 175 mM calcium chloride cross-linking concentrations were tested on FibrinVLVG hydrogels to assess impact on cell viability. Immunocytochemistry assays with GFAP, SOX9, and DAPI stainings were conducted for morphological and marker expression characterization.

1.3 Thesis Outline

This work is organized into eight chapters. Chapter 1 presents the motivation and objectives. Chapter 2 covers foundational background concepts and literature review, while Chapter 3 dives in greater detail into the most recent advances in deep learning for biological image analysis. Chapter 4 describes the materials and methods for analyzing hydrogel cell cultures. Chapter 5 details and validates the computational tools developed. Chapter 6 analyzes the experimental results. Chapter 7 discusses the results, and chapter 8 summarizes the conclusions and outlines future directions.

2

Background and Theoretical Foundations

Contents

2.1 Astrocytes and Cell Culture in 3D Hydrogels	6
2.2 Foundations and Theoretical Concepts of Machine Learning	13

2. BACKGROUND AND THEORETICAL FOUNDATIONS

This chapter explores the key concepts and state-of-the-art advancements that form the foundation of this project and drive its research objectives. Beginning with the cellular model and culture conditions, Section 2.1 examines the critical role of astrocytes in brain function, their responses to disease, and the groundbreaking developments in direct reprogramming into neurons, along with their potential applications as therapeutic agents. We will also address the limitations of modeling cellular structures in 2D environments and highlight the promise of hydrogels as innovative 3D cell culture platforms.

Section 2.2 explores the fundamental concepts of modern machine learning, its significance in the biomedical field, key evaluation metrics for supervised learning in computer vision tasks, and strategies to address data scarcity.

2.1 Astrocytes and Cell Culture in 3D Hydrogels

2.1.1 Astrocytes in Brain Function and Response to Disease

The brain, the powerhouse of the central nervous system (CNS), orchestrates everything from processing environmental stimuli to controlling bodily functions, while shaping our thoughts, emotions, and consciousness. At its core, two key players drive its operations: neurons and glial cells.

Neurons, the cells responsible for transmitting signals and triggering actions through depolarization across a vast, interconnected network [8], have long been the focus of research into behavior and disease. However, modern neuroscience increasingly has increasingly recognized glial cells as essential contributors to brain function and health [9, 10]. Far beyond providing mere structural support to neurons, glial cells play dynamic roles in maintaining proper brain activity [13, 14].

In the CNS, glial cells include oligodendrocytes, astrocytes, microglia, and ependymal cells. Although previous studies have believed these cells collectively outnumbered neurons in a ratio of 10:1 [33], more recent studies show this ratio is closer to 1:1, with region-specific differences [34]. Glial cells perform indispensable functions such as regulating metabolism, providing immune defense, maintaining the ECM, and modulating neural activity. Glial cells are now understood to be pivotal for the brain's performance, resilience, and overall health [8].

Among glial cells, astrocytes are particularly renowned for their diversity [12], extensive networking properties [35], critical interactions with the blood brain barrier (BBB) [36, 37], being associated with several diseases – such as Alzheimer's disease (AD) [38] and Parkinson's disease (PD) [39] – and presenting promising therapeutic potential [40, 41], as highlighted in Figure 2.1. In healthy conditions, astrocytes display a morphology characterized by fine, elongated processes – hereon also referred to as branches – that extend from the soma. Astrocytes are broadly distinguished by their morphological features into two classes: protoplasmic and fibrous astrocytes (Figure 2.2). Protoplasmic astrocytes, more prominent in the gray matter (GM), have a more irregular, bushy-like structure with intricate branching,

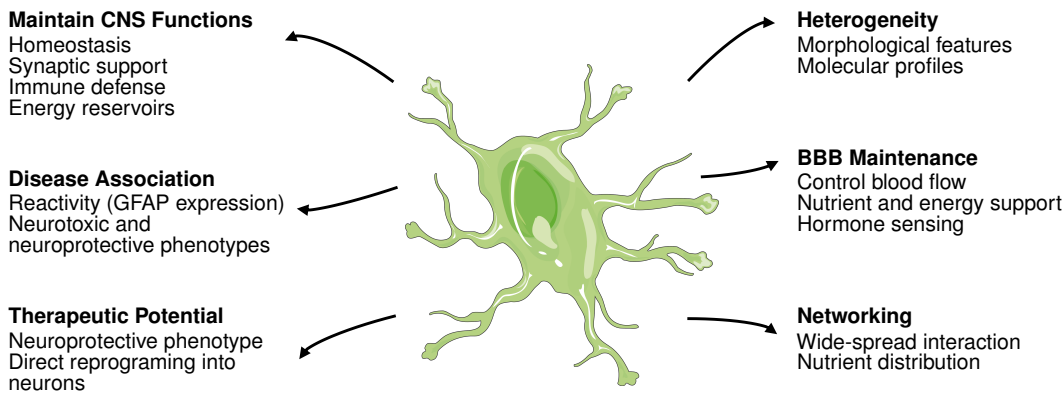


Figure 2.1: Scheme summarizing main astrocytic features and functions. Figure adapted from [43].

whereas fibrous astrocytes, mostly found in the white matter, display a star-like shape [42].

Astrocytes in the GM establish vital connections with blood vessels of the BBB, where they regulate blood flow [44], facilitate hormone sensing [45], and ensure nutrient uptake to sustain CNS cells [36]. Remarkably, mature astrocytes maintain non-overlapping territories, allowing for efficient organization and interaction with virtually every brain cell type. Interconnected through gap junctions, astrocytes form extensive communication networks that support nutrient distribution and homeostasis across the CNS [46]. Additionally, they play a crucial role in meeting the brain's high energy demands by serving as reservoirs of glucose – stored as glycogen –, and fatty acids, ensuring a steady energy supply [47, 48]. Their unique structure and multifaceted functionality underscores their indispensable role in maintaining brain health and vitality [42].

On the other hand, astrocytes also regulate synaptic formation, function, and elimination in both the developing and adult brain [49]. Positioned in direct contact with pre- and post-synaptic neurons, they secrete soluble factors that modulate excitatory and inhibitory synapses. This functional unit – the tripartite synapse – consists of two neurons and a modulating astrocyte. Remarkably, a single astrocyte can regulate up to 2 million synapses in the human brain [50, 51], highlighting their critical role in normal brain function and neuronal activity.

Interestingly, astrocytes are also highly sensitive reporters of neurological diseases and brain injuries. The hypertrophy of astrocytes, marked by an increase in number, thickening and elongation of their main cellular processes, as well as elevated GFAP expression, is widely recognized as an indicator of CNS pathology [52]. This process – known as astrogliosis – involves significant remodeling of astrocytic transcriptional regulation, morphology, metabolism, and physiology, often leading to an enhancement or repression of their normal functions. In these conditions, astrocytes are described as being in a reactive state. Notably, depending on the nature and severity of the injury or disease, reactive astrocytes can adopt diverse phenotypes and molecular profiles, reflecting their inherent heterogeneity.

The role of astrocytes at injury sites remains a topic of active debate within the scientific community.

2. BACKGROUND AND THEORETICAL FOUNDATIONS

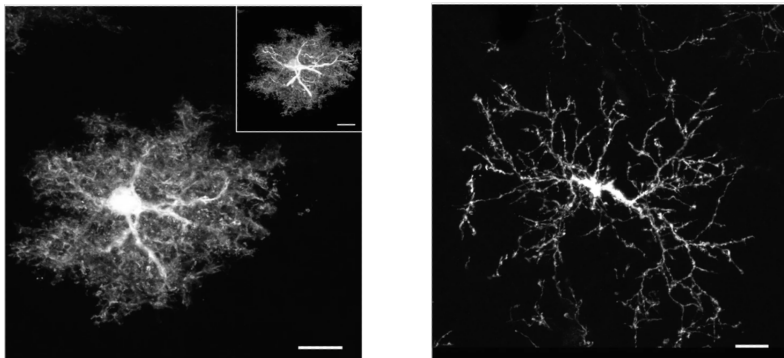


Figure 2.2: Morphological diversity of astrocytes in the CNS. Protoplasmic astrocyte (left) characteristic of the gray matter, and fibrous astrocyte (right) characteristic of the white matter. Scale bars 10 μm . Figure adapted from [42].

Some researchers propose a classification of reactive astrocytes into two contrasting categories: neurotoxic and neuroprotective astrocytes [53]. Neurotoxic astrocytes – A1 reactive astrocytes – are induced by neuroinflammation, with transcriptomic analyses revealing molecular cascades that lead to synaptic destruction and neuronal dysfunction. Contrastingly, neuroprotective astrocytes – or A2 reactive astrocytes – are triggered by ischemia and demonstrate an opposing role, upregulating neurotrophic factors that promote neuronal survival, synaptic repair, and regeneration [52].

However, the dichotomization of astrocytes' response to stress is not universally accepted, as there is considerable variability in astrocytic responses across different diseases and conditions. Furthermore, a lack of robust experimental data and insufficient characterization of marker genes for the A1 and A2 phenotypes have led some researchers to question this categorization of astrocytes [52]. Instead, an alternative model proposes a spectrum of reactive astrocytic profiles that vary based on the type and intensity of stress. This nuanced view suggests that reactive astrocytes may exhibit a continuum of molecular and functional states, which remain poorly understood and warrant further investigation [54].

The molecular heterogeneity of astrocytes poses significant challenges in identifying universal, cell-specific markers exclusive to these cells. Astroglial markers encompass structural proteins, membrane channels and transporters, transcription factors, and energy metabolism proteins. However, not all of these markers are selective for astrocytes or uniformly expressed across all astrocyte subpopulations [55]. Using a combination of markers tailored to experimental objectives often remains the most effective strategy for studying astrocytes under both normal and pathological conditions [55].

GFAP is one of the most widely recognized structural markers of astrocytes, expressed by the majority of CNS astrocytes and neural stem cells. GFAP expression is particularly prominent in fibrous astrocytes compared to protoplasmic astrocytes. Furthermore, GFAP is upregulated in reactive astrocytes under both acute and chronic pathological conditions [12, 13], making it an important indicator of astrocytic reactive activation. This phenomenon has been observed across all mammalian species stud-

ied to date [54]. Other structural markers, such as nestin and vimentin, are predominantly expressed during brain development and are more confined to astrocytic cell bodies in the early stages of CNS formation. Vimentin, although structurally similar to GFAP, is considered a pan-glial marker as it is expressed in multiple CNS glial cell types, including astrocytes, microglia, and oligodendrocytes. Additionally, vimentin is found outside the CNS in fibroblasts, endothelial cells, macrophages, neutrophils, and lymphocytes, limiting its specificity as an astrocyte marker [55]. Complementary, SOX9, a nuclear transcription factor, is a highly specific and almost exclusively astrocyte-associated marker, making it a compelling choice for identifying astrocytes in the CNS [56].

Other commonly used markers include aldehyde dehydrogenase 1 family member L1 (Aldh1L1) and S100 β [55]. Aldh1L1, a cytosolic enzyme involved in astrocytic folate metabolism and the conversion of NADP to NADPH, has shown broader expression in astrocytes than GFAP in certain contexts. Aldh1L1 also reveals finer astrocytic processes than GFAP, making it a valuable marker for detailed morphological studies [57]. Consequently, Aldh1L1 is often used in conjunction with GFAP to achieve more comprehensive astrocytic labeling [55]. S100 β , a calcium-binding cytosolic protein, is particularly effective in labeling the damaged astrocytes and cell bodies of smaller astrocytes with less extensive branching, complementing GFAP staining [55,58,59]. It is preferentially expressed in protoplasmic astrocytes, making it useful for studies focusing on GM astrocytes. However, S100 β is not exclusive to astrocytes, as it is also expressed in subsets of neurons, oligodendrocytes, and neural precursor cells [60].

2.1.2 Astrocytes as Therapeutic Agents

The loss of neurons is at the core of multiple neurodegenerative diseases, such as AD, Huntington's disease, and PD, and upon brain injury. Transplantation of neurons into the affected regions have demonstrated amelioration of the symptoms in patients with PD [61], causing increasing excitement among the scientific community about neuronal replacement therapies aimed for the replacement of neurons in the CNS lost upon injury or neurodegeneration [62,63]. In particular, neuronal replacement may be achieved through three main techniques: endogenous recruitment from neurogenic sources, transplantation of neurons or neurogenic cells, or *in vivo* direct neural reprogramming [63]. Specifically, while direct reprogramming of astrocytes is well-established *in vitro* [64], there is also proof of evidence that proliferating glial cells can also be directly reprogrammed *in vivo* to generate new neurons in response to brain injury [15,65]. Furthermore, these experiments have shown high reprogramming efficiency [66], capacity of further differentiation of newly generated neurons into different neuronal subtypes [17,67,68], and its respective synaptic integration [68].

Astrocyte transplantation is also an attractive therapeutic strategy for a number of diseases. Non disregarding the neurotoxic properties of astrocytes upon injury and disease, astrocytes and astrocyte-lineage cells have been considered as therapeutic agents in cell transplant strategies for amyotrophic

2. BACKGROUND AND THEORETICAL FOUNDATIONS

lateral sclerosis (ALS) [69], PD [70], and spinal cord injury [71].

Despite the great promises of astrocytes as potential agents for brain injury and degeneration therapeutics, there are still some concerns that prevent their application in clinical practice [52, 72]. Namely, the neurotoxic potential of astrocytes, the integration and connectivity of transplanted cells [73], cell conversion efficiency [62] and clinical safety [74] of the proposed techniques demand careful consideration for translating these approaches from preclinical studies into clinical applications.

2.1.3 3D Cell Cultures and Their Advantages

The emergence of 3D cell culture technologies has significantly advanced the study of cellular biology by providing more physiologically relevant models compared to conventional monolayer systems [20]. Unlike monolayer cultures, where cells grow on flat, rigid substrates, 3D cultures allow cells to develop in a scaffold that mimics the complex architecture and microenvironment of living tissues [21]. This more *in vivo*-like setting is essential for studying cellular behavior, disease mechanisms, and therapeutic responses [75–77]. The most promising tools for 3D cell cultures include hydrogel-based systems, alongside spheroids, organoids, and bioprinting techniques [78]. Each of these approaches has specific advantages and applications, particularly in modeling intricate tissues such as the brain [79, 80].

Spheroids and organoids cell clusters are 3D cell culture models that mimic the complex structures and functions of tissues or organs *in vitro* on a self-assembled 3D configuration [81]. In particular brain spheroids and brain organoids can be created from induced pluripotent stem cells (iPSC) [82, 83] or embryonic stem cells [84]. From the structural point of view, while spheroids are simple aggregates of cells focused on cellular interactions within a compact structure, organoids are much more complex, closely resembling the architecture and function of real human organs [85]. Functionally, these structures are capable of performing organ-like functions and can be used as disease modelling and drug testing platforms [86, 87].

Nevertheless, spheroids lack the variety of cell types found in organs and do not recapitulate the full functionality of organ-specific structures [88], whereas organoids lack reproducibility and adult maturation [89]. Furthermore, organoid models also still fail to mimic the ECM of tissues, lack of vasculature and supportive glial cells, often becoming toxic platforms to the cells localized in the core which cannot perform normal physiological metabolism, access nutrients and dispose waste as the cells in the outer layers [90].

On the other hand, hydrogels – crosslinked polymer networks capable of retaining large amounts of water [24] – present an alternative for 3D cell culture. Hydrogels can mimic the ECM by providing structural support and a microenvironment supportive to cell adhesion, proliferation, and differentiation [25]. Furthermore, they can be used to encapsulate spheroids and organoids, or to cast single cells [91, 92]. In particular, single cell strategies are commonly used to deprive cells from cell-to-cell contact allowing

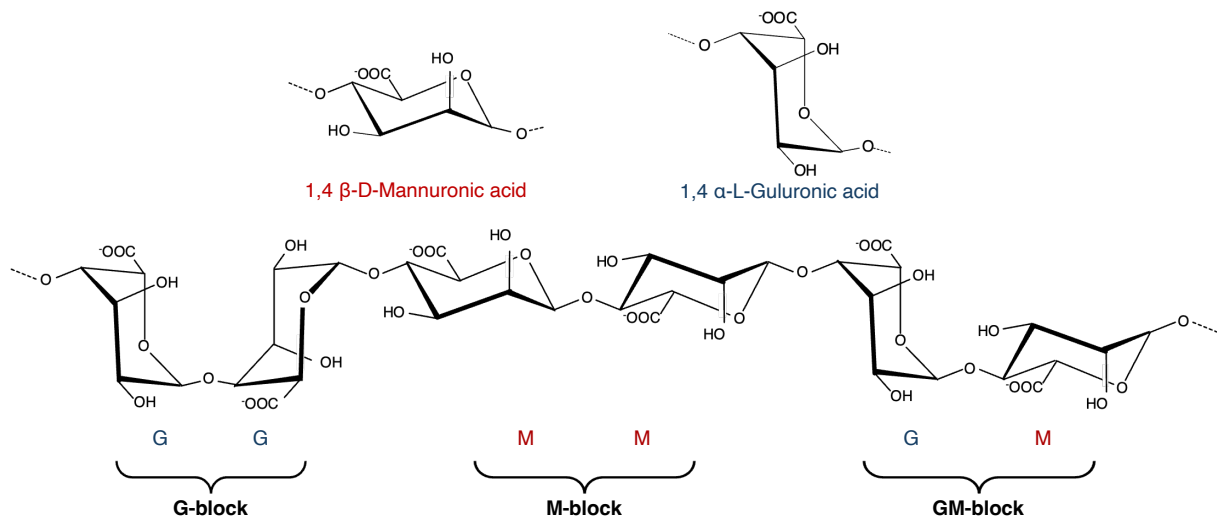


Figure 2.3: Conformation monomers and blocks distribution of alginate polyssacharide. Figure adapted from [95].

for the study of single-cell behaviour or specific cell type sub-populations [92]. Among hydrogel types, alginate, collagen and fibrin-based hydrogels are particularly well-suited for brain tissue modeling due to their tunability and biomimetic properties [93, 94].

Alginate hydrogels are natural polyssacharide-based hydrogels constituted by mannuronic-guluronic acid chains (Figure 2.3). Alginate hydrogels are derived from brown algae (*Phaeophyceae*), and valued for their biocompatibility, low immunogenicity, cell integration and ease of gelation through ionic cross-linking as exemplified in Figure 2.4A [96]. One major advantage of alginate is its tunable stiffness and viscosity, through the combination of high and low molecular weight polymers, which can be adjusted to match the mechanical properties of brain tissue [96, 97]. Additionally, alginate hydrogels provide a stable structure for long-term cultures, since they are not enzymatically degradable by mammals. In turn, the gel degradation is dependent on the degree of oxidation, pH and temperature of the cultures [98]. However, alginate lacks intrinsic cell adhesion motifs, limiting direct cell attachment unless functionalized with bioactive molecules such as arginylglycylaspartic acid (RGD) peptides (Figure 2.4B) [99].

On the other hand, fibrin-based hydrogels (Figure 2.5), formed through the polymerization of fibrinogen in the presence of thrombin, offer a contrasting set of features. As a naturally bioactive material – being the key proteins involved in blood clotting – fibrin contains cell adhesion motifs that promote cell attachment, migration, and differentiation [102]. Fibrin hydrogels are enzymatically degradable – a process called fibrinolysis –, allowing cells to remodel their environment dynamically [103]. Despite, fibrinolysis being essential *in vivo*, to prevent the formation of undesired blod clots, the process is commonly undesired for cell culture applications *in vitro*. To avoid fibrinolysis, aprotinin can be added to the hydrogel solution and delay the hydrogel degradation [104].

Furthermore, collagen, hyaluronic acid (HA), polyacrylamid (PA), and polyethylene glycol (PEG) hy-

2. BACKGROUND AND THEORETICAL FOUNDATIONS

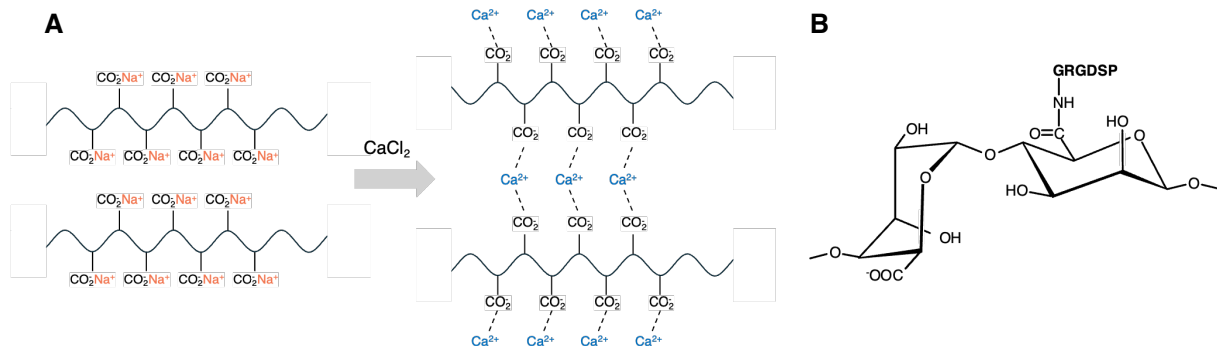


Figure 2.4: Alginate hydrogel properties. **(A)** Alginate gel gelation by crosslinking with Ca^{2+} ions (figure adapted from [100]). **(B)** Chemical structure of RGD-coupled alginate (figure adapted from [101]).

drogels include some other commonly used alternatives. Collagen hydrogels, predominantly composed of type I collagen, closely mimic the native ECM [105], providing a viscoelastic, cytocompatible environment favorable for cell adhesion. However, their low stiffness, limited long-term stability, and batch-to-batch variability are notable limitations [106]. HA hydrogels, derived from a naturally occurring glycosaminoglycan found in various tissues [107], are highly chemically tunable, making them adaptable for applications ranging from development and wound healing to disease modeling [107, 108]. Despite synthetic polymers like PA and PEG not occurring naturally in living tissues, they offer complementary advantages. PA hydrogels are prized for their tunable stiffness and precise protein conjugation, [109], though they are toxic to 3D encapsulated cells. Conversely, PEG hydrogels are biocompatible and chemically inert, allowing user-defined functionalization and 3D encapsulation [110]. Their versatility enables applications in photoencapsulation, drug screening, and tissue engineering [111].

Interestingly, combining various types of hydrogels has shown good outcomes in some applications, overcoming the limitations of each material. For instance, the combination of alginate and fibrin hydrogels allies the mechanical stability of alginate with the bioactivity of fibrin to create a hybrid scaffold

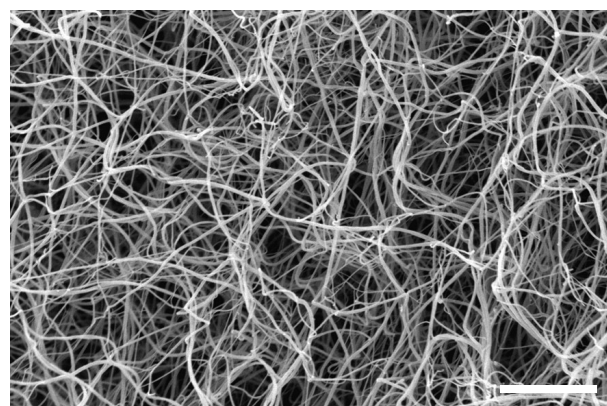


Figure 2.5: Scanning electron micrograph of 1 mg mL^{-1} human fibrinogen polymerized by 1 U mL^{-1} thrombin at pH 7.4 and 150 mM NaCl . Scale bar $10 \mu\text{m}$. Figure adapted from [102].

capable of supporting both structural integrity and cellular functionality [112]. Such combinations are increasingly used in studies creating robust and physiologically relevant models for different applications, such as to study chondrogenesis [113], reconstructing soft tissue [114], and supporting steroidogenesis and in vitro maturation of oocytes [115].

Additionally, bioprinting is a cutting-edge technique that enables the layer-by-layer deposition of bioinks – comprising cells and biomaterials, including hydrogels – to create 3D tissue constructs with precise spatial organization [116]. This approach allows researchers to engineer brain-mimetic models with controlled architecture and the ability to include multiple cell types or gradients, replicating complex tissue behavior [117]. However, bioprinting usage is limited since it is costly and technically demanding. Specifically, bioprinting brain tissue still has several limitations arising from the poor structural fidelity [118], cell damage due to printing pressure and time [119], and the lack of perusable vascular networks [120]. Nevertheless, it holds great promise for creating patient-specific brain models and studying neural tissue regeneration [121].

2.2 Foundations and Theoretical Concepts of Machine Learning

The current artificial intelligence (AI) landscape is vast and complex. In accordance with the conducted research methods, this review focuses on three main areas: machine learning, deep learning, and intelligent computer vision. ML algorithms often depend on manually defined features, where researchers extract characteristics from the monitored systems for the model to analyze, which require considerable domain expertise [122].

While ML can be effective, its performance can be limited by the inherent stochasticity of biological images and the need for extensive annotated data [123]. Deep learning takes a different approach by developing models that learn to identify relevant features directly from raw data and automating the feature extraction process. However, DL still requires even larger annotated datasets and more computational resources than traditional ML approaches, posing challenges in data-scarce or computational power-limited environments [123]. Nevertheless, DL's capacity to recognize complex patterns makes it a powerful tool for analyzing images – in other words, for computer vision. In particular, it is widely applied in the context of diverse and high-dimensional biological images [124], excelling at tasks like image classification, segmentation, and object detection [125]. In Chapter 3, the potential of DL for biomedical image analysis, namely in the context of these tasks, is explored in greater detail.

2.2.1 Core Mathematical Concepts in Machine Learning

Supervised learning is one of the most prominent paradigms within the realm of ML, especially critical for predictive tasks [126, 127]. In supervised learning, the observations, denoted as $x \in \mathcal{X}$, are mapped

2. BACKGROUND AND THEORETICAL FOUNDATIONS

to corresponding outputs or targets, $\mathbf{z} \in \mathcal{Z}$. In this approach, models are trained using labeled datasets, which consist of input-output pairs $\mathcal{D} = (\mathbf{x}_i, \mathbf{z}_i)_{i=1}^N$, where N represents the number of observations in the dataset [122]. In the context of image segmentation and classification, particularly in fields like biomedical imaging, supervised learning requires manual annotation of large datasets, a process that is both time-consuming and labor-intensive [124].

In contrast, unsupervised learning focuses on finding hidden structures or patterns within data without the need for labeled outputs [122]. Unlike supervised learning, which aims to map inputs to known targets, unsupervised methods operate solely on input data $\mathbf{x} \in \mathcal{X}$, without any corresponding labels \mathbf{z} . The goal is to infer the underlying structure of the data, identifying patterns through techniques like clustering or dimensionality reduction. Given a dataset $\mathcal{D} = (\mathbf{x}_i)_{i=1}^N$, unsupervised learning aims to extract meaningful groupings, patterns or representations from the input data alone. Techniques such as k-means clustering, principal component analysis (PCA), and autoencoders are commonly used, each offering distinct ways to explore and represent the latent structures within the data [122].

The nature of observations can vary significantly depending on the problem in hand [128]. In simple multivariate cases, observations are typically represented as an ordered set of features. However, more complex data structures, such as time series, text, and 2D or 3D images, are common in various domains. Output variables may be numerical or categorical, corresponding to regression or classification tasks, respectively. In biological image analysis, regression tasks might involve estimating properties such as cell surface area or volume, while classification tasks could focus on identifying the spatial localization of cells or categorizing them by type. Both tasks typically rely on the supervised learning framework, which requires manual annotation of training data. This process of labeling is labor-intensive and often a bottleneck, especially in fields like microscopy, where vast amounts of data must be annotated to train effective models [125]. Consequently, supervised learning, though powerful, is constrained by the availability and quality of labeled data.

There are several traditional ML approaches to handle predictive problems. In single-output classification problems, the goal is to learn a mapping function, denoted by $f : \mathbb{R}^d \rightarrow \{c_1, \dots, c_K\}$, where $c_k, k = 1, \dots, K$ are the possible classes and K is the cardinality. Binary and multiclass forms of classification are observed when $K = 2$ and $K > 2$, respectively [122]. Probabilistic approaches, such as the Bayesian classification, use the Bayes theorem to predict the class of a given unobserved sample, $\mathbf{x}_{new} \in \mathbb{R}^d$, where d is the dimensionality of the data. This is accomplished by estimating the class that maximizes the posterior probability, $\hat{z} = \arg \max_c \{p(c_k | \mathbf{x}_{new})\}$. Another popular approach, based on information theory, is the decision tree classifier. Decision trees recursively partition the data space into subspaces that contain mainly observations of only one class, with relatively few exceptions. Other alternatives such as random forests and XGBoost provide more robust predictors based on the decision tree classifier. Random forests take advantage of ensembling several independent decision trees clas-

sifiers, whereas XGBoost trains decision trees iteratively optimizing the predictor with gradient descent and regularization parameters. Additionally, support vector machines (SVM) aim to learn the optimal linear hyperplane that maximizes the distance between classes in transformed data spaces, an approach with well-established relevance in diverse domains [128].

Conversely, in a single-output regression problem, the goal is to learn a mapping function $f : \mathbb{R}^d \rightarrow \mathbb{R}$, where the output is real-valued [122]. Linear regression and variations – such as Ridge and Lasso regressions – are some of the most common regression ML approaches. In linear regression, the output is estimated through a linear combination of the input variables with a learned weight vector $\mathbf{w} = [w_0 \ w_1 \ \dots \ w_d]$, where w_0 is the estimated bias and w_j the weight associated to each observation's feature, x_j , $j = 1, \dots, d$. Thus, given a dataset X containing $\{\mathbf{x}_i\}_{i \in \{1, \dots, N\}}$ observations whose design matrix is $\tilde{X} = [\mathbf{1} \ \mathbf{x}_1 \ \dots \ \mathbf{x}_N]^T$, the estimation output is $\hat{z}_i = \mathbf{w}^T \mathbf{x}_i$. In a regression problem, the objective is to minimize a loss function that quantifies the difference between the predicted and the real values. In linear regression, the method of the least squares, which aims to minimize the sum of squared residual errors (SSE),

$$E_{SSE}(\mathbf{w}) = \sum_{i=1}^n (z_i - \hat{z}_i)^2, \quad (2.1)$$

is commonly considered. The weight vector that minimizes the loss function can be derived from setting the gradient of the SSE to zero, yielding $\mathbf{w} = (\tilde{X}^T \tilde{X})^{-1} \tilde{X}^T \mathbf{z}$ (for detailed derivation see 128). Another alternative is to use the stochastic gradient descent (SGD) update rule. With SGD, the weight vector is randomly initialized and updated recursively with one random observation each time at a predefined learning rate, η ,

$$\begin{aligned} \mathbf{w}^{t+1} &= \mathbf{w}^t - \eta \cdot \nabla_{\mathbf{w}}(\tilde{\mathbf{x}}_k) \\ &= \mathbf{w}^t + \eta \cdot (z_k - \tilde{\mathbf{x}}_k^T \mathbf{w}^t) \cdot \tilde{\mathbf{x}}_k, \end{aligned} \quad (2.2)$$

where $\tilde{\mathbf{x}}_k = [1 \ x_1 \ \dots \ x_k]$.

Nevertheless, linear regression estimators are often prone to overfitting the training observations, particularly when considering data representations in high-dimensional spaces. To overcome this problem, regularization parameters can be added to the SSE, such as in the Ridge and Lasso regressions:

$$E_{Ridge}(\mathbf{w}) = \sum_{i=1}^n (z_i - \hat{z}_i)^2 + \lambda \|\mathbf{w}\|_2^2, \quad (2.3)$$

$$E_{Lasso}(\mathbf{w}) = \sum_{i=1}^n (z_i - \hat{z}_i)^2 + \lambda \|\mathbf{w}\|_1. \quad (2.4)$$

In Ridge regression, the penalty term shrinks the weight coefficients towards zero, improving their stability [129]. Contrastingly, the Lasso regression typically produces more sparse solutions since the

2. BACKGROUND AND THEORETICAL FOUNDATIONS

minimal achievable loss often occurs on an axis, which sets the variable's weight to zero [130]. Furthermore, the strength of the regularization term is adjusted by λ hyperparameter, which needs to be optimized by cross-validation [131].

Perceptrons, on the other hand, are computational units that aim to mimic the human neuron and can solve simple regression and classification problems [128, 129]. These units effect a weighted summation of their inputs, resulting in a *net* value, and subsequently apply a nonlinear activation function, ϕ , to produce the output,

$$\hat{z} = \phi\left(\sum_{j=1}^d (w_j x_j) + b\right) = \phi(\mathbf{w}^T \mathbf{x} + b) = \phi(\text{net}). \quad (2.5)$$

Activation functions are crucial as they allow the capture of nonlinear features without requiring the input transformations, setting perceptrons apart from conventional linear regressors, and are chosen according to the problem. The most simple among these is the identity function, commonly used in regression problems and returns its argument. For binary classification problems, the step function,

$$\text{step}(\text{net}) = \begin{cases} 0, & \text{net} \leq 0 \\ 1, & \text{net} > 0 \end{cases}, \quad (2.6)$$

was the originally proposed activation function. Nevertheless, its discrete mapping outputs do not allow to discern the observations' distance to the modeled hyperplane, potentially hampering the learning process. Consequently, the step function has largely been deprecated in most applications and replaced by alternative methods. With the sigmoid function,

$$\sigma(\text{net}) = \frac{1}{1 + e^{-\text{net}}}, \quad (2.7)$$

the output of the perceptron can be thought of as a probability between 0 and 1, which enables the conceptualization of the accuracy of the classification. On the other hand, the hyperbolic tangent,

$$\tanh(\text{net}) = \frac{e^{\text{net}} - e^{-\text{net}}}{e^{\text{net}} + e^{-\text{net}}}, \quad (2.8)$$

has a shape similar to the sigmoid, but the output ranges between -1 and +1. Finally, the rectifier linear unit (ReLU) function,

$$\text{ReLU}(\text{net}) = \begin{cases} 0, & \text{net} \leq 0 \\ \text{net}, & \text{net} > 0 \end{cases}, \quad (2.9)$$

is a popular choice when learning neural networks described by multi-layer compositions of perceptrons.

Machine learning tasks often involve predicting multiple unrelated target variables simultaneously, leading to what is known as a multi-output problem. These target variables can span both categorical and numerical domains, resulting in a multi-label classification or a multi-output regression problem, respectively. Moreover, these different types of targets can coexist within the same multi-output context. While traditional ML algorithms can effectively address certain multi-output problems, more complex

supervised learning tasks, such as 3D image prediction problems, often make use of deep learning techniques to capture intricate patterns and dependencies across multiple outputs [132]. At the core of DL models are artificial neural networks (ANN), which are computational models inspired by the structure and functioning of the human brain and use perceptrons as their basic units [128].

An ANN emerges from the interconnection of multiple perceptrons, featuring an input layer responsible for aggregating the input data \mathbf{x} , hidden layers that perform intermediate computations, and an output layer where the final prediction $\hat{\mathbf{z}}$ is generated [128]. In more intricate problem domains, the network's complexity must be enhanced, often necessitating the inclusion of a greater number of hidden layers. Such networks are commonly referred to as deep neural networks. These networks possess the ability to effectively model both regression and classification problems by learning network weights that minimize a loss, $\mathcal{L}(\mathbf{w})$, associated with the error between the estimation and the targets. Generally, the weights update is performed iteratively via gradient descent rules [128].

In regression tasks, a common loss function is the squared error loss function,

$$\mathcal{L}_{SSE}(\mathbf{w}) = \frac{1}{2} \|\mathbf{z} - \hat{\mathbf{z}}\|^2 = \frac{1}{2} \sum_{j=1}^L (z_j - \hat{z}_j)^2, \quad (2.10)$$

where L is the dimensionality of the response vector, which employs the principle adjacent to the classical regression learning problems debated above (equation 2.1).

In classification tasks, the output layer generally has as many neurons as the number of classes in the problem, and the target response is commonly encoded as a one-hot vector. Thus, in a multi-class classification problem, the softmax function,

$$\text{softmax}(\text{net}_i) = \frac{e^{\text{net}_i}}{\sum_{j=1}^L e^{\text{net}_j}}, \quad (2.11)$$

is applied on the output layer to associate each output neuron to a rough probability estimate. In contrast with regression, the loss function for multi-class classification tasks is often modeled by the cross-entropy loss function,

$$\mathcal{L}_{CE}(\mathbf{w}) = - \sum_{j=1}^L z_j \cdot \ln(\hat{z}_j). \quad (2.12)$$

The gradient descent method can minimize the loss function when the non-linear activation functions in the network are differentiable. The gradient descent updates the model weights in the opposite direction of the gradient of the loss function, $\nabla \mathcal{L}(\mathbf{w}^t) = \frac{\partial \mathcal{L}(\mathbf{w}^t)}{\partial \mathbf{w}^t}$, at a predefined learning rate, $\eta > 0$,

$$\mathbf{w}^{t+1} = \mathbf{w}^t - \eta \nabla \mathcal{L}(\mathbf{w}^t), \quad (2.13)$$

where t is the iteration index. The learning rate plays an essential role in the learning convergence of

the model, thus it should be properly tuned [131].

Additionally, the weights can be updated considering all observations by summing the gradients produced by each sample individually, with a batch gradient descent approach, or consecutively with one observation at a time, with SGD. While the batch gradient descent is more stable, it is slower and easily tied in local minima. Therefore, if the dataset is too large, adopting SGD or establishing a trade-off between the two poles might be preferable via mini-batch gradient descent [129].

To avoid overfitting the training dataset, dropout is a common strategy to decrease the test dataset error [129]. Dropout is a stochastic regularization method in which a subset of hidden units is chosen and deactivated at each training step. This way, the deactivated units are not allowed to learn, and the model is less likely to overfit. Additionally, the training is faster since the network has fewer parameters at each training step. The dropout ratio hyperparameter is manually defined and sets the percentage of hidden units deactivated at each step.

2.2.2 Convolutional Neural Networks

Tailoring the choice of the artificial neural network to the intricacies of a given problem is of pivotal importance to obtain optimal results. In the contemporary landscape of neural networks, diverse architectures are designed to respond to specific problem domains. In particular, the application of convolutional neural networks (CNN) is notable in the computer vision domain.

Due to the intrinsic properties of an image, its meaning is generally not driven by individual input pixel values but by their adjacency patterning. Due to this property, if we were to construct a fully connected networks (FCN) with an image as input, the network would yield comparable results regardless of the spatial organization of the input pixels during the training process. Additionally, it would be intractable to compute the weights of a FCN for large images [130].

Convolutional neural networks can be thought of as a specialized type of multilayer perceptron that operates in a localized and sparse manner and is designed to exploit the spatial structure of the input data [130]. The definition of a CNN is any neural network that contains a convolutional layer. Accordingly, the traditional CNN architecture comprises an input layer, followed by several convolutional-pooling layers, one or multiple fully connected layers, and an output layer. Note that fully connected layers are essential to map the output to the target vector.

The design of a CNN respects three fundamental principles: sparse interactions, parameter sharing, and equivariance to translation. Firstly, CNNs establish sparse interactions between its neurons by employing a filter, also referred to as *kernel*. This strategic application to multiple image regions facilitates the detection of meaningful features at lower levels, such as edges. Secondly, the parameter-sharing feature distinguishes CNNs by applying the same kernel across multiple image regions. In contrast to FCNs, which compute distinct weights for every non-linear relation between input and output, CNNs

preserve the weight values in each convolutional layer. Finally, the equivariance to translation property ensures that the output adapts correspondingly to changes in the input, meaning that if an object undergoes translation in the input, its representation will undergo a parallel translation in the output of a convolutional layer. These features refine the network's ability to discern intricate details by connecting a subset of neurons in layer p to a single neuron in layer $p + 1$ and substantially reduce the number of parameters stored, also contributing to a more generalized model [129].

The standard CNN layer unfolds into three distinct stages. In the initial convolution stage, multiple convolutions are executed concurrently, generating an array of linear activations. Following this, the activation stage introduces a crucial non-linear element by applying an activation function to the net values. The ReLU activation function stands out as a prevailing choice. Finally, a pooling function is applied further modifying the output for subsequent layers. In certain instances, pooling is essential to handle the classification of inputs of varying sizes by extracting the same number of summary features from the convolutional layer, regardless of the input size.

The convolution can be thought of as the integration (or summation in the discrete scenario) of the product obtained by sliding one function, $w(t)$, over the other, $x(t)$,

$$s(t) = (x * w)(t) = \int x(\tau) \cdot w(t - \tau) d\tau. \quad (2.14)$$

Translating to the convolutional network terminology, now $x(t)$ is the input of the network, and $w(t)$ as the kernel. Under this light, the output of the convolution operation, $s(t)$, denotes the feature map [128].

Considering a 2D input, let $\mathbf{X} \in \mathbb{R}^{n \times n}$ be the input matrix, and let $\mathbf{W} \in \mathbb{R}^{k \times k}$ be the matrix of weights, with $k \leq n$. Let also $\mathbf{X}_k(i, j) \in \mathbb{R}^{k \times k}$,

$$\mathbf{X}_k(i, j) = \begin{pmatrix} x_{i,j} & x_{i,j+1} & \cdots & x_{i,j+k-1} \\ x_{i+1,j} & x_{i+1,j+1} & \cdots & x_{i+1,j+k-1} \\ \vdots & \vdots & \ddots & \vdots \\ x_{i+k-1,j} & x_{i+k-1,j+1} & \cdots & x_{i+k-1,j+k-1} \end{pmatrix}, \quad (2.15)$$

denote the submatrix of \mathbf{X} that starts at row i and column j .

The feature map obtained through the convolution of \mathbf{X} and \mathbf{W} ,

$$\mathbf{X} * \mathbf{W} = \begin{pmatrix} \text{sum}(\mathbf{X}_k(1, 1) \odot \mathbf{W}) & \cdots & \text{sum}(\mathbf{X}_k(1, n - k + 1) \odot \mathbf{W}) \\ \text{sum}(\mathbf{X}_k(2, 1) \odot \mathbf{W}) & \cdots & \text{sum}(\mathbf{X}_k(2, n - k + 1) \odot \mathbf{W}) \\ \vdots & \ddots & \vdots \\ \text{sum}(\mathbf{X}_k(n - k + 1, 1) \odot \mathbf{W}) & \cdots & \text{sum}(\mathbf{X}_k(n - k + 1, n - k + 1) \odot \mathbf{W}) \end{pmatrix}, \quad (2.16)$$

corresponds to the $(n - k + 1) \times (n - k + 1)$ matrix that is obtained by summing entries of the matrix resulting from the Hadamard product of the kernel, \mathbf{W} , with each submatrix of \mathbf{X} in the sliding window. The summation function, $\text{sum}(\mathbf{A})$, simply sums every entry of the matrix \mathbf{A} .

2. BACKGROUND AND THEORETICAL FOUNDATIONS

The employment of the convolution function leads to the successive decrease of the data size. The progressive shrinkage of the matrices, leads to the loss of valuable information, especially at the borders, and limits the number of convolutional layers.

To prevent these issues, padding is commonly applied in CNNs. It consists of adding a default number of zeros in each dimension of the input at both sides, before performing the convolution. This way, the output dimensions can be adjusted while the impact of the convolutional operation on the edge pixels is also reduced. Padding enables the preservation of the input size, hence it allows to have arbitrarily deep convolutional layers in a CNN [128].

On the other hand, striding is often used to reduce the spatial dimension of the output feature maps, while capturing more high-level features of the input and discarding more localized features. The stride, $s \geq 1$, defines the jumps of the sliding window during convolution [128].

The pooling function aims to replace the output of the net at a certain location by the most meaningful summary statistic of its neighbouring outputs. By doing this, the pooling helps to turn the representation invariant to small translations of the input, thus acquiring a wider feature context. There are a number of statistics that can be employed, among which the average, the L_2 norm, the weighted-average, or the maximum value are typical options. The latter approach is the most commonly employed and is referred to as *max pooling* [129].

The pooling function uses a fixed zero bias, and kernel weights fixed to 1. Neither of these are ever updated in backpropagation, thus the pooling function is maintained throughout the training. Generally, in polling the stride equal to the kernel size. This way, the pooling function is always applied over disjoint $k \times k$ windows and each convolution output value is only used once by the summary statistics.

In some architectures, there is also useful to upsample the feature map in opposition to the downampling produced by the pooling layers. These layers are referred to as upsampling layers, or deconvolution layers, and their purpose is to increase the dimensionality of the feature map. The mechanism underlying the upsampling is essentially a convolution with a fractional input stride $1/f$, in which factor f is an integer value. The resulting feature map is calculated by applying a deconvolutional filter to the input. This filter can be either fixed, using a bilinear interpolation, for example, or learned by backpropagation like the kernel in convolution layers [133].

Three-dimensional CNNs are an extension of the traditional CNNs. They are designed to operate with volumetric data such as 3D medical images, video sequences, and spatio-temporal data. Since in 3D convolutions the input is a three-dimensional tensor, defined as $\mathbf{X} \in \mathbb{R}^{n_1 \times n_2 \times n_3}$, the kernel must also be a three-dimensional tensor, $\mathbf{W} \in \mathbb{R}^{k_1 \times k_2 \times k_3}$, that slides in the three dimensions of the input [128].

In CNNs where the input is a 2D coloured image, the channels correspond to the red-green-blue filters. In this particular case, the kernel typically has the same depth as the number of channels: $k_3 = n_3$. Hence, $\mathbf{W} \in \mathbb{R}^{k_1 \times k_2 \times n_3}$, and the feature map obtained is a $(n_1 - k_1 + 1) \times (n_2 - k_2 + 1)$ matrix,

similar to equation 2.16.

Most commonly, the third dimension of the input tensor also contains valuable spatial information, such as in 3D images. In these instances, it is essential to use a kernel smaller than the input data in the third dimension. Therefore, if $k_3 \neq n_3$, then the convolution of \mathbf{X} with \mathbf{W} results in a $(n_1 - k_1 + 1) \times (n_2 - k_2 + 1) \times (n_3 - k_3 + 1)$ tensor, whose third dimension simply results from the expansion of the convolution in depth.

2.2.3 Evaluation Metrics in Supervised Learning Settings

In supervised learning problems, the primary objective is to learn the optimal model that estimates an output \hat{z} , as accurately as possible. To assess the performance of a given predictor without incurring biases, a common strategy is to split the dataset into a training and a testing set with the hold-out method. This method allows to train and test the model with independent sets of observations, generally with a 70-30% or 80-20% ratio. Moreover, it is important to bear in mind that a substantial amount of training data is necessary to produce an accurate model. Hence, in scenarios where the data is limited, the k -fold cross-validation method can be more appropriate. This method divides the original dataset X into k mutually exclusive subsets: $X = \{X_1, \dots, X_k\}$. Afterwards, it trains and validates the architecture k times, using $X \setminus X_k$ as the training set and X_k as the testing set. Furthermore, in stratified k -fold cross-validation, the data is split so the targets are identically distributed in every partition.

In regression problems, SSE has been previously discussed as a crucial metric for training a regression model. However, its utility extends beyond training; it can also serve as a valuable tool for assessing the quality of the resulting regressor. Additionally, the residuals, which are the absolute differences between the actual and the predicted values, are highly informative in evaluating a regressor. With these residuals, we can compute various performance metrics, including the mean absolute error (MAE), mean squared error (MSE), and root mean squared error (RMSE),

$$MAE = \frac{1}{n} \sum_{i=1}^n |z_i - \hat{z}_i|, \quad MSE = \frac{1}{n} \sum_{i=1}^n (z_i - \hat{z}_i)^2, \quad RMSE = \sqrt{MSE}. \quad (2.17)$$

Whereas in classification settings, the most general performance metrics are the error rate and accuracy. The error rate,

$$\text{error rate} = \frac{1}{n} \sum_{i=1}^n I(z_i \neq \hat{z}_i), \quad (2.18)$$

measures the percentage of the model's incorrect predictions over the training set, where I is an indicator function that assumes the value 1 when the argument is true and 0 otherwise. Whereas the accuracy,

$$\text{accuracy} = \frac{1}{n} \sum_{i=1}^n I(z_i = \hat{z}_i) = 1 - \text{error rate}, \quad (2.19)$$

2. BACKGROUND AND THEORETICAL FOUNDATIONS

is the percentage of the model's correct predictions, thus the complement of the error rate.

On the other hand, the model's performance can be assessed by evaluating class-conditional metrics. These metrics include the precision, recall, and Dice coefficient (DC). The precision of class k ,

$$\text{precision}_k = \frac{TP}{TP + FP}, \quad (2.20)$$

is equivalent to the class-conditional accuracy, measuring the percentage of true positive (TP) predictions of class c_k over all observations predicted to be in that class, including the TP and false positive (FP). Conversely, the recall of the class c_k ,

$$\text{recall}_k = \frac{TP}{TP + FN}, \quad (2.21)$$

corresponds to the fraction of correct predictions of that class over all observations from the same class, including the TP and false negative (FN) observations. However, there is often a tradeoff between the precision and recall that does not allow a complete overview of the model's performance. Thus, the class-conditional F1-score, also regarded as DC,

$$F1\text{-score}_k = DC_k = 2 \cdot \frac{\text{precision}_k \cdot \text{recall}_k}{\text{precision}_k + \text{recall}_k} = \frac{2 \cdot TP}{2 \cdot TP + FP + FN}, \quad (2.22)$$

computes their harmonic mean. Additionally, the overall F1-score of the classifier,

$$F1\text{-score} = DC = \frac{1}{K} \sum_{k=1}^K F1\text{-score}_k, \quad (2.23)$$

can be obtained by averaging the class-conditional F1-scores.

In computer vision tasks, such as image segmentation and object detection, the most common performance metrics are the Jaccard index, also known as the intersection over union (IoU) coefficient, and the mean average precision (mAP). Considering a multi-label problem with cardinality L , in which the objective is to estimate L categorical targets, $\hat{z}_i^{(j)}$, for each observation x_i , the IoU,

$$\text{IoU}_i = \frac{1}{L} \cdot \sum_{j=1}^L I(z_i^{(j)} = \hat{z}_i^{(j)}), \quad (2.24)$$

with $i = 1, \dots, N$ and $j = 1, \dots, L$, is the fraction of accurate target-variable classifications over the total number of target-variables. Furthermore, the mean IoU provides a global metric for the model's performance. The mAP is calculated for each class c_k with reference to specific IoU threshold values, τ ,

$$mAP_\tau^k = \frac{TP}{TP + FP + FN}, \quad (2.25)$$

thus its value is highly dependent on the threshold defined. Lower threshold values, usually $\tau < 0.5$, are used for the purpose of counting identified objects, whereas the measurement of specific features related to the objects identified, such as intensity measurements, require more accurate shapes and thus require higher value of τ [134]. Furthermore, to acquire a better overview of the models' performance and compare the performance of different models, it is usual to compute the mean of the mAP over different threshold values $T = \tau_1, \dots, \tau_T$,

$$mAP_T = \frac{1}{T} \cdot \sum_{\tau=\tau_1}^{\tau_T} mAP_\tau. \quad (2.26)$$

2.2.4 Data Augmentation, Transfer Learning and Fine-Tuning

Developing a robust deep learning model requires a substantial amount of annotated training data. This is often challenging, particularly in the field of biology, where data collection is typically labor-intensive and costly [124]. To overcome this hurdle, data augmentation techniques can be a valuable resource [129]. Data augmentation involves creating synthetic data and incorporating it into the dataset. This approach has proven particularly effective in addressing image classification problems, such as object recognition and classification.

Common image augmentation operations include translation, rotation, scaling, cropping, and noise injection [129]. These operations are relatively straightforward to implement and have been shown to significantly enhance the model's performance. Furthermore, some researchers have delved into introducing noise to the hidden units of ANNs, extending data augmentation to multiple levels of abstraction. Their findings demonstrate high efficacy in this approach [135].

Transfer learning is an additional strategy for managing the scarcity of observations in a dataset. It allows using a partially learned neural network in an arbitrary learning task and extrapolating it to another learning task. Importantly, many of the factors that explain variations in the dataset of the original task are also relevant to the variations that need to be captured in the dataset of the target task, under the assumption that they are similar to some extent [129].

In the computer vision domain, many datasets can share low-level notions of edges and visual shapes. The effects of shared geometric transformations can aid the learning process of a new task while accelerating training. These features are preserved in the first layers of the pretrained model, while the problem-specific features can be learned by the model's deeper layers – predictor layers. Additionally, fine-tuning is a valuable approach within the realm of transfer learning. While the simplest forms of transfer learning maintain the pretrained model's initial parameters, fine-tuning takes it a step further by allowing adjustments to better align with the characteristics of a new dataset.

Fine-tuning typically unfolds in two distinct phases. In the feature extraction phase, the parameters of the top layers are kept constant from the pretrained model, while the parameters of the predictor layers

2. BACKGROUND AND THEORETICAL FOUNDATIONS

are learned using the new dataset as input. This allows the model to capture domain-specific features from the new data and learn the predictive task. In the fine-tuning phase, some of the pretrained model layers are unfrozen, making them adaptable to the new dataset during the subsequent training. This two-step process enables the model to leverage the knowledge gained from its initial pretraining while tailoring its parameters to the specific requirements of the new task or dataset [129].

3

State-of-the-Art Deep Learning Approaches in Biomedical Image Analysis

Contents

3.1 Deep Learning for Biomedical Imaging	26
3.2 Foundations of Computer Vision Tasks	27

This chapter is focused on exploration of state-of-the-art deep learning technologies for biomedical image analysis. In particular, it focuses on the exploration of available technologies for biological image analysis resorting to image classification, object detection and image segmentation. At the end of this chapter, Table 3.1 provides a summary of the key networks discussed below.

3.1 Deep Learning for Biomedical Imaging

Computer vision, a prominent field within DL, is rapidly emerging as a transformative technology with the potential to revolutionize the analysis of complex biomedical imaging data [125]. Its capability to extract intricate features from raw data is driving advancements in various fields, including medical imaging, such as X-ray computed tomography (CT), magnetic resonance imaging (MRI), and positron emission tomography (PET) imaging [136]; pathological imaging, particularly in oncological pathology [137]; animal preclinical imaging, such as images from micro versions of CT, MRI, and PET scanners used in animal models; and biological imaging. This progress has the potential to transform only the acquisition, processing, and analysis of medical images, greatly impacting healthcare outcomes.

Biological imaging, in particular biological microscopy, refers to techniques employed to observe biological processes at the cellular and molecular levels. These include light microscopy (LM), fluorescence microscopy (FM), particularly confocal microscopy, electron microscopy (EM), and scanning probe microscopy (SPM). Among all biomedical imaging techniques, microscopy is often regarded the most challenging for image analysis automation due to the absence of standardized imaging protocols and the high variability in experimental conditions. As a result, microscopy images exhibit significant diversity both within and across experiments [125].

Moreover, modern automated microscopes can generate terabytes of image data per experiment, a volume that remains largely untapped without leveraging the computational power and capabilities of deep learning for analysis [125]. The analysis of biological images is a challenging task for researchers, being time-consuming and subjective, albeit crucial for accurate research outcomes [138]. However, manually analyzing large datasets is still a significant hurdle. Automation through intelligent algorithms is not just a convenience but a necessity for reducing manual effort and increasing accuracy and reproducibility of the analysis [29].

Key applications in biomedical image analysis include image enhancement, object detection, image segmentation, object tracking, and classification. Image enhancement improves image quality by reducing noise and adjusting contrast, aiding clearer interpretation. Object detection identifies and locates specific structures, such as tumors or cells, for accurate diagnostics. Image segmentation divides images into distinct regions, allowing detailed analysis of tissues or organs. Object tracking monitors dynamic processes, like cell movement or disease progression, over time. Classification categorizes

images or regions, such as identifying diseases or cell types.

Various softwares, including Imaris [139], CellProfiler [138], Ilastik [140], MorphoGraphX [141], and numerous Fiji [31] plugins, have been developed to assist with image processing and analysis. While these tools have made strides, they often struggle with the vast diversity of microscopy datasets – different imaging techniques and complex image and dataset structures pose significant challenges [142]. Specifically, automating the analysis of astrocyte cultures, known for their heterogeneity and morphological complexity [29, 143], is especially difficult due to the high data variability. In the upcoming section, there will be explored in deeper detail how DL, and in particular CNNs can be leveraged to perform classification, object detection and image segmentation tasks.

Despite its transformative potential, challenges persist. Developing robust models that generalize across diverse populations and imaging devices requires addressing data heterogeneity and biases. The reliance on large, annotated datasets is another significant barrier, prompting interest in semi-supervised, unsupervised, and federated learning techniques. Moreover, ensuring model interpretability and gaining regulatory approval are critical for translating these innovations into clinical practice [125].

3.2 Foundations of Computer Vision Tasks

In the following sections, we will explore some of the most commonly used computer vision tools in biomedical research, specifically focusing on image classification, object detection, and image segmentation. Figure 3.1 provides an outlook into each of these tasks, and expected output in the context of astrocyte culture characterization.

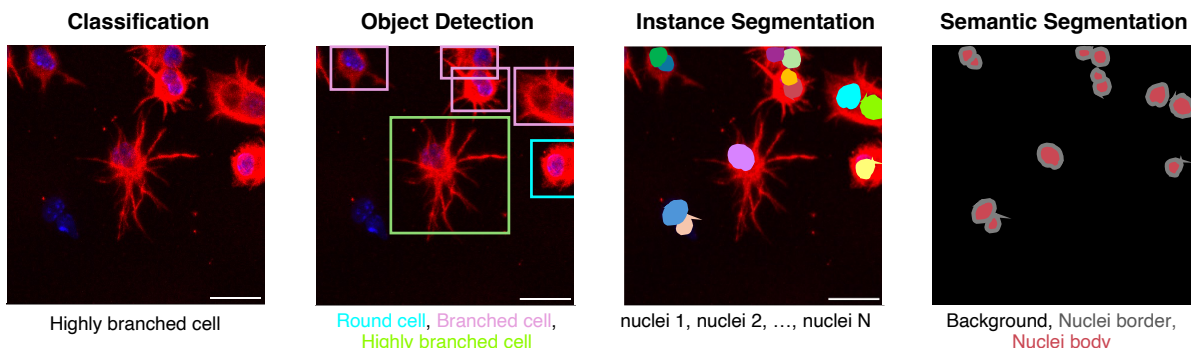


Figure 3.1: A look into computer vision tasks of classification, object detection and image segmentation in the context of astrocyte culture characterization. Maximum intensity projection of 100 μm z-stack image of a 7 DIV culture of p5-7 murine cortical gray matter astrocytes in alginate-based hydrogel. Scale 20 μm .

3.2.1 Image Classification

Image classification stands as a crucial computer vision task where a model undergoes training to categorize images into predefined classes. Recent advancements in this field focus predominantly on enhancing the classifier's performance using standardized databases. These databases not only facilitate direct model performance comparison but also offer a diverse array of images crucial for ensuring model generalization and preventing overfitting. Furthermore, once a network is trained on one of these datasets, the model's adaptability shines as it can be fine-tuned to suit specific applications using smaller annotated datasets, which is particularly invaluable in the biological domain, where the scarcity of annotated data frequently presents a challenge [124]. Notably, the ImageNet dataset [144], also known as the ILSVRC dataset, stands as one of the most renowned collections, comprising over 1.28 million images for training, 50k for validation, and 100k for testing, spanning across a thousand object classes.

The most commonly used architectures for classification tasks are based on very deep convolutional networks (VGG) and residual networks (ResNet) [145]. VGG networks trained in the ImageNet dataset were introduced in [146]. VGG networks are characterized by their increased depth compared to previous generalization models, reaching up to 19 layers (VGG16 and VGG19 are extensively documented in the literature), showing remarkable classification accuracies and broad generalization attributable to the increased representation depth. Their architecture embodies five variable-sized stacks of 3×3 padded convolutional layers followed by a 2×2 max-pooling layer. The CNN is followed by three fully connected layers: the first two have 4096 channels each and 0.5 dropout rate, while the ultimate layer serves as the classification layer, with 1000 output channels.

Meanwhile, the ResNet [147] maintained a complexity inferior to the VGG networks while performing in a much larger depth – reaching up to 152 layers. These networks tackled common problems of deep networks, such as the vanishing/exploding gradient problem, in which the weight updates are either too small or too unstable, and the degradation problem, in which the model accuracy saturates and then starts to degrade rapidly. ResNet' underlying principle is using residual blocks with shortcut connections between them. This way, the learning of residual maps is significantly easier to optimize and have greater performance. The general architecture of a ResNet consists of several padded convolutional layers organized into blocks. Between each block, the skip connection allows the input of that block to be added element-wise to its output, creating a shortcut for the gradient to flow during training. Following the sequence of the residual blocks, a fully connected layer maps the result to 1000 output channels corresponding to the classes of the ImageNet dataset.

A concrete application of classification to biological data analysis is cell phenotyping. A network designed for cell phenotyping can be trained to either directly predict the phenotype, in which the network's last layer corresponds to a classification layer, or extract a feature vector, in which the autoencoder can extract the most meaningful features from the input images. These features can then be used to either

supervisedly assign a phenotype from a set of classes known *a priori* or unsurervisedly cluster the observations. The description of phenotypes with unsupervised clustering allows the discovery of novel classes and surpasses the need for manually annotated datasets [148].

Many authors have attempted to develop DL tools for this classification problem using different approaches, such as by developing a multi-scale CNN that considers the input image at different spatial scales in parallel and assigns a probability to each possible phenotype class [149]. However, a model like this is limited to the classes defined *a priori* and cannot detect novel phenotypes. To address this limitation, *CellCognition Explorer* tool emerged to extract feature vectors with an autoencoder and infer the detection of novel phenotypes from nuclear morphology screening data with unsupervised clustering [150].

Alternatively, state-of-the-art algorithms, such as Inception-v3, VGG16 ResNet-152, and ResNet-101, pretrained on the ImageNet dataset were also used extract features and perform morphological profiling of fluorescence microscopy images of cultures human cells without additional fine-tuning [151]. Instead of using unsupervised learning, the target mechanisms of action were benchmarked by averaging the features of each class, and the observations were then classified using the 1-nearest neighbour classifier.

Despite VGG and ResNet networks being specifically designed for image classification, adaptations of these networks are also being used for other applications. Namely, autoencoder features of their CNN layers are notably beneficial to perform object detection and segmentation tasks through the extraction of features, as we will explore deeper in further Subsubsections 3.2.2 and 3.2.3.

3.2.2 Object Detection

The task of object detection involves pinpointing objects within an image using bounding boxes and assigning corresponding labels. In images with multiple objects, detection is a crucial step preceding classification. As each instance can only be associated with one label, separate classification of the multiple objects within the image is necessary for accurate analysis [152].

The concept of combining a region proposal algorithm with CNNs to devise a recursive convolutional neural network (R-CNN) for object detection was introduced in [153]. This approach involves three distinct modules: the initial module generates region proposals utilizing a selective search algorithm, followed by a large CNN to extract feature vectors, and finally, a module for object classification using class-specific linear SVMs. A notable limitation of this network is its relatively slow process, requiring the generation of approximately 2.000 category-independent region proposals for each input image. Additionally, due to its multi-staged nature, it cannot be optimized end-to-end. Building upon R-CNNs, a more efficient variant known as Faster R-CNN, consisting of only two networks was later proposed [154]. The first network, a fully convolutional region proposal network (RPN), produces object proposals with cor-

responding objectness scores, measuring the likelihood of a region belonging to specific object classes rather than the background. This RPN utilizes a VGG16 as a feature extractor alongside two sibling fully connected layers for generating objectness scores and bounding boxes, respectively. The second network, a Fast R-CNN [155], utilizes a fixed-length feature vector obtained through a region of interest pooling layer for object detection within the proposed regions. Faster R-CNN significantly improves efficiency compared to the traditional R-CNN and allows for end-to-end training.

A different approach to this task is to frame object detection as a regression problem. You Only Look Once (YOLO) networks [156] are a unified solution for real-time object detection by predicting bounding boxes and class probabilities simultaneously and directly from full images. YOLO divides the input images into a grid of size S and for each grid cell predicts B bounding boxes and a respective confidence score – $p(\text{object}) \times IoU_{\text{pred}}^{\text{truth}}$ –, in which $p(\text{object})$ formally defines the probability of the bounding box containing a given object, and the class-conditional probabilities – $p(c_k|\text{object})$ – by looking at the entire image and not just the regions of interest. The class-specific confidence scores for each box are obtained by multiplying these identities. The value per grid cell is then thresholded to predict the final bounding box results. The YOLO architectures have undergone multiple transformations over the years, resulting in significant improvements in performance by balancing its speed and accuracy [157].

Object detection architectures are not limited to R-CNN and YOLO based-models [158]. However, these are considered the most popular approaches, attributable to their stable performance and coherent results across multiple validated datasets [125, 145].

In the biological setting, the cell detection task is essential for characterizing samples through cell counting, phenotyping, and process automation through automated positioning of cells [159]. However, the automatic detection of astrocytes, in particular, is often challenged by their complex morphology and versatile branching structure [160]. YOLO, specifically YOLOv5, has been used to perform the automated detection of GFAP-immunolabeled astrocytes in brightfield and fluorescent microscope images [29]. Besides providing an accurate framework for the quantitative analysis of astrocytes, this architecture could also be applied to characterize their spatial distribution and extract morphological features that can be used to cluster astrocytes based on their phenotypic characteristics. The architecture of YOLOv5 comprises three consecutive sections: backbone, neck, and head. The backbone is designed to extract variable-sized feature maps from multiple convolution and pooling layers, fused in the neck section to enhance information flow and capture patterns at different spatial scales in the image. Lastly, the head section generates the output results: the bounding box for the detected objects, detection scores, and class probabilities. In this paper, the astrocytes were all classified to the same class. However, it is also possible to distinguish different astrocyte morphologies using this tool and a well-annotated dataset.

YOLOv5 has proved to be a competitive alternative to previous astrocyte detection networks, such

as FindMyCell [160] and GESU-Net [161], especially in dense cell population images. More recently, YOLOv8 [162] has been released with an architecture similar to YOLOv5 and supporting multiple vision tasks, such as object detection, segmentation, pose estimation, tracking, and classification [157]. YOLOv8 has already been successfully validated for the classification of white blood cells [163], which substantiates its applicability for astrocyte detection. However, the need for annotated astrocyte images is still the main factor hindering the development of more accurate algorithms. This problem leads to nonoptimal recall and precision values in several datasets due to the missed and incorrectly identified astrocytes, respectively.

3.2.3 Image Segmentation

Within computer vision, image segmentation entails pixel-wise classification to discern individual objects from the background [145]. Moreover, image segmentation branches into semantic and instance segmentation tasks. Semantic segmentation generally differentiates between background and foreground, assigning a binary class to each pixel. On the other hand, instance segmentation goes one step further and delineates each distinct instance appearing in the image [164]. Both semantic and instance segmentation tasks can be cast as a classification problem in which fully convolutional neural networks show remarkable performance [165].

The DeepLab and SegNet networks are based on the feature representation provided by the classification architectures ResNet-101 and VGG16, respectively. These networks possess a fully convolutional neural architecture and are designed for the semantic segmentation task. The DeepLab [166] network proposes the incorporation of atrous convolutions, atrous spatial pyramid pooling, and conditional random fields to improve the quality of the segmentation output. To increase feature resolution, the authors employed atrous convolutions to the last convolutional layers by replacing the pooling layers with upsampling filters and subsequently applying a bilinear interpolation to recover feature maps with the same resolution as the input image. On the other hand, atrous spatial pyramid pooling was employed by resampling the feature layers at different scales, thus allowing the capture of objects at multiple scales. In order to improve the localization accuracy, the conditional random fields were employed to capture fine edge details by considering the surrounding pixel labels [167]. In this paper, one ResNet and one VGG-based variant were proposed. By benchmarking with the PASCAL VOC 2012 dataset, the residual network variant achieved better semantic segmentation and state-of-the-art results.

Conversely, the development of SegNet [168] was predominantly motivated by road scene applications. This network demonstrates a unique capability to segment objects at variable sizes while exhibiting more efficient memory usage during inference compared to other architectures like DeepLab and DeconvNet. In stark contrast to DeepLab, SegNet functions by independently producing the probability of each pixel class, regardless of its neighbouring pixels. Although the validation of this network was

confined to road scene datasets, it showcased competitive performance against other state-of-the-art algorithms. Notably, beyond its intended road scene application, some researchers have successfully applied the SegNet architecture in the biological domain for tasks, such as cell segmentation, achieving satisfactory performance [169, 170].

On the other hand, the U-Net was initially conceived for biomedical image instance segmentation. U-Net diverges from typical convolutional networks by embracing a two-dimensional fully convolutional architecture [171]. Its key advantages include efficient training due to fewer parameters and the ability to achieve accurate segmentation with a smaller set of training images. The traditional U-Net consists of an encoder and a decoder. The encoder is a typical convolutional network comprising multiple sequences of two 3×3 unpadded convolutional layers, ReLU activation, and 2×2 polling layers that double the feature channels. In the decoder, pooling layers are substituted with upsampling layers, creating a roughly symmetric architecture to the encoder, forming the U-shaped structure. Furthermore, the decoder also receives information from lower layers, which is essential for the reconstruction due to the loss of information derived from the unpadded convolutions. The application of successive convolutional layers contributes to the model's accuracy by detecting fine features in the input [165].

Since the U-Net was first introduced, numerous authors have proposed additional networks based on its architecture for biomedical image segmentation, such as Stardist and Cellpose, and nnU-Net. Stardist [172] was designed to increase the accuracy of the previous models by approximating the bounding box surrounding each cell instance to a star-convex polygon. Star-convex polygons adjust much better to the cell or nucleus shape than bounding boxes and, therefore, are less prone to segmentation errors, such as falsely merging bordering cells or suppressing valid cell instances, especially in densely-packed cell images. Stardist separately predicts the probability of each pixel belonging to an object and its distance to the object boundary, thus predicting a star-convex polygon for each pixel. In addition, the Stardist algorithm was extended for nuclei segmentation in 3D fluorescence microscopy datasets by predicting star-convex polyhedra with Stardist 3D [134]. This algorithm uses a modified 3D variant of ResNet to predict the radial distances and the object probabilities instead of a U-Net, outperforming state-of-the-art algorithms, such as watershed and U-Net 3D [173].

Alternatively, Cellpose [174] successfully generates topological maps to segment cell nuclei or cytoplasm instances. In this model, the U-Net standard convolutional building blocks are replaced by residual blocks, which significantly improved the network performance and substantially outperformed Stardist on the tested datasets. The original model was trained primarily on 4',6-diamidino-2-phenylindole (DAPI)-annotated fluorescent microscopy images. However, given the diversity of dataset annotation styles, a second version of Cellpose was already developed to allow fine-tuning the pretrained model [175]. Similarly to Stardist, Cellpose also has an extension for the robust cell segmentation of 3D microscopy image data with Cellpose 3D [176], which also uses a U-Net as the backbone structure of the archi-

ture. Alternatively, Cellstitch [177] leverages the 2D segmentations from cellpose to reconstruct 3D instance segmentation predictions using optimal transport. Through this approach, it bypasses the need for end-to-end training of any 3D network.

Ultimately, nnU-Net (no-new-U-Net) is an automated, self-adapting framework for medical image segmentation based on the U-Net architecture [178]. It is designed to work with a wide variety of medical imaging tasks without requiring manual tuning. nnU-Net achieves this by using a dynamic auto-configuration, which adapts its architecture, preprocessing, and training pipeline to the specifics of a given dataset. Its out-of-the-box performance eliminates the need for extensive manual configuration or specialized domain knowledge. Furthermore, nnU-Net supports 2D and 3D semantic sementation tasks depending on the dataset. nnU-Net has become a popular tool in the medical imaging community for its robustness and ease of use, achieving state-of-the-art results across numerous datasets.

Mask R-CNN [179] takes a different approach from Stardist and Cellpose. Instead of directly predicting a shape that fits the detected object, it starts by determining the objects' bounding boxes by employing the Faster R-CNN algorithm. The network reports a parallel prediction of the binary mask and the class label in the output layer. This algorithm was not explicitly designed for biomedical applications and has a broader set of applications. Therefore, despite still being used for cell segmentation tasks [180], some authors suggest it is not as competitive as other alternative algorithms, such as Stardist, in specific data domains [172].

More recently, self-attention transformers are also being used to aggregate associative features among patch images enhancing the networks performance [181]. U-Net Transformer [182] and UT-Net [183] are two U-net-based networks that employ self-attention to enhance medical image segmentation. In addition to image segmentation, self-attention transformers have also been used for multi-class cell detection [181].

Table 3.1: Summary of the most common deep neural networks used for computer vision tasks in biological image analysis.

Neural Network	Tasks	Dimensionality	Evaluation metrics	Breakthroughs/ Innovations	Citation
VGG	• classification • localization	2D	• top-1 error • top-5 error	Significant improvement on the prior state-of-the-art configurations. Increased depth, with 16 to 19 layers.	[146]
ResNet	• classification	2D	• top-1 error • top-5 error	Easier to optimize. Higher accuracy. Increased depth (up to 8x deeper than VGG nets).	[147]
R-CNN	• object detection	2D	• mAP	Combination of RPNs with CNNs. Small amount of annotated data.	[153]
Faster R-CNN	• object detection	2D	• top-5 error	Higher efficiency compared to R-CNN. End-to-end optimization.	[154]
YOLO	• object detection	2D and 3D	• mAP • IoU	Real-time prediction. End-to-end optimization.	[156]
DeepLab	• semantic segmentation	2D	• mean IoU	Convolution with upsampled filters, atrous spatial pyramid pooling, and combination of deep CNNs with probabilistic graphical models.	[166]
SegNet	• semantic segmentation	2D	• accuracy • mean IoU • F1-score	More efficient memory usage during inference.	[168]
U-Net	• semantic segmentation • instance segmentation	2D and 3D	• IoU • wrapping error • rand error • pixel error	Increased learning capacity from few training images. Yields more precise segmentations.	[171]
nnU-Net	• semantic segmentation	2D and 3D	• F1-score	Self-configuration based on the dataset. No need for hyperparameter tuning. Maximize performance with limited training data.	[178, 184]
StarDist	• instance segmentation	2D and 3D	• IoU • mAP • MAE	Cell nuclei localization via star-convex polygons (in opposition to bounding boxes)	[134, 172]
Cellpose	• instance segmentation	2D (and 3D)	• IoU • mAP • mean IoU	Learning from a wide-variety of microscopy images. Bypasses retraining or parameter adjustments.	[174, 176]
Cellstitch	• instance segmentation	3D	• precision • recall • mAP	Reconstruction 3D cell segmentations via layer-wise alignment of 2D segmentation results.	[177]
Mask R-CNN	• instance segmentation	2D	• mAP	Bounding box prediction followed by object segmentation.	[179]
Bright2Nuc	• pixel-wise regression	3D	• average Pearson correlation	Integrated pipeline to infer in silico labeling from brightfield microscopy images, and conduct nuclei segmentation and phenotype classification.	[185]
InstantDL	• classification • instance segmentation • semantic segmentation • pixel-wise regression	2D and 3D	• mean IoU • AUC • median pixel-wise Pearson correlation	Integrated pipeline to perform multiple computer vision tasks.	[186]

4

Materials and Methods for Cell Culturing and Profiling

Contents

4.1 Primary Cultures of Mouse Cortical Astrocytes	36
4.2 Cell Cultures	36
4.3 Cell Culture Characterization	37

4. MATERIALS AND METHODS FOR CELL CULTURING AND PROFILING

Wet laboratory experiments were undertaken in facilities of the Biomedical Center Munich (BMC) at the Ludwig Maximilian University of Munich (LMU), Germany.

The complete list of all used chemicals, materials and software may be found in the Appendix A.

4.1 Primary Cultures of Mouse Cortical Astrocytes

Cortical GM astrocytes were isolated and cultured from postnatal day 5-7 (p5-7) wild type (WT) and transgenic Actin::GFP mice, following a reference protocol [187] with minor modifications. Whole brains were extracted from decapitated mice and transferred to a culture dish containing 10 mL of ice-cold dissection medium (1X HBSS containing 10 mM HEPES). Brains were coronally sectioned at the optic chiasm, discarding the anterior portion and the midbrain. Each brain was hemisected, and the hypothalamus, striatum, and cortical white matter were excised, followed by the removal of meninges. Cortical GM was mechanically dissociated in 3 mL of dissection medium and centrifuged at 350 rpm for 5 minutes. Cell pellet was resuspended in 5 mL of astrocyte medium (DMEM/F12 (1:1), 10% fetal bovine serum (FBS), 100U/mL penicillin–streptomycin (P/S), supplemented with 1X B27, 0.45% glucose and 1X GlutaMAX) and plated in a T25 flask. Cells were cultured for 7 days under standard incubation conditions (37°C, 5% CO₂). For passaging, cells were incubated at standard incubation conditions for 8 minutes with 1 mL of 0.05% trypsin. Cell solution was centrifuged at 350 rpm for 5 minutes with 1:4 astrocyte medium. Cell pellet was resuspended in astrocyte medium and filtered through a fluorescent-activated cell sorting (FACS) filter to avoid culture of cell aggregates.

4.2 Cell Cultures

4.2.1 2D Cell Cultures

Cell cultures were prepared in monolayer PDL-coated glass or embedded in hydrogels. 2D cell cultures were prepared on PDL-coated glass coverslips (see Appendix B.1) or PDL-coated glass-bottom 24-well plates (IBIDI) with a final concentration of 25.000 cells per well. The cell count was determined using the trypan blue exclusion method, with a 1:1 ratio of cell suspension to trypan blue. The cells were counted in Neubauer chambers under transmitted light microscopy. Cultures were supplied with 1 mL of astrocyte medium and maintained in standard incubation conditions for 7 days.

4.2.2 Cell Embedding in 3D Sodium Alginate Hydrogels

Alginate hydrogels, medium viscosity guluronate (MVG) and very low viscosity guluronate (VLVG), were prepared at a concentration of 0.5% (w/v) in 1X PBS from a 2% (w/v) stock solution (NovatachTM, guluronic acid ≥ 60%). Alginate solutions were mixed with cortical GM cells to achieve a final concentration of approximately 1.000.000 cells/mL. Cell-containing alginate precursor solution was added

to glass-bottom mini-wells (see Appendix B.2) in a 24-well plate in volumes of 15 µL. Hydrogels were covered with a dialysis membrane and crosslinked with calcium chloride solution (CaCl_2), 100 mM for MVG and 175 mM for VLVG, for 10 minutes immediately after casting at 22°C, room temperature (RT). Mini-wells were flipped upside down 1 minute after the addition of calcium chloride solution, to avoid cell sedimentation. Cell-containing hydrogels were supplemented with astrocyte medium and stored at standard incubation conditions.

4.2.3 Cell Embedding in 3D FibrinVLVG and Fibrin Hydrogels

The preparation of FibrinVLVG and fibrin hydrogels was consistent across all conditions, differing only in the composition of the thrombin solution and fibrinogen solution, as described on Table 4.1. The thrombin solution was added to the cell pellet, followed by the fibrinogen solution, in a 1:1 ratio. The cell-containing hydrogel solutions were prepared with a final cell concentration of 1.000.000 cells/mL. For hydrogel casting in mini-wells, 15 µL of the cell-containing hydrogel precursor solution was pipetted into glass-bottom mini-wells in a 24-well plate. Whereas for hydrogel casting into glass-bottom 24-well plates, 50 µL drops of the cell-containing hydrogel precursor solution were casted the middle of each well. Hydrogels gelated at RT for 10 minutes. FibrinVLVG hydrogels were crosslinked 1 mL of calcium chloride for 10 minutes. Hydrogels were supplemented with astrocyte medium and further incubated under standard conditions.

Table 4.1: Composition of thrombin and fibrinogen solutions for Fibrin and FibrinVLVG hydrogels casting.

Hydrogel	Fibrinogen Solution	Thrombin Solution
Fibrin	1X PBS 6 mg/ml fibrinogen 0.16 mg/mL aprotinin	astrocyte medium 4 U/mL thrombin
5 mM Ca^{2+} FibrinVLVG	1X PBS 1% (w/v) VLVG 6 mg/ml fibrinogen 0.16 mg/mL aprotinin	astrocyte medium 4 U/mL thrombin 10 mM CaCl_2
50 mM, 100 mM and 175 mM Ca^{2+} FibrinVLVG	1X PBS 1% (w/v) VLVG 6 mg/ml fibrinogen 0.16 mg/mL aprotinin	astrocyte medium 4 U/mL thrombin

4.3 Cell Culture Characterization

4.3.1 Immunocytochemistry

Cells were fixed at 22°C, RT, for 15 minutes with 1 mL of 4% paraformaldehyde (PFA) in 1X HBSS. Cells were washed thrice for 15 minutes with 1 mL of 1X HBSS, before incubation with the blocking

4. MATERIALS AND METHODS FOR CELL CULTURING AND PROFILING

buffer (1X PBS, 2% bovine serum albumin (BSA), 0.5% Triton X-100) to permeabilize the cells and reduce nonspecific antibody binding for 1 hour at RT. Cells were incubated with 0.5 mL of the primary antibodies solution (1X HBSS, chicken anti-GFAP 1:1500, rabbit anti-SOX9 1:1000) for 24 hours at -4°C. Cells were washed thrice for 15 minutes with 1X HBSS and incubated for 2 hours at RT, or overnight at -4°C, with 0.5 mL of the secondary antibodies solution (1X HBSS, alexa fluor (AF) 647 goat anti-chicken IgY H&L 1:1000, AF594 donkey anti-rabbit IgY H&L 1:1000). Cells were washed thrice for 15 minutes with 1X HBSS. DAPI (1:1000) was added to the washing solution on the second washing period.

4.3.2 LIVE/DEAD Viability Assay

Cells were washed once with 1 mL 1X PBS and stored under standard incubation conditions with 0.5 mL of solution containing 1X propidium iodide (PI), 10 µM Calcein-AM and Hoechst 33342 1:1000 in 1X HBSS for 45 minutes. Cells were washed with 1X PBS and fed with astrocyte medium for immediate live imaging at the confocal microscope. Live cells were identified by green fluorescence from Calcein⁺, while dead cells were marked by PI staining.

4.3.3 Confocal Imaging of 3D Astrocyte Cultures

Mini-well cultures were imaged at the LSM710 laser-scanning confocal (Carl Zeiss). Digital images were acquired using the ZEN software (Carl Zeiss) at 10X or 20X. Images were acquired with immersion on 1X HBSS. Glass-bottom well-plates were imaged at a STELLARIS 8 FALCON on DMi8 (Leica Microsystems) confocal microscope. Digital images were acquired using the LAS-X software (Leica Microsystems), at 10X or 20X dry. Frame size was fixed at a resolution of 1024×1024 pixels, with a pixel dwell time of ranging between 2 and 3 µs. Zoom was varied between x0.75 and x1. Step size in the vertical direction was fixed at 2 µm.

4.3.4 Cell Morphology and Markers Expression Quantification

Astrocytic cells were identified by the expression of the nuclear marker SOX9. Astrocytes' morphology was characterized by visual inspection of green fluorescent protein (GFP) and GFAP channels and distinguished into three subtypes: round – cells with no visible branching; branched – cells with small branches and/or only 1 or 2 large branches, or branches that expand concentrically rather than radially; highly branched (hBranched) – cells with at least 3 large branches expanding radially. Additionally, cell clusters were characterized by cell aggregates containing at least three DAPI⁺ nuclei and not exhibiting branching structures. SOX9⁺ nuclei aggregates with at least three nuclei which exhibit astrocyte-like branched morphologies fall into the categories of branched or hBranched, according to the previous description. Cell cultures were quantified regarding the percentage of astrocytes (SOX9^{+/DAPI⁺), percentage of GFAP⁺ expressing cells (GFAP^{+/DAPI⁺) and percentage of reactive astrocytes (GFAP^{+/SOX9⁺).}}}

5

Computational Solution for 3D Cell Culture Characterization

Contents

5.1 Deep Learning for Nuclei Segmentation	40
5.2 GUI for 3D Cell Culture Image Annotation	51
5.3 Deep Learning for Cell Classification	55

This chapter explores the *in silico* methods developed throughout the project. Section 5.1 delves into the DL methods used for cell nuclei segmentation, encompassing 2D and 3D approaches. Section 5.2 explores the main features of the GUI developed for 3D z-stack assisted image annotation. The guidelines for the GUI-assisted annotation are further described in Appendix C. In addition, Section 5.3 includes the description of the dataset obtained for cell classification and the proposed approach for cell morphology classification.

5.1 Deep Learning for Nuclei Segmentation

Nuclei segmentation – a process more complex than nuclei detection – is a crucial for studying the cellular phenotypes. The nucleus, as the control center of the cell, holds the genetic material. By accurately identifying and segmenting cell nuclei, researchers can examine key cellular features such as size, shape, and distribution, which are important for cytological, histological, and pathological analysis [188]. Furthermore, these cellular features provide valuable insights into how cells behave under different conditions, how they respond to environmental changes, and how they interact with their surroundings [189,190]. This process is essential for studying cellular variability and the phenotypic diversity that emerges in response to various stimuli or during different stages of development.

As highlighted in previous chapters, the manual classification of nuclei using software like Fiji is still laborious and complex, while one-size-fits-all DL models to segment nuclei still have limited generalization capacity to handle specific data such as neural tissue, especially on the 3D scenario [29,30]. In this project we focus on optimizing nuclei segmentation models for astrocyte cultures in 3D hydrogels. In Subsection 5.1.1, a baseline solution is proposed, which involves performing 2D instance segmentation of nuclei by fine-tuning a model of Mask R-CNN described in the literature to our dataset and comparing the results to widely used architectures: stardist and cellpose. In Subsection 5.1.2, the semantic segmentation of 3D z-stack images using nnU-Net models trained from scratch is attempted, as well as Stardist 3D and a variant of cellpose adapted to 3D scenarios. Both StarDist and Cellpose were designed primarily for 2D image analysis, with later adaptations for 3D. However, their performance in 3D datasets is less extensively validated, with fewer studies and benchmarks compared to their well-documented effectiveness in 2D [191].

5.1.1 Baseline Solution

For the baseline solution, the 2D instance segmentation of nuclei using Mask R-CNN is proposed. The dataset for fine-tuning Mask R-CNN encompasses 21 bidimensional images (1024×1024 pixels, $591.05 \mu\text{m}^2$) derived from the DAPI channel. These images represent maximum intensity projections of z-stack images obtained from 3D sodium alginate hydrogel cell cultures of murine astrocytes, captured

by confocal microscopy. The images were processed and analyzed as detailed in Appendix D.1.

Mask R-CNN processes 2D images as input and generates binary masks for each segmented nucleus, facilitating straightforward nuclei quantification. The architecture was evaluated by employing different pretrained weights and fine-tuning strategies.

Initially, the performance of Mask R-CNN was assessed using pretrained weights provided by [180], derived from training on the 2D nuclear instance segmentation dataset from the nuclear detection challenge 2018 (DSB2018) [192], and the general purpose dataset ImageNet [144]. Subsequently, the network’s performance was further refined by fine-tuning the model on the given dataset. Careful calibration of the training-validation ratio and cross-validation folds is crucial to balance statistical reliability and computational efficiency due to the limited dataset size. Therefore, two k-fold cross-validation experiments were conducted, using $k = 3$ and $k = 7$.

Additionally, the impact of data augmentation strategies on the model’s performance was also investigated. To this end, multiple strategies were assessed, including feature scaling, standard normalization, horizontal and vertical flips, Poisson noise addition, rotations, intensity amplification, contrast and brightness adjustments, gamma correction, thresholding, and Gaussian blurring. These augmentations were applied randomly modifying training and validation images at predefined rates. Notably, the training subset was augmented indirectly, as the model was trained using the same subsets as in non-augmented scenarios, with the augmentations applied dynamically during training [180].

Mask R-CNN Performance across Multiple Models

The performance of the Mask R-CNN architecture was evaluated across six distinct models, as summarized in Table 5.1. To evaluate the performance of each model, the recall, precision, mAP, mean IoU, F1-score were computed. The metrics were calculated relative to a *IoU* threshold value, $\tau = 0.2$. Additionally, there was also computed the prediction ratio (PR),

$$PR = \frac{TP + FP}{TP + FP + FN}, \quad (5.1)$$

where the numerator corresponds to the number of model predictions and the denominator to the number of ground truth predictions. The PR metric is independent of the *IoU* value and estimates how many nuclei the model predicts in comparison to the ground truth annotation. The number of ground truth predictions aggregated as a single nuclei prediction was also computed as the aggregation ratio (AR),

$$AR = \frac{\text{aggregated predictions}}{TP + FP + FN}, \quad (5.2)$$

where the numerator computes the number of ground truth instances aggregated into a single prediction by the model.

5. COMPUTATIONAL SOLUTION FOR 3D CELL CULTURE CHARACTERIZATION

Table 5.1: Mask R-CNN models used for 2D instance segmentation.

Model	Cross Validation	Data Augmentation	Description
<i>imagenet</i>	–	–	General purpose model trained with the ImageNet dataset.
<i>dsb2018</i>	–	–	Model trained with the DSB2018 dataset.
<i>ftk3</i>	3-fold	No	Models obtained by fine-tuning the <i>dsb2018</i> model to our dataset.
<i>ftk7</i>	7-fold	No	
<i>aftk3</i>	3-fold	Yes	Models obtained by fine-tuning the <i>dsb2018</i> model to our dataset after data augmentation.
<i>aftk7</i>	7-fold	Yes	

From all the tests performed, *imagenet* model was the least successful. Its recall – the probability of a segmentation accurately segmenting a nuclei – was of only 20.69% and the precision – the probability of a nuclei being detected – was of 13.32%, whereas the $mAP_{0.2}$ was of only 8.82%. Furthermore, there were only identified 485 true positive segmentations out of the 2034 nuclei segmented in the annotated dataset, which indicates a poor sensitivity. In addition, 93.12% of the predictions had *IoU* coefficients lower than 20% with their respective ground truth.

Using the *dsb2018* model – already trained to detect cell nuclei –, the nuclei predictions were significantly more accurate. The precision was of 79.13%, however the number of FP observations was still considerably high, leading to a recall of only 47.24% and $mAP_{0.2}$ of 42.01%. On the other hand, the mean *IoU* of the predictions was 41.65% and the *AR* correspondend to 16.28%, indicating that this model was overpredicting the nuclei size.

Fine-tuning the model to our dataset significantly improved the segmentation task results. Comparing the results from the 3-fold and 7-fold cross-validations (*ftk3* and *ftk7* models), the recall and the $mAP_{0.2}$ of *ftk3* was higher, however its precision was lower than for *ftk7* model (Table 5.2). Even though *ftk3* model made more nuclei predictions they were not as specific as the predictions of *ftk7*, and multiple nuclei were aggregated in the same prediction, leading to a higher percentage of the *AR* value. On the other hand, the mean *IoU* was comparable between these models. The values of the computed metrics were comparable between the models obtained with data augmentation strategies in the training (*aftk3* and *aftk7*) and its non-augmented homologous (Table 5.2).

Considering all the metrics, *ftk3* was the proposed model that performed better in the given dataset. Despite higher *AR* than *ftk7* and *aftk7*, *ftk3* was able to predict more closely the total number of nuclei with outstanding recall and $mAP_{0.2}$.

Table 5.2: Summary of the models performance regarding the $recall_{0.2}$, $precision_{0.2}$, $mAP_{0.2}$, mean IoU coefficient, PR and AR .

Model	$recall_{0.2}$	$precision_{0.2}$	$mAP_{0.2}$	IoU	PR	AR
<i>imagenet</i>	0.21	0.13	0.09	0.27	2.15	0.008
<i>dsb2018</i>	0.47	0.79	0.42	0.42	0.52	0.16
<i>ftk3</i>	0.90	0.94	0.85	0.63	0.88	0.047
<i>ftk7</i>	0.84	0.96	0.80	0.64	0.80	0.027
<i>aftk3</i>	0.85	0.94	0.81	0.64	0.85	0.051
<i>aftk7</i>	0.85	0.96	0.81	0.65	0.82	0.026

Comparing *ftk3* model with Stardist 2D and Cellpose 2D

To corroborate the results from the Mask R-CNN architecture, *ftk3* model was compared to Stardist 2D and Cellpose 2D, without fine-tuning (Table 5.3).

The performance of Stardist 2D, using a model trained with the nuclei segmentation data from the DSB2018, was very competitive with the results obtained with Mask R-CNN. The PR indicates that Stardist 2D tends to over estimate the effective number of nuclei, in contrast to Mask R-CNN. On the other hand, it does not discriminate individual instances as well, exhibiting an AR of 4.85% and predicting more false positives, which lowers its precision.

Contrastingly, Cellpose 2D was not as effective as the two previous architectures. It presented several outliers to extreme under-estimation or over-estimation of the number of nuclei, and a standard deviation of 707.47 nuclei. Also due to this poor estimation, the PR is considerably elevated and its precision is markedly low.

In Figures 5.1A and 5.1B the similarity between the performances of the fine-tuned models using the Mask R-CNN architecture and the Stardist 2D is clearly illustrated. In addition, Cellpose 2D notably underperforms the remaining models. Furthermore, in Figures 5.1C are illustrated the ground truth masks and the predictions from *ftk3* model, Stardist 2D and Cellpose 2D, respectively. This example, illustrates the inadequacy of Cellpose 2D to generalize to all images, in contrast to the other models.

Table 5.3: Validation of the architectures performance regarding the $recall_{0.2}$, $precision_{0.2}$, $mAP_{0.2}$, IoU coefficient, PR and AR .

Architecture	$recall_{0.2}$	$precision_{0.2}$	$mAP_{0.2}$	IoU	PR	AR
Mask R-CNN	0.90	0.94	0.85	0.63	0.88	0.047
Stardist 2D	0.88	0.86	0.77	0.65	1.09	0.049
Cellpose 2D	0.79	0.27	0.25	0.59	4.68	0.075

5. COMPUTATIONAL SOLUTION FOR 3D CELL CULTURE CHARACTERIZATION

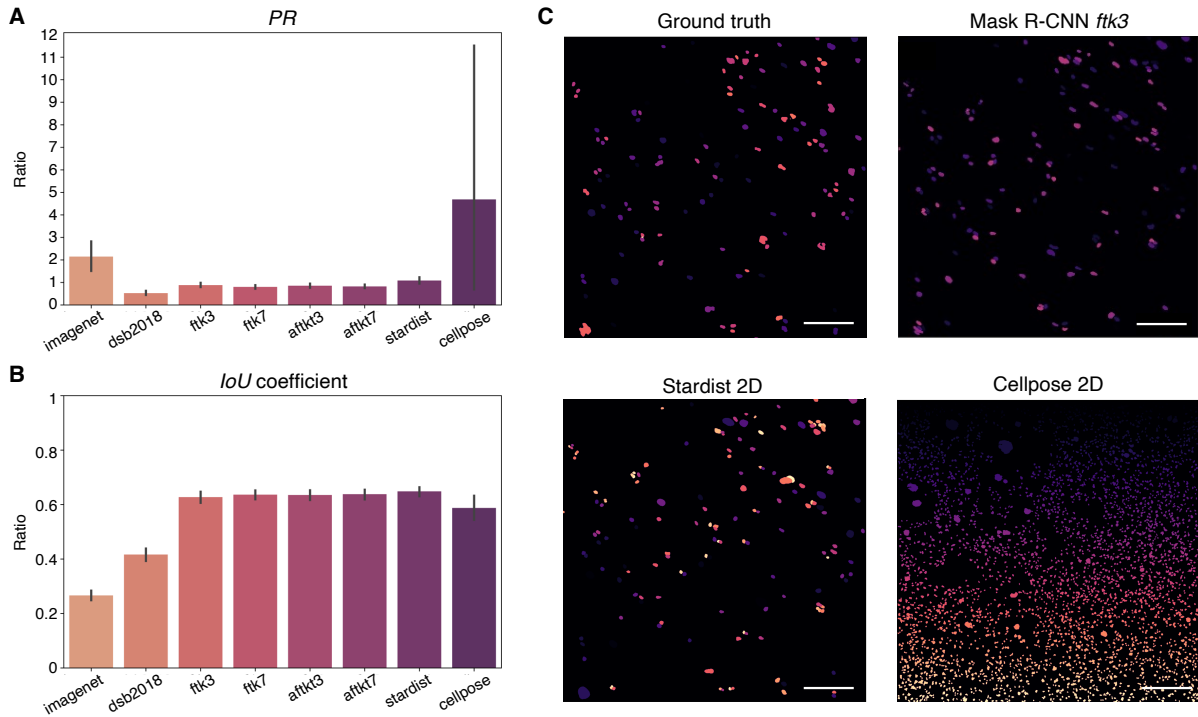


Figure 5.1: Summary and visualization of the performance of the tested models and architectures for 2D nuclei segmentation. **(A)** Bar plot of the *PR* values across the multiple models tested; **(B)** Bar plot of the *IoU* coefficient across the multiple models tested; **(C)** Comparison of the ground truth labels and predicted masks across multiple segmentation models. The colors of the masks shown in the images are arbitrary and do not correspond to any specific correlation or property. Scale bars = 100 μm . Error bar in the graphics correspond to the 95% confidence interval.

5.1.2 Improved Solution

The improved solution for the nuclei segmentation task explored in this project involved performing 3D nuclei segmentation training using deep learning models. As noted in the literature, 3D nuclei segmentation is less developed compared to 2D approaches. Nevertheless, the Stardist 3D and Cellstitch algorithms were identified as viable options for instance nuclei segmentation, aligning with the objectives of this work.

Specifically, Cellstitch [177] employs a 2D approach leveraging the Cellpose 2D algorithm to segment individual cell instances in an initial step. Subsequently, a complementary algorithm reconstructs 3D segmentations from z-stack images. Consequently, the input to this network remains bi-dimensional rather than three-dimensional, differing from the 3D approach pursued in this project. Contrastingly, Stardist 3D directly processes 3D images, generating instance segmentations autonomously. This feature makes Stardist 3D the best architectural framework for addressing the challenges at hand.

An initial assessment of the performance of these models was conducted using a z-stack image dataset composed of 16 images ($512 \times 512 \times 101$ pixels, $200.05 \mu\text{m}^2 \times 200 \mu\text{m}$). These multichannel im-

ages contained DAPI and GFAP channels, representing nuclei and astrocyte morphology, respectively.

The dataset was processed to generate four additional variants by modifying preprocessing methods, feature selection strategies (regarding channel selection), and data augmentation techniques applied to the raw images. Preprocessing was performed manually using Fiji and included strategies to reduce background noise and optimize contrast levels. Data augmentation was applied at a random rate of 0.3 and included 90° rotations, horizontal and vertical flips, and zoom operations ranging from $\times 0.5$ to $\times 2$. All augmented images were ensured to be distinct to prevent overfitting during subsequent model training.

The datasets generated and their characteristics are summarized in Table 5.4. The mean and standard deviation values of the dataset images' intensity were also analyzed using the Shapiro-Wilk test to assess the normality of their distributions (Figure 5.2). For dataset 1, dataset 2, and dataset 3, the null hypothesis of the Shapiro-Wilk test was accepted, indicating that the intensity values follow a normal distribution. However, the data augmentation strategies applied to dataset 4 and dataset 5 altered the datasets in such a way that their intensity distributions no longer conformed to a normal distribution.

Table 5.4: Depiction of the datasets generated for nnU-Net model optimization.

Features	dataset 1	dataset 2	dataset 3	dataset 4	dataset 5
Images	preprocessed	raw	raw	raw + augmented	raw + augmented
Size	16	16	16	120	150
Selected Channels	DAPI + GFAP	DAPI + GFAP	DAPI	DAPI	DAPI
Augmentation	–	–	–	rotations, vertical and horizontal flips	rotations, vertical and horizontal flips, zoom
Digital Size (512,512,101,Z)	Z = 2	Z = 2	Z = 1	Z = 1	Z = 1
Training FOV Range (μm^2)	200.63	200.63	200.63	200.63	100.31 – 802.50
nnU-Net model	model 1	model 2	model 3	model 4	model 5

Nevertheless, testing the performance of Stardist 3D and Cellstitch with dataset 1 without fine-tuning the models yielded results significantly below the expected values for accurate 3D nuclei segmentation. From best-performing scenarios in the literature, Stardist 3D achieved a $mAP_{0.1}$ of 0.94 [134] and Cellstitch a $mAP_{\{0.3,0.5,0.7\}}$ of 0.66 [177]. However, Stardist 3D and Cellstitch obtained $mAP_{0.2}$ values of 0.48 and 0.19, respectively, when tested on dataset 1.

Alternatively, as explored in Chapter 3, nnU-Net is an advanced deep learning framework specifically designed for medical image segmentation tasks. Based on the widely recognized U-Net architecture, nnU-Net distinguishes itself by automating the model configuration process and supporting various data

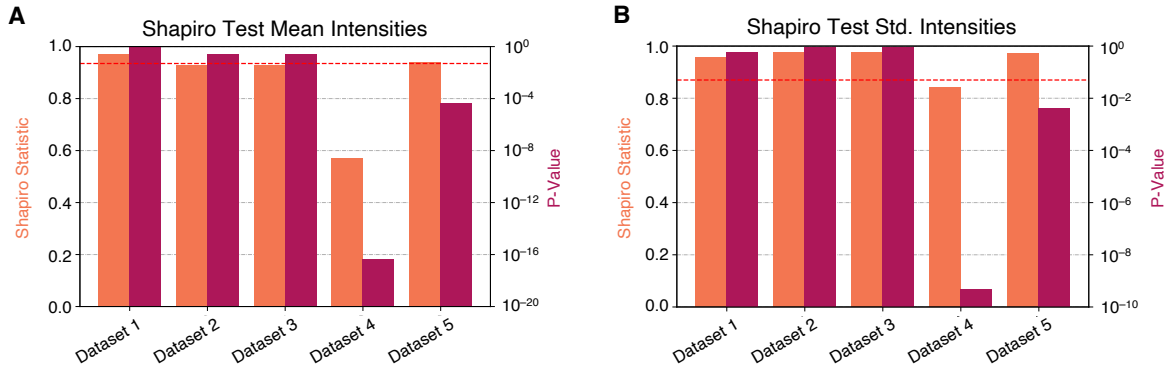


Figure 5.2: Shapiro test analysis each dataset images, regarding **(A)** Mean values, and **(B)** Intensity standard deviation values of images' intensity. A p-value below 0.05 threshold (---) indicates the dataset significantly deviates from a normal distribution.

input types, including 2D and 3D images.

Since nnU-Net produces semantic segmentations, a postprocessing step was required to achieve cell instance segmentation. For this purpose, a simple threshold-based algorithm leveraging 3D components was developed, as illustrated in algorithm 1.

Algorithm 1 Instance Segmentation Algorithm

```

1: procedure INSTANCESEGMENTATION(nnunet_output)
2:   background  $\leftarrow$  find pixels where nnunet_output = 0
3:   foreground  $\leftarrow$  find pixels where nnunet_output = 2
4:   unknown  $\leftarrow$  find pixels where nnunet_output = 1
5:   connected_components  $\leftarrow$  cc3d(foreground)            $\triangleright$  Detect connected components in the foreground
6:   local_maxima  $\leftarrow$  peaks(connected_components)       $\triangleright$  Find local maxima within the components
7:   instance_segmentation  $\leftarrow$  watershed(connected_components, local_maxima)
8:   return instance_segmentation                          $\triangleright$  Return the segmented instances
9: end procedure

```

Additionally, the cell nuclei in the dataset were individually segmented using Napari – which facilitates preliminary segmentation with Stardist 2D and subsequent manual correction (see Appendix D.2). The obtained segmentations, along with the original dataset, were further used to train and test a model with nnU-Net and to compare its performance against the Stardist 3D and Cellstitch algorithms. The nnU-net models were trained in 5-fold cross-validation experiments assuring the training and testing datasets did not overlap.

Comparing nnU-Net to Stardist 3D and Cellstitch

Across all assessed metrics, nnU-Net consistently outperformed its counterparts (Figure 5.3). Not only were its mean values closer to the optimal, but the 95% confidence intervals were narrower, indicating a higher likelihood that 95% of all observations fall within a smaller range closer to the high mean value.

Based on these observations, we confidently conclude that training nnU-Net from scratch with the manually annotated dataset yields superior performance compared to open-source models. Consequently, nnU-Net holds significant potential for further improvement. Enhancing the training dataset could elevate its performance even further, enabling it to achieve a more generalizable paradigm.

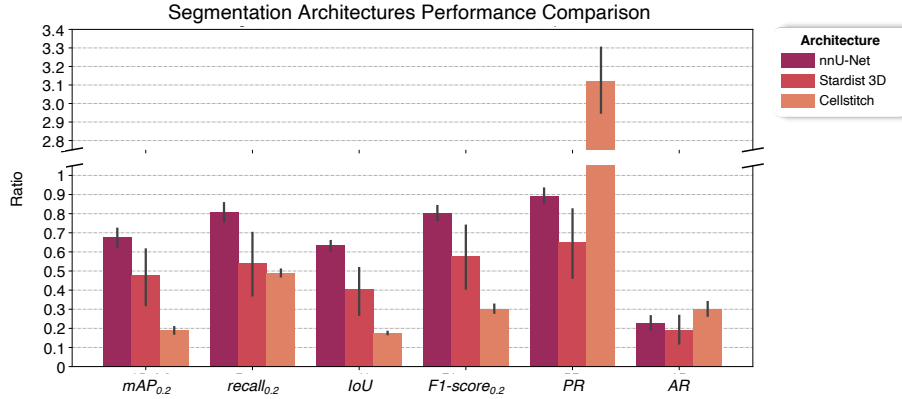


Figure 5.3: Comparison of nnU-Net, Stardist 3D and Cellstitch, regarding the performance metrics: $mAP_{0.2}$, $recall_{0.2}$, IoU , $F1\text{-score}_{0.2}$, PR , and AR . Error bar: 95% confidence interval.

Optimizing nnU-Net Models' Performance

The performance of nnU-Net was further optimized by adjusting the input dataset, as illustrated in Table 5.4. The comparison metrics used for evaluation were the same as those employed to compare the performance of the other architectures. Each dataset was used to train the nnU-Net model using a 5-fold cross-validation method, resulting in five distinct comparison models.

Since nnU-Net is an auto-configuring architecture, no further adjustments to the model's hyperparameters were necessary. The fixed parameters included the optimizer, learning rate, and loss function. Furthermore, the batch-size intensity normalization, and network topology were automatically defined by nnU-Net through rule-base parameters considering each dataset fingerprint [178]. The results obtained after this training process are summarized in Figure 5.4, where each model number corresponds to the respective dataset number in Table 5.4.

Comparing *model 1* and *model 2*, where the only difference between the datasets was the preprocessing of the raw data, it was observed that, in general and contrary to initial expectations, the raw data led to better performance results. These results suggest that the raw data might facilitate better model generalization, making the model more adaptable to unseen data. However, the *AR* increased slightly in *model 2*, which could be attributed to noise in the untreated images, causing nuclei instances to merge.

When the GFAP channel was excluded from the training data (*model 3*), the overall performance of the model decreased substantially. Despite this, the ideal dataset should include only the DAPI channel,

5. COMPUTATIONAL SOLUTION FOR 3D CELL CULTURE CHARACTERIZATION

as it is more likely to be generalizable to unseen datasets. A model trained with both the DAPI and GFAP channels is only applicable to test images that also include both channels. This result suggests that while the cytoplasm channel may aid in the accurate prediction of nuclei positions, it could negatively impact nuclei separation, as indicated by the decrease of the *AR*.

The data augmentation strategies applied to datasets 4 and 5 played a crucial role in improving model performance without the GFAP channel. The performance of *model 4* and *model 5* was in general similar. However, *model 5* demonstrated a preference, as it was trained on a more generalizable dataset, which included images amplifications as a data augmentation strategy. The zooming applied to dataset 5 allows *model 5* to better adapt to images with varying field of view (FOV), which is particularly useful for assessing unseen datasets.

Nevertheless, these observations generally have low statistical significance (Figure 5.5), making it difficult to confidently assert that one model outperforms the other. However, when comparing *model 5* to the remaining models, its outperformance regarding the *PR* metric is consistently statistically significant on the parametric assumption (*t*-test), except in the comparison with *model 4*. Contrastingly, in the non-parametric assumption, which is necessary since dataset 5 is not normally distributed (Figure 5.2), there was not verified statistical significance. Other metrics may also be influenced by the *IoU* threshold, as discussed previously.

The performance of the models was evaluated using a ranking system for each metric, where models were ranked from 1 to 5 based on their performance, with 1 indicating the best performance and 5 the worst. For this ranking, only the mean values (Table 5.5) were considered, and the *F1-score* was excluded, as it is a weighted average of the precision and recall. According to this scoring system, *model 5* was deemed the best performing model among the trained instances, achieving an impressive 99.5% value of PR.

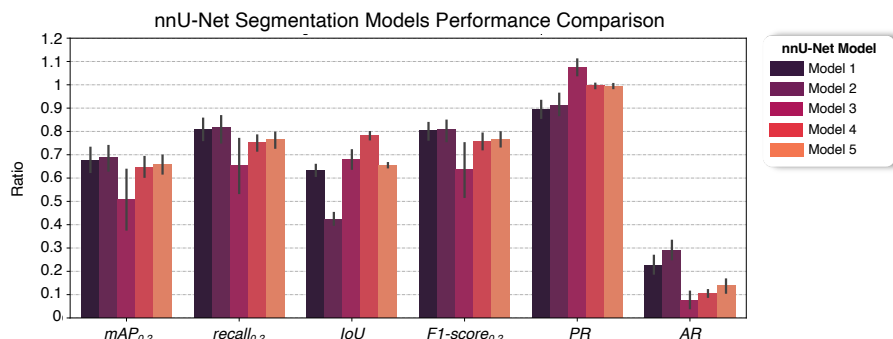


Figure 5.4: Comparison of nnU-Net models trained on different datasets, regarding the performance metrics: $mAP_{0.2}$, $recall_{0.2}$, IoU , $F1\text{-score}_{0.2}$, PR , and AR . Error bar: 95% confidence interval.

5.1 DEEP LEARNING FOR NUCLEI SEGMENTATION

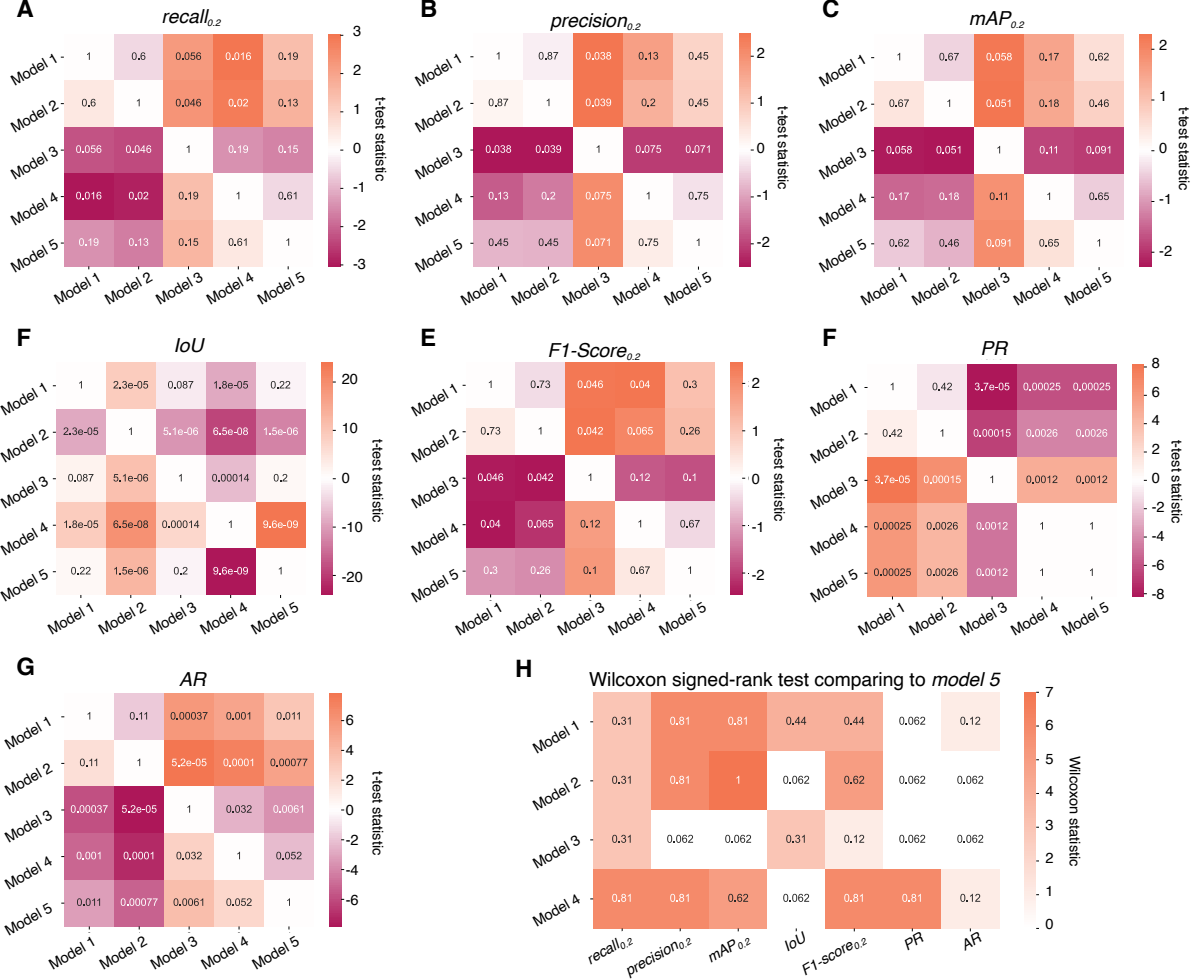


Figure 5.5: Comparison of the performance of various nnU-Net segmentation models, regarding seven performance metrics: $recall_{0.2}$, $precision_{0.2}$, $mAP_{0.2}$, IoU , $F1\text{-score}_{0.2}$, PR , and AR . (A – G) T -test statistic from independent tests comparing the model in the corresponding row with the model in the column. The heatmap scale indicates the t -test statistic value. (H) Wilcoxon signed-rank test for non-parametric comparison of model 5 with respective models in each row. The numerical values within the heatmaps represent the p-values for the respective statistical comparisons.

Table 5.5: Scoring of trained nnU-Net models following a ranking system of each of the evaluation metrics.

Model	$recall_{0.2}$	$precision_{0.2}$	$mAP_{0.2}$	IoU	PR	AR	Score
model 1	2	2	2	4	5	4	20
model 2	1	1	1	5	4	5	17
model 3	5	5	5	2	3	1	21
model 4	4	4	4	1	2	2	17
model 5	3	3	3	3	1	3	16

5. COMPUTATIONAL SOLUTION FOR 3D CELL CULTURE CHARACTERIZATION

Testing nnU-Net Models on Unseen Datasets

The performance and efficiency of *model 5* in segmenting nuclei on the DAPI channel was further validated by testing it on a diverse set of z-stack image datasets obtained under different conditions. These datasets included 3D hydrogel culture conditions with murine and human iPSCs (hiPSCs)-derived astrocytes, cast as single cells following the same protocol used for the training dataset but performed by different operators, as well as tissue samples from murine embryonic tissue and adult murine cortical tissue¹. The datasets also exhibited heterogeneity in terms of FOV, pixel ratio, and anisotropy ratio.

This validation aimed to assess whether *model 5* is generalizable enough to predict nuclei instances accurately across different biological image types. However, a thorough analysis of its performance could not be fully carried out due to insufficient testing data from diverse conditions. Specifically, the image characteristics such as FOV and anisotropy do not vary within the same dataset, but rather across different datasets. Therefore, it is inaccurate to assume that these parameters are directly related to the model's performance, as these factors could already be influenced by the inherent appearance of the images themselves.

Four different datasets were tested, as detailed in Table 5.6. To maintain consistency with the training data, the image properties of the testing datasets were kept within the range of those observed in the training dataset. Figure 5.6 illustrates the maximum intensity projection over a volume of 12 µm in depth for each dataset. A raw visual inspection of the images reveals a close resemblance between the cells cultured in 3D hydrogels across the various datasets. Furthermore, the brain cortex images of murine tissue share some similarities with these datasets, though the cells in the brain cortex are packed more

Table 5.6: nnU-Net testing datasets, spanning from cultures in hydrogels and murine tissue samples, accross different FOV and anisotropies.

Dataset Features \	Cultures in 3D Hydrogel			Tissue	
	Training	Murine-derived Astrocytes	hiPSC-derived Astrocytes	Murine Embryo	Murine Cortex
Cell Origin	p5-7 ADLH1L1 Mice	p5-7 Actin::GFP Mice	hiPSC p30-35	Embryo WT Mice	Cortex Mice
Dataset Size	N = 16	N = 13	N = 9	N = 9	N = 13
Type of cells	Astrocytes	Astrocytes	Astrocytes	Neural cells	Neural cells
Organization	Single Cell	Single Cell	Single Cell	Packed Cells	Packed Cells
Image FOV (µm ²)	100.31 – 802.50	387.88	591.05	228.12	122.17 – 400.29
Resolution (pixels/µm)	2.55	1.32	1.73	4.82	1.54
Anisotropy (X,Y,Z)	0.19 – 1.52	0.61	1.16	0.30	0.24 – 0.78

¹Acknowledgement to Katherina Konrad Daga, Daniela Cimino and Maroussia Hennes for providing with the hiPSC-derived astrocytes embedded in hydrogels, murine embryonic tissue, and murine cortical tissue images, respectively.

closely together. By comparing the ratio of correct predictions to ground truth annotations (Figure 5.7), we conclude that the model adapts well to other 3D hydrogel culture images, but its performance diminishes when applied to other types of biological structures.

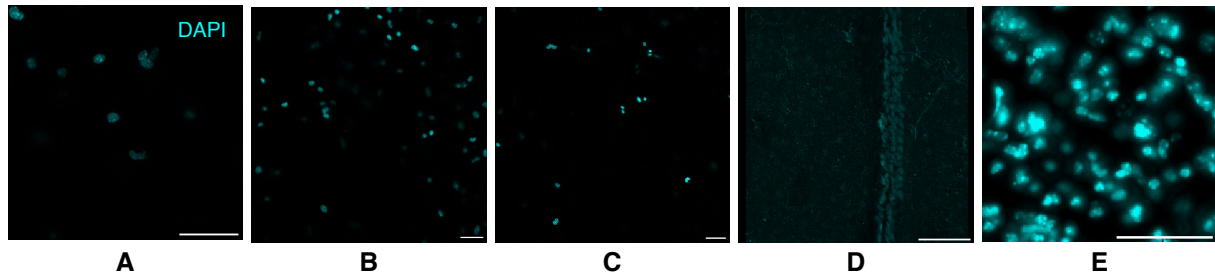


Figure 5.6: Maximum intensity projections of 12 μm in depth of exemplary images of each dataset from Table 5.6: **(A)** Training dataset, **(B)** Postnatal murine-derived astrocytes cultured in hydrogel, **(C)** hiPSC-derived astrocytes cultured in hydrogel, **(D)** Murine embryo tissue section, and **(E)** Murine cortex tissue section. Scale bars = 50 μm .

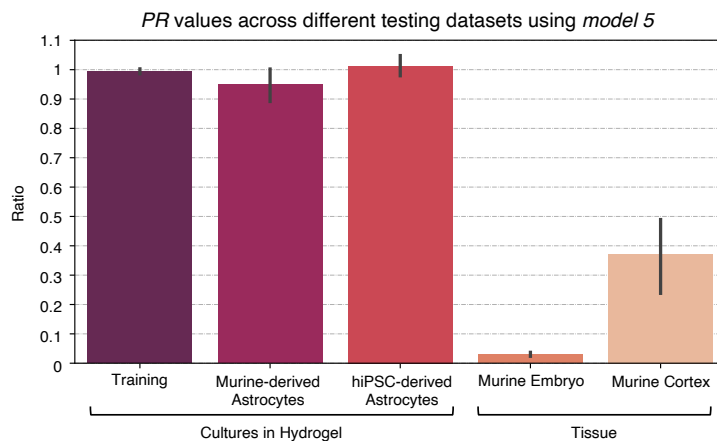


Figure 5.7: Values of the *PR* across the different testing datasets using *model 5* as predictor.

The performance of *model 4*, while promising on its initial testing set, failed to generalize to datasets with different FOVs. This limitation demonstrates the necessity of broad and diverse training datasets for effective generalization. *Model 4*'s inability to predict any instances in varied FOV datasets underscores its overfitting to specific characteristics of the original training dataset. This finding emphasizes the importance of including variations in imaging conditions, such as different FOVs and experimental setups, to enhance the robustness of trained models.

5.2 GUI for 3D Cell Culture Image Annotation

Biological image annotation often involves tasks that go beyond simply identifying cell nuclei. For instance, biologists typically need to classify each nucleus according to its morphology or marker expres-

5. COMPUTATIONAL SOLUTION FOR 3D CELL CULTURE CHARACTERIZATION

sion, where a single cell may be associated with one or more states. The approach used for classification depends on the problem at hand, as well as the conditions defined by the researcher, which can be specific or more general. For example, a set of observed morphologies may follow a characterization created by the biologist to answer a particular question (further exemplified in Section 6.1), while the presence or absence of marker expression is a more general issue that applies to many experiments due to its binary or quantitative nature.

Fiji software is widely used for biological image annotation through plugins like the Cell Counter [193] to help simplify the counting process. This tool allows biologists to set a counter for each condition they want to study and then classify each observation into its corresponding phenotype or phenotypes by navigating through 2D or 3D images. Despite its utility, this method is limited in several ways. First, data extraction from the results is rudimentary, requiring the user to copy and paste counter results into a spreadsheet application for further processing. Second, correcting or adding new data, like a new counter, is difficult, as it requires re-navigation across all instances for classification and subsequent merging in the spreadsheet. Third, the annotation process is entirely manual, often necessitating zooming in and out to observe each instance. This issue becomes even more problematic in 3D scenarios, where users must navigate through the 3D stack.

As such, current methods for image annotation are usually not user-friendly and are not suited to the high-throughput imaging technologies available in modern laboratories. The developed GUI aims to address these challenges, providing a more user-friendly experience for biologists and enabling semi-

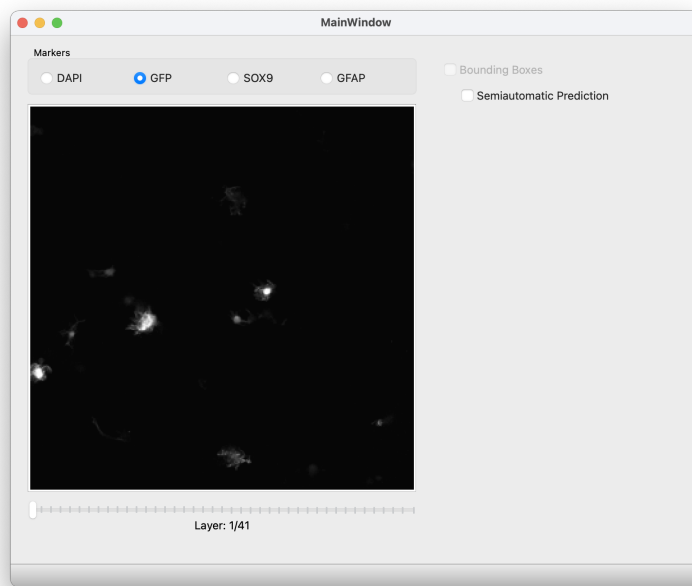


Figure 5.8: Representation of the GUI's main window with an image loaded. Image with 4 color channels: DAPI, GFP, SOX9, and GFAP, and 41 images depth.

automated annotation of large amounts of data. Nevertheless, its main objective is to facilitate the creation of image classification datasets for further application to deep learning models and automate efficiently image annotation process. The GUI was developed in Python using the PyQt5 library, this tool is currently shared on GitHub with members of the Helmholtz Munich research group, and its user guide is provided in Appendix C.

Similar to Fiji, the GUI displays four-dimensional images and allows quick navigation through the stack and channels (Figure 5.8). However, this tool is specifically designed for annotation and does not include image manipulation features. In the following subsections, the main GUI features are presented.

5.2.1 Automatic Identification of Nuclei

One of the primary features of the annotation tool is the automatic identification of nuclei. As it stands, nuclei detection still needs to be processed separately using the nuclei segmentation model described in Section 5.1.2, which requires a graphics processing unit (GPU) (NVIDIA RTX A5000, Cuda version 12.0). The preliminary step is performed on a GPU-equipped machine, and the results are then blended into a formatted .csv file, which is input into the GUI. This file includes information about the position and sizes of each bounding box in the segmented 3D nuclei structures. This feature allows blending data from all observations in the same dataset or experiment, making subsequent data analysis easier.

On the main screen of the GUI, the image and the corresponding dataset .csv file can be loaded.

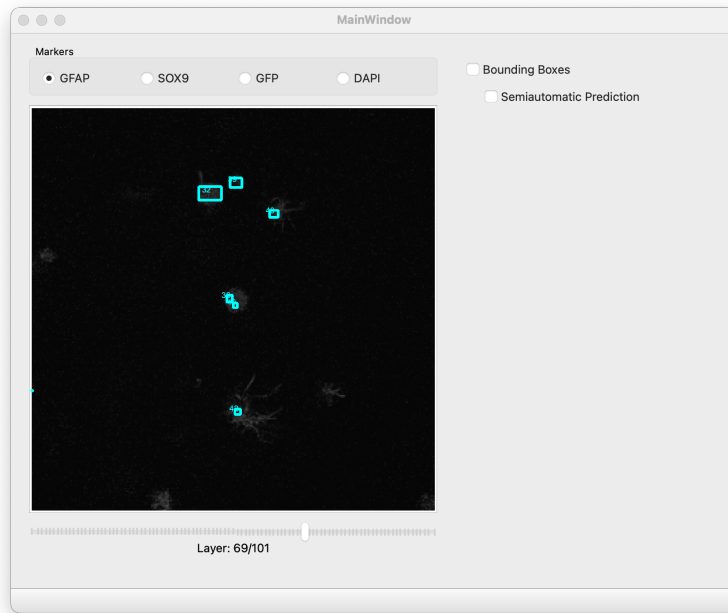


Figure 5.9: Representation of the GUI's main window with an image loaded and bounding boxes drawn. Image with 4 color channels: DAPI, GFP, SOX9, and GFAP, and 101 images depth.

5. COMPUTATIONAL SOLUTION FOR 3D CELL CULTURE CHARACTERIZATION

The image is displayed in the viewer, and the associated bounding boxes are shown around each nuclei instance identified by the nuclei segmentation model (Figure 5.9). Users can then make manual annotations of the image, identifying nuclei instances that the model may have missed.

5.2.2 Cell Labelling

The GUI was developed specifically for the present project but is designed to be easily adaptable to other use cases. For this project, the tool was tailored for two types of classification: morphological and marker expression classification. The morphological classification is specific to the project, where the images represent astrocyte cultures in 3D hydrogels, and each cell instance is classified into one of six categories: round, branched, hBranched, cluster, other, or unknown (as detailed in Subsection 4.3.4 and Figure 6.3). On the other hand, identity classification is binary and specific to cell markers, meaning it determines whether a marker is positive or negative for each dataset-specific marker.

On the right side of the main screen, users can select the options for *Bounding Boxes* and *Semiautomatic Prediction*. The semiautomatic prediction option is a feature of the bounding boxes screen. When selected, the software automatically predicts the binary marker classification of the cell instance. The semiautomatic prediction tool is not yet optimized and is not specific to individual images or channels. The chosen strategy is conservative, predicting marker presence if the mean intensity of the bounding box is 8 times higher than the mean intensity of the entire image in the same channel. While this feature

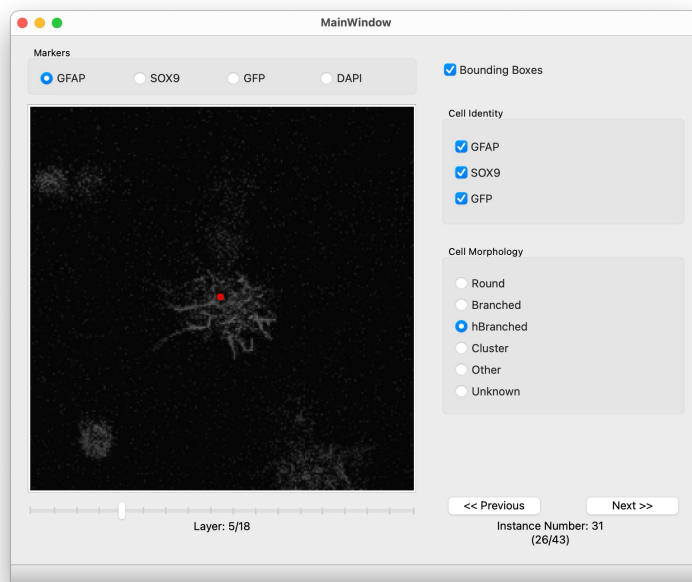


Figure 5.10: Representation of the GUI's *Bounding Boxes* window. Cell instance with 4 color channels: DAPI, GFP, SOX9, and GFAP, and 18 images depth. Instance number corresponds to the total number of instances identifies in the original image.

is still non-optimal, it allows for faster annotation with minimal corrections.

When the *Bounding Boxes* option is selected, the bounding boxes screen appears (Figure 5.10). On the left side of this screen, users can visualize each cell instance separately and navigate through its depth and color channels. On the right side, the user can annotate each instance according to its identity and morphological features. Several shortcuts have been implemented in the interface to optimize the user experience, allowing for faster annotation of large datasets (Section C.3).

Annotation of multiple images can be performed in sequence without needing to interrupt the session to save data externally. All results are saved and updated in the original .csv file, allowing the user to resume their work without loss of progress.

5.3 Deep Learning for Cell Classification

Downstream automatic tools for cell classification based on the undertaken segmentation, including the discrimination between different astrocyte morphologies, fall outside the scope of this thesis. Nevertheless, significant progress was made by creating the necessary data and formulating an approach to address this challenge. This section briefly outlines how the data generated in this project can be leveraged to efficiently train a classification model for astrocyte morphology.

The GUI developed in this project facilitates the straightforward creation of classification datasets following the annotation of original microscopy images. Specifically, the experimental images from the studies detailed in the subsequent chapter were annotated, resulting in the creation of a comprehensive dataset for training classification models. Specifically, 140 z-stack images from p5-7 murine astrocyte cell culture in MVG, VLGV, FibrinVLGV and pure fibrin hydrogels were annotated. In total there were classified 2761 cells. Regarding the morphological label n = 485 correspondend to round cells, n = 639 branched cells, n = 492 hBranched cells, n = 268 cells in clusters, n = 265 other types of cells and n = 612 unknown. Each cell instance was also classified regarding expression of GFAP, SOX9, and GFP in the actin::GFP murine cultures-derived images. This way, to the multilabel properties of the images, this dataset can be used to train classification models that predict cell morphology, cell interaction with the environment, i.e. distinguishing between single cells or cell clusters, or the cell markers expression.

The images generated for the morphology classification dataset were multi-channel 3D volumes, with individual channels corresponding to specific imaged markers: DAPI, GFAP, and SOX9, with or without GFP. During the model training phase, these channels can be utilized in different ways: individually (e.g., for predicting marker expression), collectively (e.g., using all channels to predict morphology), or through selective merging (e.g., combining specific channels to emphasize particular features of interest).

Merging color channels is particularly useful for reducing image dimensionality and enhancing the generalizability of the trained model. For example, combining all nuclei markers (such as DAPI and

SOX9) and cytoplasmic markers (such as GFAP and GFP) simplifies the training data. This approach increases generalizability, especially when testing images may contain different nuclei and cytoplasmic markers than those used during training. Figure 5.11 illustrates how a cell instance marker channels can be merged into nuclei and cytoplasmic features.

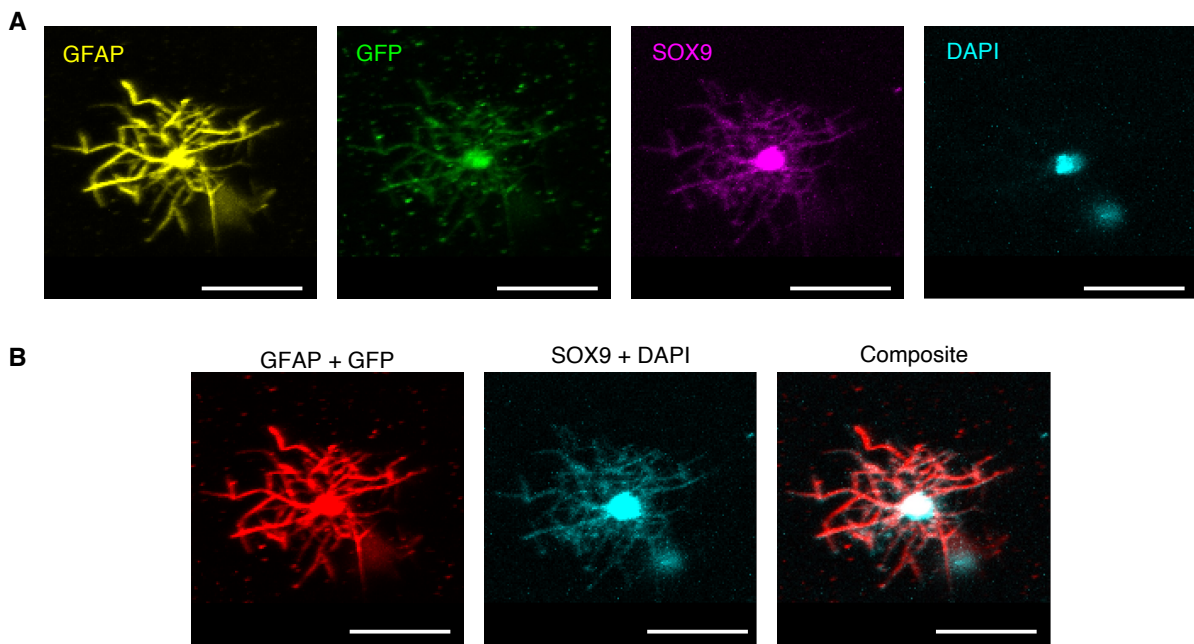


Figure 5.11: Merging of cell features for image classification. **(A)** Expression markers imaged separated in each color channel. **(B)** Cytoplasmic features (GFAP + GFP) and nuclei features (SOX9 + DAPI) selectively merged. Scale 50 μm .

Furthermore, while each image also contains information regarding the 3D structure and intensity of individual cell instances, it is suggested that, for the baseline approach, maximum intensity projections of these 3D volumes be utilized. This approach simplifies the 3D data into 2D projections while preserving key morphological features and intensity information relevant to classification tasks.

To train the classification model, deep learning architectures such as ResNet are suggested due to their proven effectiveness in handling complex image data and their ability to automatically learn hierarchical feature representations. The 2D images, derived from the multi-channel data, will serve as the input for these ResNet models. This allows the network to not only capture intricate patterns of cellular morphologies but also associate them with specific marker expressions. This dual approach — leveraging both morphological features and protein expression data — ensures that the model can accurately classify cells based on a combination of structural and functional characteristics.

This methodology promises a robust foundation for developing an automated system that can efficiently classify astrocyte morphologies, contributing to advancements in understanding cellular behaviors and the underlying biology of astrocytes.

6

Experimental Results

Contents

6.1 Cell Morphology and Astrocytic Markers Expression in Alginate and Fibrin-Alginate Hydrogels	58
6.2 Effects of CaCl ₂ Crosslinking Concentrations on Cell Viability	62
6.3 Effects of CaCl ₂ Crosslinking Concentrations on Cell Morphology and Astrocytic Markers Expression	64

6. EXPERIMENTAL RESULTS

This chapter details the experimental results obtained by culturing astrocytes derived from p5-7 mice cortical gray matter on hydrogel scaffolds. The first experiment (Section 6.1) aimed to characterize and validate the viability of three different hydrogels: MVG, VLVG and FibrinVLVG for culturing astrocytes, regarding hydrogel stability and cell morphology and astrocytic markers expression. Secondly, since the cells in alginate hydrogels were subjected to elevated concentrations of Ca^{2+} , the second experiment (Section 6.2) studies the effects of the Ca^{2+} concentration on cell viability. Thirdly, the effects of concentration of Ca^{2+} were also used to study the impact on cell morphology and astrocytic markers expression after 7 days of culture in hydrogels (Section 6.3).

The images obtained from these cultures were annotated using the tools described on Chapter 5. The nuclei segmentation model allowed for a more accurate detection and segmentation of the nuclei found on the images. Furthermore, the merging of these results with the GUI for z-stack annotation allowed for a faster and semi-automatic characterization of the cultures. The results were further individually validated.

6.1 Cell Morphology and Astrocytic Markers Expression in Alginate and Fibrin-Alginate Hydrogels

MVG, VLVG, and FibrinVLVG hydrogels were assessed in the laboratory with 7 days in vitro (DIV) cultures of astrocytes derived from the cortical GM of p5-7 Actin::GFP transgenic mice. The protocol for this experiment, illustrated in Figure 6.1, began with the creation of an expansion culture with astrocyte-selective media, enabling the natural selection of astrocytes in the culture, previously isolated from the mice. Subsequently, the astrocytes were cast in 15 μL of hydrogel volume within mini-wells (see Section B.2 of Appendix B) and maintained in culture for 7 days.

The validation of these hydrogels was conducted in two distinct phases. In the first phase, the stability and homogeneity of the technical and biological replicates were monitored over a 7 day culture period. This phase enabled qualitative comparisons among the hydrogels and the cells in culture. The second phase involved the fixation of samples with 4% PFA, followed by immunostaining for image acquisition using a Zeiss LSM 710 laser-scanning confocal microscope. These images were subsequently processed semi-automatically, allowing for quantitative comparisons between the different cultures.

In addition to the three hydrogel cultures, a monolayer control condition was included using PDL-coated coverslips. These monolayer controls served to qualitatively monitor the cultures in terms of cell confluence and survival. Furthermore, they were used to baseline cell astrocytic markers expression after the 7 day culture period. Whereas for the hydrogel conditions there was used a cell concentration of 1.000.000 cells/mL in the cell embedding, the PDL condition had an initial cell concentration of 25.000 cells/mL.

6.1 CELL MORPHOLOGY AND ASTROCYTIC MARKERS EXPRESSION IN ALGINATE AND FIBRIN-ALGINATE HYDROGELS

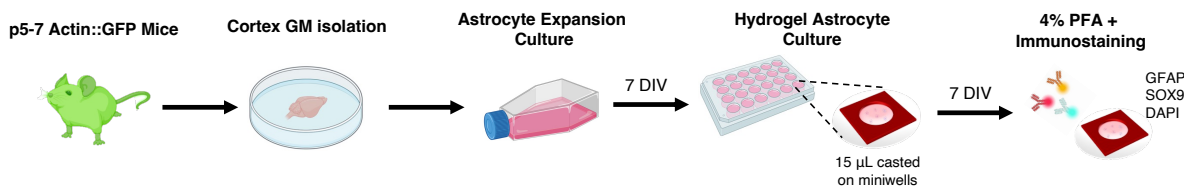


Figure 6.1: Illustrative procedure for the study of morphology and markers expression of astrocytes in alginate and alginate-fibrous hydrogels.

From the initial qualitative analysis, it was observed several differences in the hydrogels appearing from as early as the moment of casting of the hydrogels. Possibly due to the different viscosity properties of MVG, VLVG, and FibrinVLVG hydrogels, VLVG hydrogels presented much higher cell sedimentation than its counterparts (Figures 6.2A and 6.2B). Merely after 3 days of culture, the hydrogels started showing great differences on the cell morphologies (Figure 6.2C). MVG and VLVG hydrogels presented mostly round and little branched cells, with few exceptions found mainly on the VLVG hydrogels which already started showing more complex morphologies. Contrastingly, several cells on the FibrinVLVG hydrogels already presented complex morphologies and significant branching.

Throughout the experimental period, MVG and VLVG hydrogels exhibited low stability, with the cultures showing significant differences between technical and biological replicates. Moreover, the hydrogels often displayed heterogeneity even within the same miniwell, which is far from optimal as it introduces variable conditions within a single technical replicate. After the 7 days in culture, the significant cell sedimentation following the casting phase on VLVG hydrogels, decreased the concentration of cells in the tridimensional state (Figure 6.2D-VLVG). Conversely, while the higher density of MVG hydrogels reduced cell sedimentation, it inhibited cell branching (Figure 6.2D-MVG). Consequently, most cells in these hydrogels appeared rounded or exhibited only small branches. Furthermore, both MVG and VLVG hydrogels demonstrated low stability during fixation with PFA, leading to hydrogel degradation. This instability rendered quantitative analysis impossible for all MVG samples and most VLVG samples.

Contrastingly, the FibrinVLVG hydrogels presented higher stability compared to VLVG hydrogels not degrading as easily, and rendered cells with more interesting morphologies that mimic the astrocytes found in the murine brain more closely (Figure 6.2D-FibrinVLVG), with distinct branches expanding from the cell body.

For the morphology and markers expression analysis over the different hydrogel conditions, the cells embedded within the hydrogels were stained for GFAP and SOX9 markers and imaged using confocal microscopy. However, due to significant hydrogel degradation, the experimental dataset was substantially limited. Specifically, all three biological replicates of the MVG hydrogel condition degraded, as did two out of three replicates of the VLVG hydrogel condition. Consequently, quantitative analysis for the MVG condition was infeasible, and the VLVG condition lacked sufficient replicates to enable statistically

6. EXPERIMENTAL RESULTS

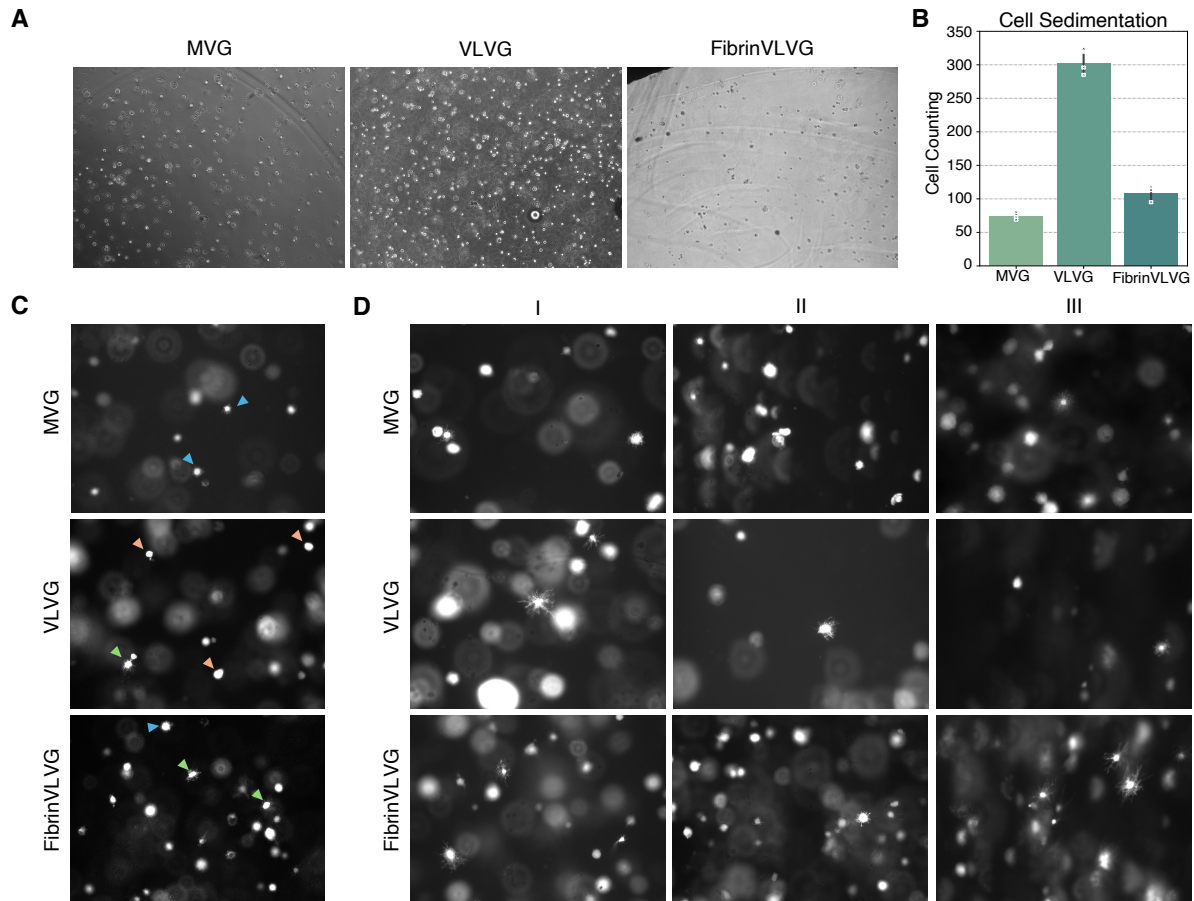


Figure 6.2: Qualitative analysis of MVG, VLVG and FibrinVLVG hydrogels. **(A)** Bright field microscopy images, 10X magnification, of the first layer of cells sedimented on the glass coverslip after the moment of casting (0 hours). Bright-field microscope 10X. **(B)** Barplot of the sedimented number of cells after casting per hydrogel condition ($N = 3$), obtained through the counting of the number of cells in focus on images obtained in the same conditions of (a). **(C)** 3 DIV fluorescent images illustrating morphological differences of the cells found on each hydrogel condition: orange – round cells, blue – branched cells, and green – highly branched cells. Bright-field microscope 20X. **(D)** 7 DIV fluorescent images comparing 3 biological replicates of each hydrogel condition. Bright-field microscope 20X. The roman numbering (I, II, III) distinguishes three biological replicates without correlation between hydrogel conditions.

robust conclusions. Despite these constraints, comparative analyses of the remaining samples were performed to investigate differences in cellular morphology and astrocytic markers expression. As depicted on Figure 6.3A, the cells' morphology was categorized into six classes between round, branched, hBranched, cluster, other and unknown (see Subsection 4.3.4 for more details). Furthermore, comparisons were made to monolayer PDL cultures, which served as a reference for assessing astrocytic markers expression.

The proportion of cell clusters within the hydrogel cultures was evaluated. The mean percentage of cell clusters observed in FibrinVLVG hydrogels was 5.58%, notably lower than the 21.59% observed in VLVG hydrogels (Figure 6.3B). Despite this apparent trend, the high variability within the data precluded

6.1 CELL MORPHOLOGY AND ASTROCYTIC MARKERS EXPRESSION IN ALGINATE AND FIBRIN-ALGINATE HYDROGELS

statistical significance ($p = 0.288$, independent t -test).

The morphological characteristics of individual cells were also analyzed, specifically focusing on the degree of branching. In VLVG hydrogels, 46.89% of cells exhibited a round morphology, compared to 31.15% in FibrinVLVG hydrogels (Figure 6.3C). While this suggests a potential difference in cell behavior between conditions, the results did not achieve statistical significance ($p = 0.72$, independent t -test).

Within the FibrinVLVG samples, a detailed analysis of branched and hBranched was conducted (Figure 6.3C). The proportions of these morphological subtypes were found to be statistically indistinguishable ($p = 0.90$, paired t -test). However, when the total percentage of branched structures was compared to the percentage of round cells, no statistically significant difference was identified ($p = 0.44$, paired t -test). The variability observed in these analyses was largely attributed to an outlier biological replicate (N6), which introduced significant variance into the dataset.

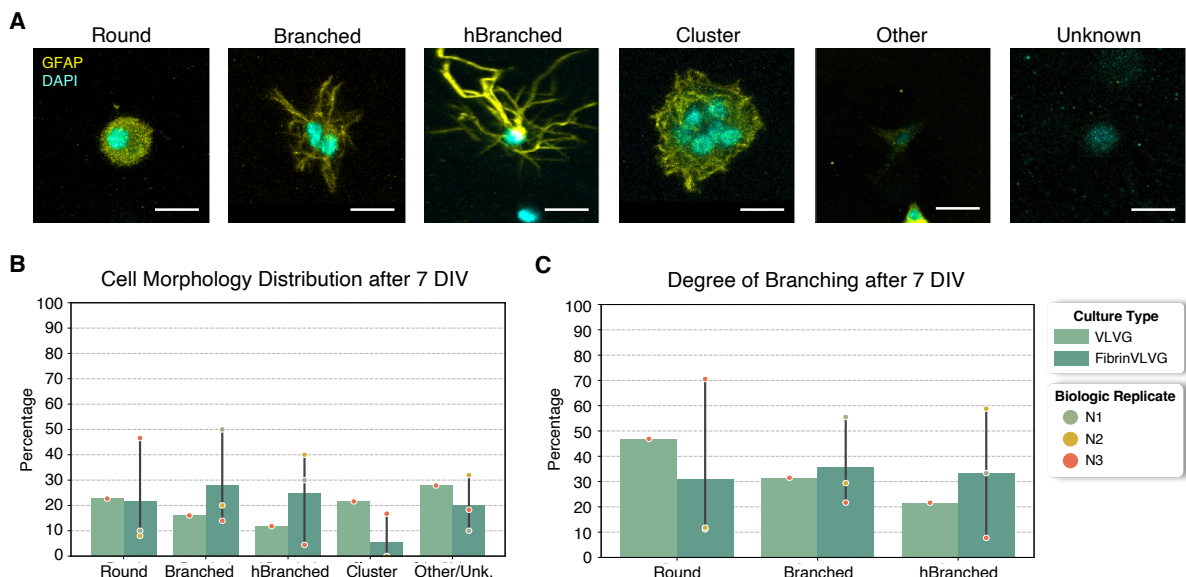


Figure 6.3: Morphological cell analysis of MVG, VLVG and FibrinVLVG hydrogels. **(A)** Depiction of cell morphologies found in the hydrogels in the 3D state. Scale bar = 15 μm . **(B)** Cell morphology distribution in VLVG ($N = 1$) and FibrinVLVG hydrogels after 7 DIV ($N = 3$). **(C)** Degree of branching distribution states in VLVG and FibrinVLVG hydrogels after 7 DIV.

The proportion of astrocytes within the hydrogel cultures, identified by the presence of the SOX9 marker in cell nuclei, was notably high, with percentages exceeding 70% across all conditions and surpassing 90% in the VLVG hydrogel samples (Figure 6.4). In contrast, the mean percentage of GFAP⁺ cells was markedly lower, averaging less than 13.15%. This discrepancy highlights the difference between the total astrocyte population and the subset of astrocytes expressing GFAP.

The ratio of reactive astrocytes, defined as the proportion of GFAP⁺ cells relative to SOX9⁺ cells, was higher in the hydrogel cultures compared to the PDL monolayer control. This observation suggests an elevated level of astrocytic reactivity in the 3D hydrogel environment. However, the difference in the

6. EXPERIMENTAL RESULTS

mean values was not statistically significant ($p = 0.15$, independent t -test), which may be attributed to the high variability among samples and the limited number of biological replicates.

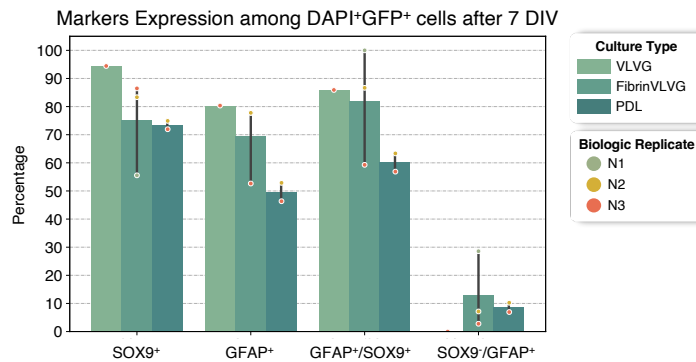


Figure 6.4: Distribution of cell population regarding GFAP and SOX9 markers expression, in VLVG ($N = 1$) and FibrinVLVG hydrogels ($N = 3$), and PDL cultures ($N = 2$) after 7 DIV.

6.2 Effects of CaCl₂ Crosslinking Concentrations on Cell Viability

A 24-hour experiment was conducted to evaluate the effects of different CaCl₂ concentrations on cell viability (Figure 6.5). The study quantified cell death following cell seeding onto Fibrin and FibrinVLVG hydrogels gelated with varying calcium ion concentrations: 5 mM, 50 mM, 100 mM and 175 mM. The cortical gray matter cells were isolated from p5-7 mice and cultured in astrocyte-selective media for 7 days to achieve confluence. The cells were then casted in 50 μ L hydrogel droplets at a density of 1.000.000 cells/mL directly onto glass-bottom well plates. After 24 hours, the cell viability assay was performed using Hoechst 33342, calcein, and PI viability markers (see Subsection 4.3.2). Automated live-cell imaging was conducted using a STELLARIS 8 FALCON on DMi8 (Leica Microsystems) confocal microscope. A monolayer control was included, with cells seeded on PDL-coated coverslips at a density of 25.000 cells/mL. There were performed 5 biological replicates.

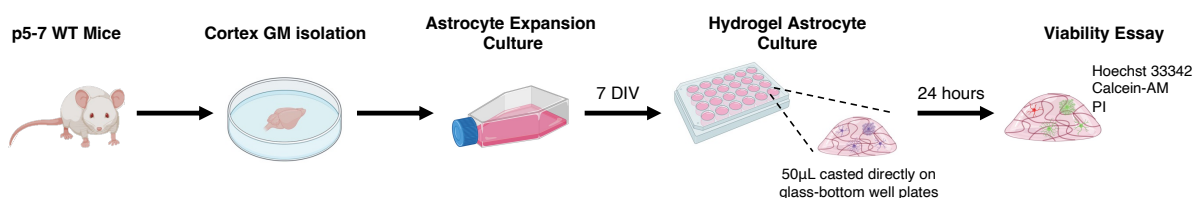


Figure 6.5: Illustrative procedure for the study of cell viability in VLVG and FibrinVLVG hydrogels crosslinked with different concentrations of CaCl₂.

The Hoechst 33342 labeled all nuclei, providing a control for total cell count, while calcein and PI labeled live and dead cells, respectively (Figure 6.6). Some cells were observed to express both viability

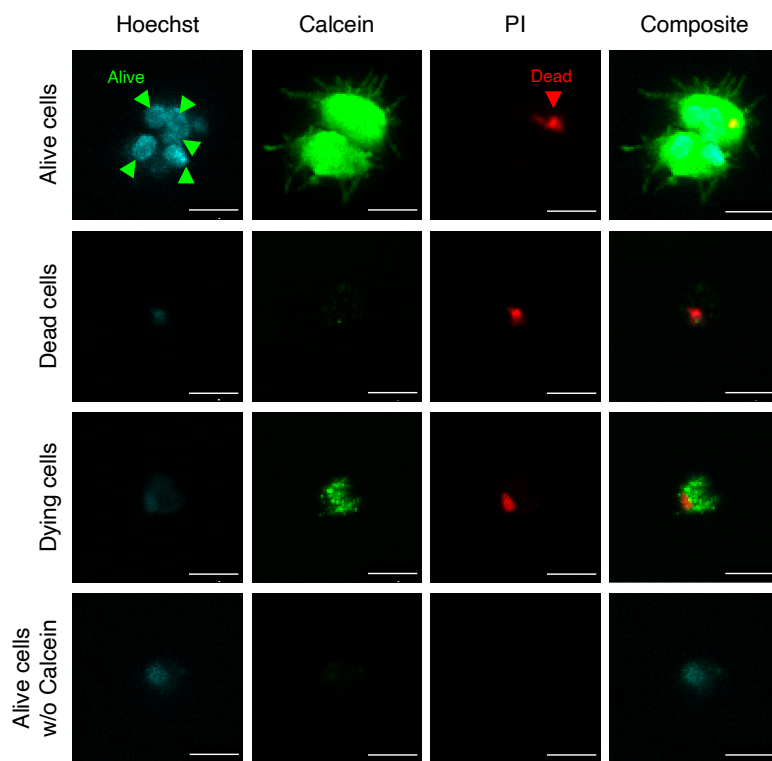


Figure 6.6: Astrocytic markers expression characterization and classification based on viability markers. Hoescht 33342 in blue, calcein in green and PI in red. Scale bar = 20 μ m.

markers (Calcein⁺PI⁺), likely representing cells undergoing late-stage death. These cells are thought to have been viable at the start of the assay, produced calcien during the 45-minute incubation but later died, allowing PI to penetrate the nuclei. Their incomplete and diffuse calcien staining suggests membrane compromise. Additionally, some Hoechst-stained cells lacked both calcien and PI signals. These cells are hypothesized to be viable cells with unknown mechanisms preventing calcien uptake. Dual-stained cells were evenly distributed throughout the hydrogel depth, ruling out diffusion limitations of the staining reagents.

Cell viability was categorized as follows: PI⁻ cells were classified as live, Calcein⁺PI⁺ cells as dying, and Calcein⁻PI⁺ cells as dead. The results (Figure 6.7) showed no cell death or stress-related events in the PDL monolayer control, highlighting its suitability as an optimal culture condition regarding cell viability. In contrast, hydrogel cultures displayed increased cell stress, reflected in increased proportions of dead and dying cells. Fibrin hydrogels (0 mM Ca²⁺) exhibited 87.64% live cells, while FibrinVLG conditions averaged 81.43% \pm 2.12%. Statistical analysis revealed no significant difference in cell survival between the Fibrin and FibrinVLG conditions ($p = 0.176$, independent *t*-test). However, hydrogel culture conditions resulted in significantly higher cell death rates compared to monolayer conditions ($p = 1.4 \times 10^{-4}$, independent *t*-test), emphasizing the stress-inducing effects of the 3D matrix.

6. EXPERIMENTAL RESULTS

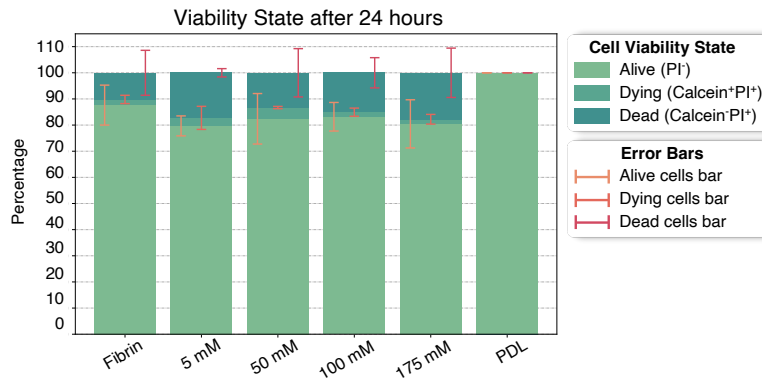


Figure 6.7: Viability essay analysis on VLVG and FibrinVLVG hydrogels crosslinked with 5 mM, 50 mM, 100 mM, and 175 mM of Ca^{2+} , comparing to monolayer cell cultures of PDL coated coverslips. The error bars indicate the standard deviation for each viability state, centered on the corresponding mean.

environment.

The correlation between CaCl_2 concentration and cell viability was also assessed. Pearson, denoted with r , and Spearman, denoted with ρ , correlation tests revealed no significant correlation between CaCl_2 levels and the proportions of live or dead cells. For Pearson correlation, $r = 0.03$ ($p = 0.93$) for live cells and $r = 0.09$ ($p = 0.78$) for dead cells. Spearman correlation yielded $\rho = 0.15$ ($p = 0.64$) for live cells and $\rho = -0.065$ ($p = 0.84$) for dead cells. These results indicate that CaCl_2 concentration does not significantly influence cell viability in the tested conditions.

6.3 Effects of CaCl_2 Crosslinking Concentrations on Cell Morphology and Astrocytic Markers Expression

To investigate whether different Ca^{2+} concentrations impact hydrogel properties during gelation and subsequently influence cell morphology and astrocytic markers expression over prolonged culture periods, a new experiment was designed. This study aimed to evaluate the effects of Ca^{2+} concentrations on astrocytic morphology and reactivity. The experimental procedure mirrored that of the preceding studies (Figure 6.8). Cortical glial cells were isolated from p5-7 WT mice, cultured in astrocyte-selective media for seven days, and subsequently embedded in hydrogels. These hydrogels were cast directly onto glass-bottom well plates as 50 μL droplets containing 1.000.000 cells/mL. Additionally, a monolayer control was prepared by seeding cells at a density of 25.000 cells/mL onto PDL-coated coverslips.

After seven days of culture, cells were fixed with 4% PFA and immunostained for GFAP and SOX9 markers. Notably, Fibrin and 5 mM FibrinVLVG hydrogels demonstrated poor stability over the culture period. Partial degradation was observed within 1–2 days for 5 mM FibrinVLVG hydrogels and 6–7 days for Fibrin hydrogels. Nevertheless, sufficient data was collected to obtain five biological replicates for

6.3 EFFECTS OF CaCl₂ CROSSLINKING CONCENTRATIONS ON CELL MORPHOLOGY AND ASTROCYTIC MARKERS EXPRESSION

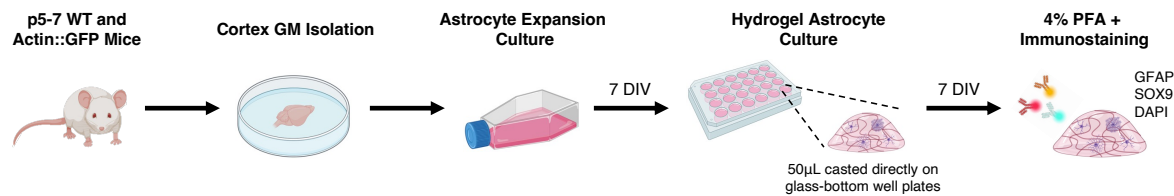


Figure 6.8: Illustrative procedure for the study of cell morphology and astrocytic markers expression in Fibrin and FibrinVLVG hydrogels crosslinked with different concentrations of CaCl₂.

each condition.

The instability of these hydrogels was reflected in the high percentage of cells exhibiting irregular morphologies, which could not be classified into standard astrocytic branching patterns (Figure 6.9A). This proportion reached 51.95% for Fibrin hydrogels and 45.98% for 5 mM FibrinVLVG hydrogels, in contrast to an average of $22.23\% \pm 4.99\%$ for the other conditions. Of these unclassified cells, 10.26% $\pm 3.91\%$ were not astrocytes (i.e., they did not express SOX9).

An assessment of Ca²⁺ concentration on astrocytic branching (Figure 6.9B) revealed a positive correlation between increased Ca²⁺ concentrations and greater degrees of branching ($r = 0.32$, $p = 0.12$). This trend suggests that higher Ca²⁺ levels, potentially leading to increased hydrogel stiffness, promote astrocytic ramification. Among all tested conditions, the 100 mM FibrinVLVG hydrogel exhibited the highest branching rate, with 84.24% of cells displaying a branched morphology, whereas the 5 mM FibrinVLVG condition exhibited the lowest at 69.45%. Notably, in all conditions, the majority of cells retained a branched morphology.

Variability in Fibrin and 5 mM FibrinVLVG hydrogels extended to cell astrocytic markers expression analysis (Figure 6.10), precluding significant conclusions for these conditions. Conversely, the remaining hydrogel and monolayer control conditions consistently demonstrated high proportions of astrocytes in culture. All hydrogel conditions yielded astrocyte proportions exceeding 70%, with median values consistently above 90%. In comparison, the monolayer control exhibited slightly lower median astrocyte proportions, exceeding 80%. Statistical analysis revealed that hydrogel conditions significantly promoted astrocyte selection over monolayer controls ($p = 0.04$, independent *t*-test).

The Ca²⁺ ion concentrations used during hydrogel gelation also inversely influenced GFAP expression. There was a significant negative correlation between Ca²⁺ concentration and both the proportion of GFAP⁺ cells ($r = -0.60$, $p = 0.019$) and the GFAP^{+/SOX9⁺ ratio ($r = -0.59$, $p = 0.020$). This finding suggests reduced astrocytic reactivity in hydrogels gelated with higher Ca²⁺ concentrations. Furthermore, monolayer cultures exhibited significantly lower astrocytic reactivity than stable hydrogel conditions ($p = 0.015$, independent *t*-test). These results collectively underscore the influence of Ca²⁺ concentrations on astrocytic morphology and reactivity within hydrogel environments.}

Finally, the correlation between the expression of SOX9 and GFAP markers and the morphological

6. EXPERIMENTAL RESULTS

classification of the cells was calculated (see Figure 6.11). Cells classified as *Other* or *Unknown* exhibited a strong negative correlation with the expression of both SOX9 and GFAP markers, with statistical significance. This result was anticipated, as cells in these groups could not be classified due to the absence of the cytoplasm marker (GFAP) or were not astrocytes (i.e., they did not express SOX9).

On the other hand, the remaining conditions generally showed a positive correlation with the expression of both SOX9 and GFAP. The clusters observed in the FibrinVLVG 175 mM condition were the only class that presented a negative correlation with SOX9⁺, indicating a trend where the clusters

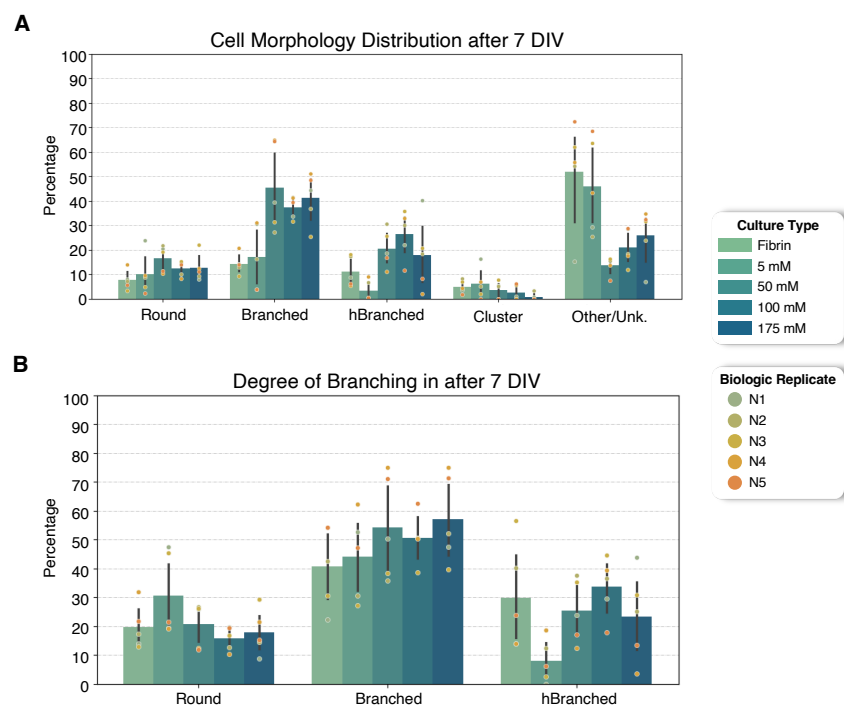


Figure 6.9: Cell morphology analysis in Fibrin and FibrinVLVG hydrogels (N = 5). **(A)** Cell morphology distribution. **(B)** Degree of branching distribution.

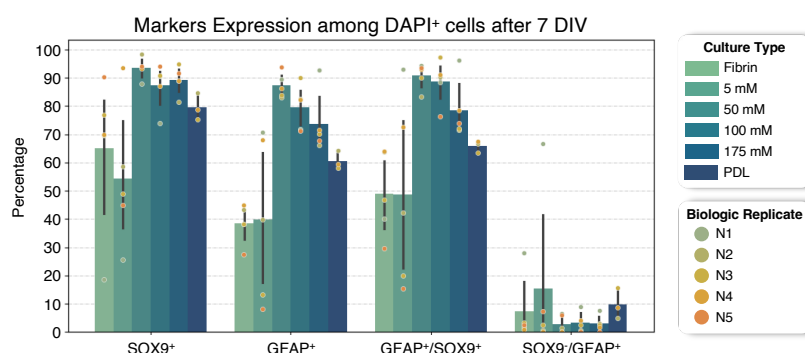


Figure 6.10: Astrocytic markers expression analysis on Fibrin and FibrinVLVG hydrogels crosslinked with 5 mM, 50 mM, 100 mM, and 175 mM of Ca²⁺, comparing to monolayer cell cultures of PDL coated coverslips.

6.3 EFFECTS OF CACL₂ CROSSLINKING CONCENTRATIONS ON CELL MORPHOLOGY AND ASTROCYTIC MARKERS EXPRESSION

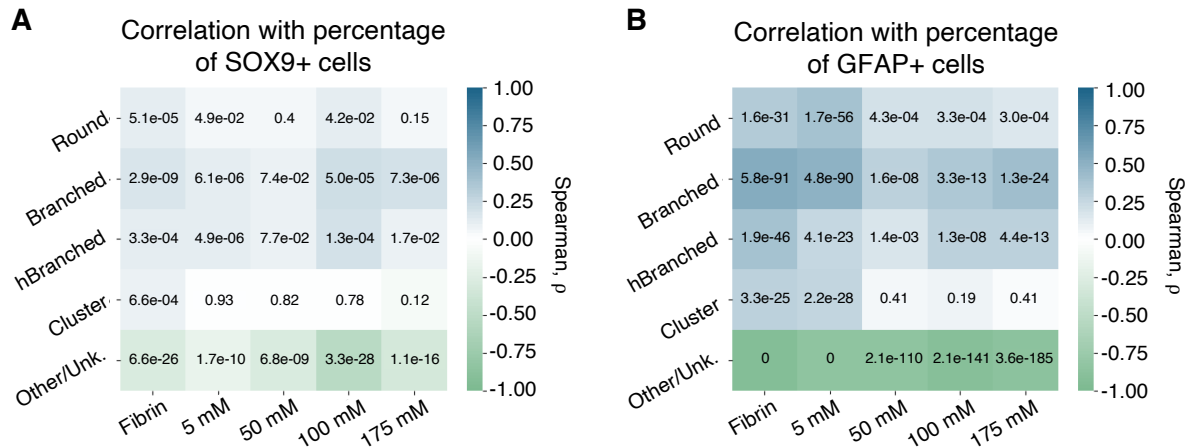


Figure 6.11: Correlation between morphology and astrocytic markers expression analysis on Fibrin and FibrinVLG hydrogels crosslinked with 5 mM, 50 mM, 100 mM, and 175 mM of Ca²⁺. The heatmap scale indicates the spearman correlation values. The numerical values within the heatmap represent the p-values for the respective statistical comparisons. Note that, p-values lower than 0.05 convey statistical significant correlations.

in FibrinVLG 175 mM hydrogels were predominantly composed of non-astrocytic cells. However this observation does not have a statistical significant p-value.

Round, branched and hBranched morphologies exhibited similar moderate correlations with the percentage of SOX9⁺ cells ($\rho = 0.12 \pm 0.049$). This observation suggests that the distribution of astrocytes across these morphological classes is approximately the same. In contrast, the percentage of GFAP⁺ cells among the same round and branched classes displayed a slight preference for branched and hBranched morphologies to express GFAP ($\rho = 0.35 \pm 0.11$). The correlation between the percentage of GFAP⁺ cells and the round morphology was somewhat weaker ($\rho = 0.25 \pm 0.095$). Notably, the correlation between the percentage of GFAP⁺ cells and the round, branched, and hBranched morphologies reached statistical significance across all measures, while the correlation between the percentage of SOX9⁺ cells and these morphologies was statistically significant in 73% of the observations, providing strong support for the findings (Figure 6.11).

7

Discussion

Contents

7.1 Discussion of the Computational Solutions	70
7.2 Discussion of the Experimental Results	74

7. DISCUSSION

This chapter discusses the results and achievements derived from the computational solutions outlined in Chapter 5, as well as the experimental work presented in Chapter 6. Furthermore, the challenges and limitations encountered during the experimental phase are addressed, as well as the inherent constraints of the undertaken work.

7.1 Discussion of the Computational Solutions

Nuclei Segmentation Tool

Overall, the mean IoU and mAP results of the 2D nuclei segmentation model fine-tuned on Mask R-CNN (*ftk3*) align well with those reported in previous studies [172, 174]. Despite using a more conservative IoU threshold, $\tau = 0.2$, in this analysis compared to other studies, the achieved results affirm the credibility and effectiveness of the selected model. It is anticipated that further refinement through additional training iterations will enhance these segmentation outcomes. This suggests that exceptional segmentation results can be achieved even when working within the constraints of a limited dataset in the 2D scenario.

The presented baseline solution for the nuclei segmentation task simplifies the network optimization problem by fixing some hyperparameters, such as batch size, learning rate, and the number of epochs. The advantages of a fine hyperparameterization is well-documented in the literature [194]. However, at the light of existing computational constraints and the solid efficacy levels achieved by some of the tested hyperparameterizations, a stable hyperparameterization – batch size of 2, a learning rate of 0.002, and setting the number of epochs to 20 – was fixed, achieving a *PR* value of 0.88. While optimizing these values could potentially enhance the network's performance, such improvement is not guaranteed.

The data augmentation strategies employed did not yield the expected performance improvements, obtaining a lower *PR* value of 0.85. To enhance performance, a more tailored approach to augmentation techniques could be explored, optimizing their application to maximize efficacy. For example, increasing the rate of data transformations in the training set or diversifying the transformation techniques could lead to different conclusions and potentially improve the network's performance.

Regarding the validation of Cellpose 2D, several concerning aspects of its functionality were noted. In addition to the suboptimal outcomes achieved, several predefined conditions within the algorithm impact its performance. Notably, the model type selection significantly influences results. Despite using the *cytoplasm* model instead of the *nucleus* model – due to the intrinsic characteristics of our dataset – the results were less competitive than those obtained with other architectures. Furthermore, this model exhibited significantly longer estimation times, taking up to 60 times longer than alternative models to generate predictions, regardless of the number of resulting predictions. Its primary advantage lay in simultaneously computing the nuclei area and predicting the nuclei position. However, these statistics

can also be retrieved with relative ease from the leading models. Nevertheless, it is acknowledged that fine-tuning the Cellpose 2D model can lead to significant performance improvements, as demonstrated in this project with the Mask R-CNN model.

Conversely, Stardist 2D, even without fine-tuning, exhibited highly competitive results, comparable to the best-performing model based on the Mask R-CNN architecture. It is hypothesized that fine-tuning Stardist 2D on our dataset could further improve the accuracy of the results. However, this task was out of the scope of the project.

The improved solution proposed in this study for nuclei segmentation of 3D instances, which involved training the nnU-Net model from scratch, demonstrated excellent performance on the training dataset ($PR = 99.5\%$) and when tested on datasets resembling the culture conditions of the training data ($PR > 95\%$). In particular, *model 5* achieved high accuracy in segmenting nuclei in the DAPI channel across different biological samples from murine and hiPSCs cultures in hydrogels. In contrast, the performance of Stardist 3D and Cellstitch algorithms was notably less effective in accurately predicting cell instances in our training dataset. While Stardist 3D tended to underpredict the number of instances ($PR \approx 0.65$), Cellstitch tended to largely overestimate this value ($PR \approx 3.1$). Nevertheless, it is worth noting that the performance of Stardist 3D and Cellstitch could potentially have been improved if they had been fine-tuned to our specific dataset, as they were originally pretrained on datasets that may not fully capture the nuances of our experimental conditions.

When the best-performing nnU-Net model (*model 5*) was tested on datasets derived from cortical and embryonic tissues of murine origin, its performance substantially decreased. This reduction in accuracy was expected, given the limited scope and diversity of the training dataset. These results highlight a critical limitation in the generalizability of models trained on small and specific datasets. To develop a more robust and generalizable model, it is crucial to expand the training dataset. This expansion could involve not only data augmentation strategies but also incorporating a broader range of data from different biological contexts. Such measures would enable the model to better generalize across various tissue types and experimental conditions, making it more adaptable to real-world scenarios.

Moreover, the efficiency and generalizability of the model could not be fully validated in terms of its correlation with key image parameters such as FOV, resolution, and anisotropy. The lack of diverse image acquisition conditions limited the ability to assess how these factors affect model performance. Future work should include datasets with varied imaging conditions to better understand how image parameters influence the performance of deep learning models in biological image segmentation tasks. Furthermore, incorporating a larger variety of image resolutions, FOV sizes, and anisotropy ratios could help improve the model's robustness and its ability to process images from different sources.

Additionally, it would be valuable to explore alternative model architectures or hybrid approaches, possibly combining the strengths of different models, such as nnU-Net with other instance segmen-

7. DISCUSSION

tion algorithms, including Stardist 3D, to achieve even better segmentation performance. Future studies could also experiment with multi-channel data to enhance the model’s ability to distinguish between distinct cellular features, such as nuclei and cytoplasm, especially when working with complex biological structures like tissues with tightly packed cells. As proposed in Section 5.3, merging cell features separately, such as nuclei and cytoplasmic features, might be useful also for enhancing nuclei segmentation tools while preserving the models’ versatility.

Finally, the integration of manual annotation with semi-automated tools, such as napari, has proven useful in creating accurate ground truth data for training purposes. However, as the dataset increases in size and complexity, further advancements in automated annotation methods, possibly leveraging active learning techniques, could help reduce the time and effort required for dataset preparation while maintaining the quality of annotations.

The efficiency of the 3D segmentation model is remarkable in segmenting nuclei from astrocyte cultures in hydrogels. Nuclei segmentation using a GPU (NVIDIA RTX A5000, CUDA version 12.0) was up to $4\times$ faster than manual nuclei identification (i.e., manually pinpointing the nuclei location) and $120\times$ faster than the equivalent manual nuclei segmentation task¹. Furthermore, the nuclei segmentation results achieved remarkable prediction ratio values, with 95% correct predictions for the murine cultures and around 100% for the hiPSC cultures.

GUI for 3D Cell Culture Image Annotation

The development of the GUI for biological image annotation addresses several critical challenges currently faced by biologists in experimental analysis settings. Annotating biological images, particularly in complex scenarios like 3D cell cultures, has long been a bottleneck in many experiments due to the limitations of existing annotation tools. These limitations include the time-consuming nature of manual annotation, difficulties in extracting and correcting data, and the lack of flexibility to adapt to specific research needs. The GUI developed in this project alleviates these challenges by providing a semi-automated, user-friendly solution that allows biologists to efficiently annotate large volumes of data without compromising accuracy.

One of the key strengths of this tool is its ability to handle various types of data. It is designed to enable the efficient annotation of z-stack images with multi-channel imaging data. Additionally, the integration of an automatic nuclei detection feature facilitates rapid identification of cell nuclei, moving closer to automated classification. Although this feature is not yet fully optimized and currently performs competitively only on astrocyte cell cultures in hydrogel scaffolds, it represents significant progress in automating the initial stages of annotation.

¹The time measurement for each task was not detailed in project. On average, for hydrogel volumes of $8\times 10^3 \mu\text{m}^3$ with a cell concentration of 1 million cells/mL, 3D manual segmentations took between 150 to 180 minutes/image, manual nuclei identification on the same images about 4 to 6 minutes/image, and automatic nuclei segmentation about 90 seconds/image.

The nuclei segmentation step currently requires an external GPU-based segmentation process, limiting its accessibility and making it less ideal for all users. Developing a more integrated solution that performs all tasks within the same tool would enhance user-friendliness. Furthermore, implementing a nuclei detection algorithm, instead of nuclei segmentation, could improve computational efficiency by disregarding measurements of nuclei-specific features, such as size and shape, which may be less critical for the intended characterizations on marker expression and cell morphology.

The tool's semi-automated annotation feature is particularly valuable in reducing the workload involved in annotation. It uses pre-segmented nuclei data to automatically predict the binary classification of marker expression based on intensity measurements. While the current strategy of predicting marker presence based solely on intensity is overly simplistic and may not be effective in all cases, enhancing the prediction algorithm with machine learning techniques or more sophisticated image analysis methods could improve its accuracy and adaptability across diverse datasets. Nonetheless, this feature provides a solid foundation for data annotation and can be manually corrected with minimal effort. This approach accelerates the annotation process while preserving manual validation for final decision-making.

Another notable benefit of the tool is its flexibility for accommodating different types of annotations. It supports both morphological classifications and marker expression-based classifications, making it adaptable for a variety of biological experiments. By enabling these types of annotations in parallel, the tool ensures that different aspects of cellular behavior and marker expression are captured in a streamlined and comprehensive manner. This functionality offers biologists a more holistic overview of global cell culture characteristics. While this feature is not yet fully enabled, this project has laid the groundwork for tailoring the interface to address a specific problem. Future improvements could include enabling user-specific annotation classes and features to further customize the tool for diverse research needs.

In addition, the tool was designed with ease of use in mind. By allowing for manual adjustments, biologists can correct prediction errors that may occur in the automated system. Given the complexity of biological images, especially when working with 3D datasets, a tool that facilitates easy corrections is invaluable. This combination of automation and user input also enhances the tool's versatility.

Furthermore, it incorporates intuitive shortcut controls for navigating 3D stacks, which is particularly important when working with volumetric images. The inclusion of a bounding box feature simplifies the visualization of segmented nuclei and allows users to quickly classify cells based on their morphology or markers expression. The tool's integration with external files ensures that data can be seamlessly updated and saved, supporting a smooth and continuous annotation process without the need for frequent manual saving. The ability to annotate multiple images sequentially without interruption further enhances workflow efficiency. Data is continuously saved and updated in the original annotation file,

7. DISCUSSION

enabling users to resume their work without losing progress.

Nevertheless, the tool could benefit from improved integration with downstream analysis platforms. While it can export data in a .csv format, adding support for more advanced data visualization and statistical analysis tools would greatly benefit biologists who need to perform complex analyses on their annotated datasets. This could include built-in support for analysis in Python, R or MatLab.

Overall, the GUI developed in this project represents a significant advancement in biological image annotation, addressing many of the limitations of existing tools. By automating parts of the annotation process while allowing for easy manual corrections, it achieves a balance between efficiency and accuracy. Its ability to handle 4D data and support the classification of both morphological and markers expression features makes it a versatile tool suitable for a wide range of biological experiments. With further optimizations and refinements, this tool has the potential to greatly improve the annotation process in high-throughput biological studies, ultimately accelerating the pace of research and discovery.

7.2 Discussion of the Experimental Results

The comparative evaluation of hydrogels revealed significant differences in their ability to support astrocyte cultures in a 3D environment. The findings underscore the importance of hydrogel composition in influencing cell viability, morphology, and astrocytic marker expression patterns.

Hydrogel Stability and Cell Morphology

Hydrogel stability emerged as a critical determinant of experimental outcomes. MVG and VLGV hydrogels demonstrated poor stability, degrading during the fixation procedure and leading to substantial variability among replicates. This instability hindered quantitative analysis of MVG hydrogels and reduced the reliability of VLGV results. Fibrin and FibrinVLGV hydrogels, while exhibiting greater stability, also showed partial degradation, particularly at a 5 mM Ca²⁺ crosslinking concentration. This degradation was associated with an increased proportion of cells with irregular morphologies, which could not be classified into standard astrocytic patterns.

Astrocyte morphology was also influenced by hydrogel composition and Ca²⁺ concentration. Increased Ca²⁺ levels positively correlated with higher degrees of astrocytic branching ($r = 0.32$, $p = 0.12$), suggesting that greater hydrogel stiffness promotes ramification. The highest branching rates were observed in FibrinVLGV hydrogels gelated with 100mM Ca²⁺, whereas lower concentrations resulted in the lowest branching rates. These findings highlight the importance of tuning hydrogel casting conditions to support astrocyte cultures and mimic *in vivo*-like morphologies.

Cell Viability and Stress

Cell viability assays revealed stress-related effects in hydrogel cultures compared to monolayer controls. The proportion of live cells was lower in hydrogel environments, with fibrin and FibrinVLG hydrogels averaging 87.64% and 81.43% live cells, respectively, compared to the monolayer condition, which exhibited no observable cell death. This disparity emphasizes the stress-inducing effects of 3D hydrogel environments, likely due to increased mechanical resistance, altered nutrient diffusion, or casting-related stress.

Ca^{2+} concentration did not significantly influence cell viability under the tested conditions, as indicated by weak Pearson and Spearman correlations between Ca^{2+} levels and the proportions of live or dead cells after a 24-hour experimental period. However, different results might be observed after longer culture periods. A viability assay over 7 days in hydrogels should be performed to effectively assess how Ca^{2+} affects cell viability in the long term.

Astrocytic Markers Expression and Reactivity

Immunostaining for SOX9 and GFAP markers provided insights into astrocytic markers expression and reactivity. Across all hydrogel conditions, high proportions of astrocytes were observed, with mean SOX9⁺ proportions consistently exceeding 70%. Notably, monolayer controls exhibited slightly lower astrocyte proportions, indicating that hydrogel environments may better support astrocyte selection.

The ratio of GFAP⁺ astrocytes was influenced by Ca^{2+} concentrations. Higher Ca^{2+} levels during gelation were associated with reduced astrocytic reactive marker expression, as evidenced by negative correlations with both the proportion of GFAP⁺ cells ($r = -0.60$, $p = 0.02$) and the GFAP⁺/SOX9⁺ ratio ($r = -0.59$, $p = 0.02$). These findings suggest that increased hydrogel stiffness may suppress astrocytic reactivity, potentially mimicking the quiescent state of astrocytes in healthy brain tissue [195]. However, additional experiments must be conducted in order to assess the effective hydrogel physical properties and the expression of other astrocytic reactivity markers through bulk RNA-Seq.

Correlation Between Morphology and Marker Expression

The correlation analysis between SOX9 and GFAP marker expression and morphological classifications further elucidated the relationship between astrocytic markers expression and cell morphology. Cells classified as *Other* or *Unknown* exhibited a strong negative correlation with SOX9 and GFAP expression, consistent with their classification as non-astrocytic or unidentifiable cells. Conversely, round and branched morphologies showed moderate positive correlations with SOX9 expression, indicating an even distribution of astrocytes across these classes. A slight preference for GFAP expression in branched and hBranched morphologies was observed, suggesting a potential link between branching

7. DISCUSSION

complexity and astrocytic reactivity.

Interestingly, the clusters observed in FibrinVLVG hydrogels gelated with 175 mM Ca²⁺ displayed a negative correlation with SOX9 expression, suggesting a prevalence of non-astrocytic cells in these clusters. However, this observation was not statistically significant, highlighting the need for further studies to validate these trends.

These findings collectively emphasize the role of hydrogel properties, including composition and gelation conditions, in shaping astrocyte behavior in 3D cultures. FibrinVLVG hydrogels, particularly those gelated with higher Ca²⁺ concentrations, emerged as the most promising candidate for astrocyte culture, owing to their stability ability to support complex morphologies. However, the limited number of biological replicates, underscores the need for further optimization and validation.

Future work should prioritize optimizing hydrogel formulations to strike a balance between stability, stiffness, and biological compatibility. Addressing these factors will improve the reproducibility and reliability of 3D astrocyte cultures. Increasing the sample size and adjust experimental protocols will help mitigate variability and enhance the robustness of statistical analyses.

Furthermore, the thorough characterization of the physical properties of hydrogels is urgently needed, particularly given the observed variability in stability and morphological outcomes across different Ca²⁺ crosslinking concentrations. Understanding parameters such as stiffness, porosity, and degradation rates will provide critical insights into the structure-function relationships of these biomaterials. This is especially important as protocols are refined and Ca²⁺ concentrations are varied during gelation.

Lastly, exploring the molecular mechanisms underlying hydrogel-mediated effects on astrocyte morphology and reactivity could offer a deeper understanding of how the 3D microenvironment influences cellular behavior. Such studies could unlock the full potential of hydrogel systems for applications in neural tissue engineering, regenerative medicine, and disease modeling, where astrocyte behavior is a key determinant of success.

8

Conclusion

Contents

8.1 Conclusions	78
8.2 Limitations and Future Work	79

8. CONCLUSION

8.1 Conclusions

This project achieved meaningful contributions to the field of automated characterization of 3D astrocyte cultures in hydrogel matrices, leveraging a dual approach that integrates experimental and computational advancements. By addressing key challenges in both domains, this work provides a solid foundation for the optimization of 3D cell culture systems and their analysis, with implications for neurobiology and regenerative medicine.

In particular, advances were proposed along in three main fronts. Firstly, from the **experimental validation of hydrogel systems** stand point, the study provides a comprehensive evaluation of astrocyte morphology, viability, and marker expression in various hydrogel systems, identifying optimal conditions for future applications. Multiple hydrogel platforms, including MVG and VLVG alginate, fibrin, and their composite, FibrinVLVG, for astrocyte culturing were explored and validated. The results demonstrated that FibrinVLVG hydrogels, particularly those crosslinked with calcium chloride at 100 mM concentration, provided the most supportive microenvironment for murine astrocytes. These conditions promoted favorable cell viability, while also preserving key morphological features and the expression of astrocytic markers such as GFAP and SOX9. Comparative analysis revealed that 3D culture systems promote astrocyte reactive profiles when compared to monolayer systems, highlighting their potential for studying astrocyte behavior and heterogeneity under physiologically relevant conditions. However, cell death is also superior on these systems appealing further refinement of the methods.

Secondly, from the **computational solutions** perspective, this work takes an initial step towards the development of a high-throughput analysis pipeline for the characterization of astrocyte cultures, with special emphasis on nuclei segmentation and cell classification in 3D images. Using deep learning methods, the study compared the performance of different models, with nnU-Net emerging as a robust solution for accurate nuclei segmentation across multiple z-stack fluorescent microscopy images datasets. Furthermore, the integration of this tool into a user-friendly GUI streamlined the annotation and analysis process, enabling researchers to efficiently label cell features and extract classification datasets. This automated approach reduces the time and expertise required for manual image analysis, paving the way for broader adoption in biological research.

Finally, considering the **synergy between biology and computer science**, this project takes a significant step towards bridging the gap between biological modeling and data-driven analysis, fostering more robust investigations into astrocyte biology. Automating image analysis has become indispensable in modern laboratories, as it not only accelerates workflows but also enhances the standardization and scalability of data processing. Consequently, the automation of these processes adds substantial value to research endeavors, enabling the generation and analysis of large, high-quality datasets with improved consistency and reliability.

8.2 Limitations and Future Work

While the findings are promising, several limitations – both experimental and computational – warrant careful consideration, as the project focused on a specific case study of culturing postnatal mouse-derived astrocytes in alginate- and fibrin-based hydrogels. Ensuring the scalability of the experiments and the insights gained here will be crucial for future advancements and broader applications.

A deeper understanding of the effects of fibrin-alginate hydrogels on astrocyte cultures is needed, as these interactions remain insufficiently explored. Phenotypic studies of the cultures produced, as well as the creation of cultures using astrocytes derived from different sources, would provide valuable insights into the proposed models' effectiveness in supporting cell function and their scalability to varied conditions. Furthermore, a comprehensive assessment of the physical and chemical properties of the hydrogels remains lacking. Variations in calcium chloride crosslinking concentrations or the choice of hydrogel scaffolds used in this study are expected to significantly influence their physicochemical properties. However, the absence of detailed measurements compromises the ability to draw a holistic analysis.

From a computational perspective, training tailored deep learning models continues to pose significant challenges, particularly due to the scarcity of annotated data, which remains a critical bottleneck. Addressing this issue by exploring techniques for partially automating data annotation is vital. Such advancements could enhance the generalizability of the nuclei segmentation model and streamline cell instance classification. Additionally, the implementation of a nuclei detection model, rather than a segmentation model, could be considered. This approach would reduce computational demands during prediction and simplify the annotation process, albeit at the cost of losing detailed nuclei information. Further, the GUI developed still remains tailored for very specific needs only. Extending these efforts for more generalizable applications will leverage the project outreach near the scientific community.

Bibliography

- [1] B. A. Reynolds and S. Weiss, "Generation of neurons and astrocytes from isolated cells of the adult mammalian central nervous system," *science*, vol. 255, no. 5052, pp. 1707–1710, 1992.
- [2] P. S. Eriksson, E. Perfilieva, T. Björk-Eriksson, A.-M. Alborn, C. Nordborg, D. A. Peterson, and F. H. Gage, "Neurogenesis in the adult human hippocampus," *Nature medicine*, vol. 4, no. 11, pp. 1313–1317, 1998.
- [3] M. B. Luskin, "Restricted proliferation and migration of postnatally generated neurons derived from the forebrain subventricular zone," *Neuron*, vol. 11, no. 1, pp. 173–189, 1993.
- [4] C. Lois and A. Alvarez-Buylla, "Proliferating subventricular zone cells in the adult mammalian forebrain can differentiate into neurons and glia." *Proceedings of the National Academy of Sciences*, vol. 90, no. 5, pp. 2074–2077, 1993.
- [5] H. G. Kuhn, H. Dickinson-Anson, and F. H. Gage, "Neurogenesis in the dentate gyrus of the adult rat: age-related decrease of neuronal progenitor proliferation," *Journal of Neuroscience*, vol. 16, no. 6, pp. 2027–2033, 1996.
- [6] H. Cameron, C. Woolley, B. McEwen, and E. Gould, "Differentiation of newly born neurons and glia in the dentate gyrus of the adult rat," *Neuroscience*, vol. 56, no. 2, pp. 337–344, 1993.
- [7] A. Kumar, V. Pareek, M. A. Faiq, S. K. Ghosh, and C. Kumari, "Adult neurogenesis in humans: a review of basic concepts, history, current research, and clinical implications," *Innovations in clinical neuroscience*, vol. 16, no. 5-6, p. 30, 2019.
- [8] E. R. Kandel, J. H. Schwartz, T. M. Jessell, S. Siegelbaum, A. J. Hudspeth, S. Mack *et al.*, *Principles of neural science*. McGraw-hill New York, 2000, vol. 4.
- [9] H. Hirbec, N. Déglon, L. C. Foo, I. Goshen, J. Grutzendler, E. Hangen, T. Kreisel, N. Linck, J. Mufat, S. Regio *et al.*, "Emerging technologies to study glial cells," *Glia*, vol. 68, no. 9, pp. 1692–1728, 2020.

BIBLIOGRAPHY

- [10] M. M. Rahman, M. R. Islam, M. Yamin, M. M. Islam, M. T. Sarker, A. F. K. Meem, A. Akter, T. B. Emran, S. Cavalu, and R. Sharma, “Emerging role of neuron-glia in neurological disorders: at a glance,” *Oxidative medicine and cellular longevity*, vol. 2022, no. 1, p. 3201644, 2022.
- [11] T. Araki, Y. Ikegaya, and R. Koyama, “The effects of microglia-and astrocyte-derived factors on neurogenesis in health and disease,” *European Journal of Neuroscience*, vol. 54, no. 5, pp. 5880–5901, 2021.
- [12] S. J. Miller, “Astrocyte heterogeneity in the adult central nervous system,” *Frontiers in cellular neuroscience*, vol. 12, p. 401, 2018.
- [13] Z. Jiwaji and G. E. Hardingham, “Good, bad, and neglectful: Astrocyte changes in neurodegenerative disease,” *Free Radical Biology and Medicine*, vol. 182, pp. 93–99, 2022.
- [14] C. Muñoz-Ballester and S. Robel, “Astrocyte-mediated mechanisms contribute to traumatic brain injury pathology,” *WIREs Mechanisms of Disease*, vol. 15, no. 5, p. e1622, 2023.
- [15] R. L. Davis, H. Weintraub, and A. B. Lassar, “Expression of a single transfected cdna converts fibroblasts to myoblasts,” *Cell*, vol. 51, no. 6, pp. 987–1000, 1987.
- [16] N. Heins, P. Malatesta, F. Cecconi, M. Nakafuku, K. L. Tucker, M. A. Hack, P. Chapouton, Y.-A. Barde, and M. Götz, “Glial cells generate neurons: the role of the transcription factor pax6,” *Nature neuroscience*, vol. 5, no. 4, pp. 308–315, 2002.
- [17] Z. Guo, L. Zhang, Z. Wu, Y. Chen, F. Wang, and G. Chen, “In vivo direct reprogramming of reactive glial cells into functional neurons after brain injury and in an alzheimer’s disease model,” *Cell stem cell*, vol. 14, no. 2, pp. 188–202, 2014.
- [18] R. Bocchi, G. Masserdotti, and M. Götz, “Direct neuronal reprogramming: Fast forward from new concepts toward therapeutic approaches,” *Neuron*, vol. 110, no. 3, pp. 366–393, 2022.
- [19] T. Mori, A. Buffo, and M. Götz, “The novel roles of glial cells revisited: the contribution of radial glia and astrocytes to neurogenesis,” *Current topics in developmental biology*, vol. 69, pp. 67–99, 2005.
- [20] J. C. Fontoura, C. Viezzer, F. G. Dos Santos, R. A. Ligabue, R. Weinlich, R. D. Puga, D. Antonow, P. Severino, and C. Bonorino, “Comparison of 2d and 3d cell culture models for cell growth, gene expression and drug resistance,” *Materials Science and Engineering: C*, vol. 107, p. 110264, 2020.
- [21] C. Jensen and Y. Teng, “Is it time to start transitioning from 2d to 3d cell culture?” *Frontiers in molecular biosciences*, vol. 7, p. 33, 2020.

- [22] M. P. Lutolf and J. Hubbell, "Synthetic biomaterials as instructive extracellular microenvironments for morphogenesis in tissue engineering," *Nature biotechnology*, vol. 23, no. 1, pp. 47–55, 2005.
- [23] M. W. Tibbitt and K. S. Anseth, "Hydrogels as extracellular matrix mimics for 3d cell culture," *Biotechnology and bioengineering*, vol. 103, no. 4, pp. 655–663, 2009.
- [24] T.-C. Ho, C.-C. Chang, H.-P. Chan, T.-W. Chung, C.-W. Shu, K.-P. Chuang, T.-H. Duh, M.-H. Yang, and Y.-C. Tyan, "Hydrogels: properties and applications in biomedicine," *Molecules*, vol. 27, no. 9, p. 2902, 2022.
- [25] H. Geckil, F. Xu, X. Zhang, S. Moon, and U. Demirci, "Engineering hydrogels as extracellular matrix mimics," *Nanomedicine*, vol. 5, no. 3, pp. 469–484, 2010.
- [26] U. S. Madduma-Bandarage and S. V. Madihally, "Synthetic hydrogels: Synthesis, novel trends, and applications," *Journal of Applied Polymer Science*, vol. 138, no. 19, p. 50376, 2021.
- [27] E. Mauri, A. Sacchetti, N. Vicario, L. Peruzzotti-Jametti, F. Rossi, and S. Pluchino, "Evaluation of rgd functionalization in hybrid hydrogels as 3d neural stem cell culture systems," *Biomaterials science*, vol. 6, no. 3, pp. 501–510, 2018.
- [28] J. George, C.-C. Hsu, L. T. B. Nguyen, H. Ye, and Z. Cui, "Neural tissue engineering with structured hydrogels in cns models and therapies," *Biotechnology advances*, vol. 42, p. 107370, 2020.
- [29] Y. Huang, A. Kruger, S. Syed, C. B. Kayasandik, M. Papadakis, and D. Labate, "Automated detection of gfap-labeled astrocytes in micrographs using yolov5," *Scientific Reports*, vol. 12, no. 1, p. 22263, 2022.
- [30] P. M. Kulkarni, E. Barton, M. Savelonas, R. Padmanabhan, Y. Lu, K. Trett, W. Shain, J. L. Leasure, and B. Roysam, "Quantitative 3-d analysis of gfap labeled astrocytes from fluorescence confocal images," *Journal of neuroscience methods*, vol. 246, pp. 38–51, 2015.
- [31] J. Schindelin, I. Arganda-Carreras, E. Frise, V. Kaynig, M. Longair, T. Pietzsch, S. Preibisch, C. Rueden, S. Saalfeld, B. Schmid *et al.*, "Fiji: an open-source platform for biological-image analysis," *Nature methods*, vol. 9, no. 7, pp. 676–682, 2012.
- [32] M. K. Gautier and S. D. Ginsberg, "A method for quantification of vesicular compartments within cells using 3d reconstructed confocal z-stacks: comparison of imagej and imaris to count early endosomes within basal forebrain cholinergic neurons," *Journal of neuroscience methods*, vol. 350, p. 109038, 2021.
- [33] H. Hyden, "The neuron and its glia-a biochemical and functional unit." *Endeavour*, vol. 21, pp. 144–155, 1962.

BIBLIOGRAPHY

- [34] F. A. Azevedo, L. R. Carvalho, L. T. Grinberg, J. M. Farfel, R. E. Ferretti, R. E. Leite, W. J. Filho, R. Lent, and S. Herculano-Houzel, “Equal numbers of neuronal and nonneuronal cells make the human brain an isometrically scaled-up primate brain,” *Journal of Comparative Neurology*, vol. 513, no. 5, pp. 532–541, 2009.
- [35] T. Fellin, “Communication between neurons and astrocytes: relevance to the modulation of synaptic and network activity,” *Journal of neurochemistry*, vol. 108, no. 3, pp. 533–544, 2009.
- [36] R. Cabezas, M. Ávila, J. Gonzalez, R. S. El-Bachá, E. Báez, L. M. García-Segura, J. C. Jurado Coronel, F. Capani, G. P. Cardona-Gomez, and G. E. Barreto, “Astrocytic modulation of blood brain barrier: perspectives on parkinson’s disease,” *Frontiers in cellular neuroscience*, vol. 8, p. 211, 2014.
- [37] G. Schiera, C. M. Di Liegro, G. Schirò, G. Sorbello, and I. Di Liegro, “Involvement of astrocytes in the formation, maintenance, and function of the blood–brain barrier,” *Cells*, vol. 13, no. 2, p. 150, 2024.
- [38] P. Preman, M. Alfonso-Triguero, E. Alberdi, A. Verkhratsky, and A. M. Arranz, “Astrocytes in alzheimer’s disease: pathological significance and molecular pathways,” *Cells*, vol. 10, no. 3, p. 540, 2021.
- [39] E.-H. Joe, D.-J. Choi, J. An, J.-H. Eun, I. Jou, and S. Park, “Astrocytes, microglia, and parkinson’s disease,” *Experimental neurobiology*, vol. 27, no. 2, p. 77, 2018.
- [40] P. M. Rappold and K. Tieu, “Astrocytes and therapeutics for parkinson’s disease,” *Neurotherapeutics*, vol. 7, no. 4, pp. 413–423, 2010.
- [41] A. Becerra-Calixto and G. P. Cardona-Gómez, “The role of astrocytes in neuroprotection after brain stroke: potential in cell therapy,” *Frontiers in molecular neuroscience*, vol. 10, p. 88, 2017.
- [42] O. Le Thuc, T. Gruber, M. H. Tschöp, and C. García-Cáceres, “Control of systemic metabolism by astrocytes in the brain,” *Glial-Neuronal Signaling in Neuroendocrine Systems*, pp. 127–153, 2021.
- [43] E. F. Garland, I. J. Hartnell, and D. Boche, “Microglia and astrocyte function and communication: what do we know in humans?” *Frontiers in neuroscience*, vol. 16, p. 824888, 2022.
- [44] R. C. Koehler, R. J. Roman, and D. R. Harder, “Astrocytes and the regulation of cerebral blood flow,” *Trends in neurosciences*, vol. 32, no. 3, pp. 160–169, 2009.
- [45] W. A. Banks, “The blood–brain barrier as an endocrine tissue,” *Nature Reviews Endocrinology*, vol. 15, no. 8, pp. 444–455, 2019.

- [46] S. Tietz and B. Engelhardt, "Brain barriers: crosstalk between complex tight junctions and adherens junctions," *Journal of Cell Biology*, vol. 209, no. 4, pp. 493–506, 2015.
- [47] A. M. Brown and B. R. Ransom, "Astrocyte glycogen and brain energy metabolism," *Glia*, vol. 55, no. 12, pp. 1263–1271, 2007.
- [48] A. Panov, Z. Orynbayeva, V. Vavilin, and V. Lyakhovich, "Fatty acids in energy metabolism of the central nervous system," *BioMed research international*, vol. 2014, no. 1, p. 472459, 2014.
- [49] W.-S. Chung, N. J. Allen, and C. Eroglu, "Astrocytes control synapse formation, function, and elimination," *Cold Spring Harbor perspectives in biology*, vol. 7, no. 9, p. a020370, 2015.
- [50] N. A. Oberheim, T. Takano, X. Han, W. He, J. H. Lin, F. Wang, Q. Xu, J. D. Wyatt, W. Pilcher, J. G. Ojemann *et al.*, "Uniquely hominid features of adult human astrocytes," *Journal of Neuroscience*, vol. 29, no. 10, pp. 3276–3287, 2009.
- [51] C. Falcone and V. Martínez-Cerdeño, "Astrocyte evolution and human specificity," *Neural Regeneration Research*, vol. 18, no. 1, pp. 131–132, 2023.
- [52] C. Escartin, E. Galea, A. Lakatos, J. P. O'Callaghan, G. C. Petzold, A. Serrano-Pozo, C. Steinhäuser, A. Volterra, G. Carmignoto, A. Agarwal *et al.*, "Reactive astrocyte nomenclature, definitions, and future directions," *Nature neuroscience*, vol. 24, no. 3, pp. 312–325, 2021.
- [53] M. K. Gottipati, J. M. Zuidema, and R. J. Gilbert, "Biomaterial strategies for creating in vitro astrocyte cultures resembling in vivo astrocyte morphologies and phenotypes," *Current opinion in biomedical engineering*, vol. 14, pp. 67–74, 2020.
- [54] S. A. Liddelow and B. A. Barres, "Reactive astrocytes: production, function, and therapeutic potential," *Immunity*, vol. 46, no. 6, pp. 957–967, 2017.
- [55] A. M. Jurga, M. Paleczna, J. Kadluczka, and K. Z. Kuter, "Beyond the gfap-astrocyte protein markers in the brain," *Biomolecules*, vol. 11, no. 9, p. 1361, 2021.
- [56] W. Sun, A. Cornwell, J. Li, S. Peng, M. J. Osorio, N. Aalling, S. Wang, A. Benraiss, N. Lou, S. A. Goldman *et al.*, "Sox9 is an astrocyte-specific nuclear marker in the adult brain outside the neurogenic regions," *Journal of Neuroscience*, vol. 37, no. 17, pp. 4493–4507, 2017.
- [57] J. D. Cahoy, B. Emery, A. Kaushal, L. C. Foo, J. L. Zamanian, K. S. Christopherson, Y. Xing, J. L. Lubischer, P. A. Krieg, S. A. Krupenko *et al.*, "A transcriptome database for astrocytes, neurons, and oligodendrocytes: a new resource for understanding brain development and function," *Journal of Neuroscience*, vol. 28, no. 1, pp. 264–278, 2008.

BIBLIOGRAPHY

- [58] M. Rothermundt, M. Peters, J. H. Prehn, and V. Arolt, “S100b in brain damage and neurodegeneration,” *Microscopy research and technique*, vol. 60, no. 6, pp. 614–632, 2003.
- [59] F. Michetti, N. D’Ambrosi, A. Toesca, M. A. Puglisi, A. Serrano, E. Marchese, V. Corvino, and M. C. Geloso, “The s100b story: from biomarker to active factor in neural injury,” *Journal of neurochemistry*, vol. 148, no. 2, pp. 168–187, 2019.
- [60] J. Steiner, H.-G. Bernstein, H. Bielau, A. Berndt, R. Brisch, C. Mawrin, G. Keilhoff, and B. Bogerts, “Evidence for a wide extra-astrocytic distribution of s100b in human brain,” *BMC neuroscience*, vol. 8, pp. 1–10, 2007.
- [61] E. Hedlund and T. Perlmann, “Neuronal cell replacement in parkinson’s disease,” *Journal of internal medicine*, vol. 266, no. 4, pp. 358–371, 2009.
- [62] M. Götz and R. Bocchi, “Neuronal replacement: Concepts, achievements, and call for caution,” *Current opinion in neurobiology*, vol. 69, pp. 185–192, 2021.
- [63] S. Grade and M. Götz, “Neuronal replacement therapy: previous achievements and challenges ahead,” *NPJ Regenerative medicine*, vol. 2, no. 1, p. 29, 2017.
- [64] C. Heinrich, R. Blum, S. Gascón, G. Masserdotti, P. Tripathi, R. Sánchez, S. Tiedt, T. Schroeder, M. Götz, and B. Berninger, “Directing astroglia from the cerebral cortex into subtype specific functional neurons,” *PLoS biology*, vol. 8, no. 5, p. e1000373, 2010.
- [65] A. Buffo, M. R. Vosko, D. Ertürk, G. F. Hamann, M. Jucker, D. Rowitch, and M. Götz, “Expression pattern of the transcription factor olig2 in response to brain injuries: implications for neuronal repair,” *Proceedings of the National Academy of Sciences*, vol. 102, no. 50, pp. 18 183–18 188, 2005.
- [66] S. Gascón, E. Murenu, G. Masserdotti, F. Ortega, G. L. Russo, D. Petrik, A. Deshpande, C. Heinrich, M. Karow, S. P. Robertson *et al.*, “Identification and successful negotiation of a metabolic checkpoint in direct neuronal reprogramming,” *Cell stem cell*, vol. 18, no. 3, pp. 396–409, 2016.
- [67] W. Niu, T. Zang, Y. Zou, S. Fang, D. K. Smith, R. Bachoo, and C.-L. Zhang, “In vivo reprogramming of astrocytes to neuroblasts in the adult brain,” *Nature cell biology*, vol. 15, no. 10, pp. 1164–1175, 2013.
- [68] O. Torper, D. R. Ottosson, M. Pereira, S. Lau, T. Cardoso, S. Grealish, and M. Parmar, “In vivo reprogramming of striatal ng2 glia into functional neurons that integrate into local host circuitry,” *Cell reports*, vol. 12, no. 3, pp. 474–481, 2015.

- [69] R. H. Baloh, J. D. Glass, and C. N. Svendsen, “Stem cell transplantation for amyotrophic lateral sclerosis,” *Current opinion in neurology*, vol. 31, no. 5, pp. 655–661, 2018.
- [70] J. H. Man, L. Groenink, and M. Caiazzo, “Cell reprogramming approaches in gene-and cell-based therapies for parkinson’s disease,” *Journal of controlled release*, vol. 286, pp. 114–124, 2018.
- [71] S. Liu, T. Schackel, N. Weidner, and R. Puttagunta, “Biomaterial-supported cell transplantation treatments for spinal cord injury: challenges and perspectives,” *Frontiers in cellular neuroscience*, vol. 11, p. 430, 2018.
- [72] S. Gascón, G. Masserdotti, G. L. Russo, and M. Götz, “Direct neuronal reprogramming: achievements, hurdles, and new roads to success,” *Cell stem cell*, vol. 21, no. 1, pp. 18–34, 2017.
- [73] J. S. Schweitzer, B. Song, T. M. Herrington, T.-Y. Park, N. Lee, S. Ko, J. Jeon, Y. Cha, K. Kim, Q. Li *et al.*, “Personalized ipsc-derived dopamine progenitor cells for parkinson’s disease,” *New England Journal of Medicine*, vol. 382, no. 20, pp. 1926–1932, 2020.
- [74] R. Bocchi and M. Götz, “Neuronal reprogramming for brain repair: challenges and perspectives,” *Trends in Molecular Medicine*, vol. 26, no. 10, pp. 890–892, 2020.
- [75] Y. Imamura, T. Mukohara, Y. Shimono, Y. Funakoshi, N. Chayahara, M. Toyoda, N. Kiyota, S. Takao, S. Kono, T. Nakatsura *et al.*, “Comparison of 2d-and 3d-culture models as drug-testing platforms in breast cancer,” *Oncology reports*, vol. 33, no. 4, pp. 1837–1843, 2015.
- [76] K. M. Yamada and M. Sixt, “Mechanisms of 3d cell migration,” *Nature Reviews molecular cell biology*, vol. 20, no. 12, pp. 738–752, 2019.
- [77] L. S. Costard, R. R. Hosn, H. Ramanayake, F. J. O’Brien, and C. M. Curtin, “Influences of the 3d microenvironment on cancer cell behaviour and treatment responsiveness: A recent update on lung, breast and prostate cancer models,” *Acta Biomaterialia*, vol. 132, pp. 360–378, 2021.
- [78] X. Wu, J. Su, J. Wei, N. Jiang, and X. Ge, “Recent advances in three-dimensional stem cell culture systems and applications,” *Stem cells international*, vol. 2021, no. 1, p. 9477332, 2021.
- [79] S. P. Pasca, “The rise of three-dimensional human brain cultures,” *Nature*, vol. 553, no. 7689, pp. 437–445, 2018.
- [80] R. Samanipour, H. Tahmooressi, H. Rezaei Nejad, M. Hirano, S.-R. Shin, and M. Hoorfar, “A review on 3d printing functional brain model,” *Biomicrofluidics*, vol. 16, no. 1, 2022.
- [81] M. E. Sakalem, M. T. De Sibio, F. A. d. S. da Costa, and M. de Oliveira, “Historical evolution of spheroids and organoids, and possibilities of use in life sciences and medicine,” *Biotechnology Journal*, vol. 16, no. 5, p. 2000463, 2021.

BIBLIOGRAPHY

- [82] L. Song, X. Yuan, Z. Jones, C. Vied, Y. Miao, M. Marzano, T. Hua, Q.-X. A. Sang, J. Guan, T. Ma *et al.*, “Functionalization of brain region-specific spheroids with isogenic microglia-like cells,” *Scientific reports*, vol. 9, no. 1, p. 11055, 2019.
- [83] D. Pamies, P. Barrera, K. Block, G. Makri, A. Kumar, D. Wiersma, L. Smirnova, C. Zhang, J. Bressler, K. M. Christian *et al.*, “A human brain microphysiological system derived from induced pluripotent stem cells to study neurological diseases and toxicity,” *Altex*, vol. 34, no. 3, p. 362, 2016.
- [84] K. M. De Kleijn, W. A. Zuure, K. R. Straasheijm, M. B. Martens, M. C. Avramut, R. I. Koning, and G. J. Martens, “Human cortical spheroids with a high diversity of innately developing brain cell types,” *Stem Cell Research & Therapy*, vol. 14, no. 1, p. 50, 2023.
- [85] S.-Y. Lee, I.-S. Koo, H. J. Hwang, and D. W. Lee, “In vitro three-dimensional (3d) cell culture tools for spheroid and organoid models,” *SLAS discovery*, vol. 28, no. 4, pp. 119–137, 2023.
- [86] C. Giorgi, G. Lombardozzi, F. Ammannito, M. S. Scenna, E. Maceroni, M. Quintiliani, M. d’Angelo, A. Cimini, and V. Castelli, “Brain organoids: a game-changer for drug testing,” *Pharmaceutics*, vol. 16, no. 4, p. 443, 2024.
- [87] C. N. Mayhew and R. Singhania, “A review of protocols for brain organoids and applications for disease modeling,” *STAR protocols*, vol. 4, no. 1, p. 101860, 2023.
- [88] S. Chae, J. Hong, H. Hwangbo, and G. Kim, “The utility of biomedical scaffolds laden with spheroids in various tissue engineering applications,” *Theranostics*, vol. 11, no. 14, p. 6818, 2021.
- [89] N. Urrestizala-Arenaza, S. Cerchio, F. Cavaliere, and C. Magliaro, “Limitations of human brain organoids to study neurodegenerative diseases: a manual to survive,” *Frontiers in Cellular Neuroscience*, vol. 18, p. 1419526, 2024.
- [90] M. T. Pham, K. M. Pollock, M. D. Rose, W. A. Cary, H. R. Stewart, P. Zhou, J. A. Nolta, and B. Walda, “Generation of human vascularized brain organoids,” *Neuroreport*, vol. 29, no. 7, pp. 588–593, 2018.
- [91] Z. Gan, X. Qin, H. Liu, J. Liu, and J. Qin, “Recent advances in defined hydrogels in organoid research,” *Bioactive Materials*, vol. 28, pp. 386–401, 2023.
- [92] B. Tiemeijer and J. Tel, “Hydrogels for single-cell microgel production: Recent advances and applications,” *Frontiers in Bioengineering and Biotechnology*, vol. 10, p. 891461, 2022.
- [93] N. Seyedhassantehrani, Y. Li, and L. Yao, “Dynamic behaviors of astrocytes in chemically modified fibrin and collagen hydrogels,” *Integrative Biology*, vol. 8, no. 5, pp. 624–634, 2016.

- [94] Z. Liu, S. Mao, Y. Hu, F. Liu, and X. Shao, "Hydrogel platform facilitating astrocytic differentiation through cell mechanosensing and yap-mediated transcription," *Materials Today Bio*, vol. 22, p. 100735, 2023.
- [95] F. Abasalizadeh, S. V. Moghaddam, E. Alizadeh, E. Akbari, E. Kashani, S. M. B. Fazljou, M. Torbat, and A. Akbarzadeh, "Alginate-based hydrogels as drug delivery vehicles in cancer treatment and their applications in wound dressing and 3d bioprinting," *Journal of biological engineering*, vol. 14, pp. 1–22, 2020.
- [96] K. Y. Lee and D. J. Mooney, "Alginate: properties and biomedical applications," *Progress in polymer science*, vol. 37, no. 1, pp. 106–126, 2012.
- [97] H.-J. Kong, K. Y. Lee, and D. J. Mooney, "Decoupling the dependence of rheological/mechanical properties of hydrogels from solids concentration," *Polymer*, vol. 43, no. 23, pp. 6239–6246, 2002.
- [98] K. H. Bouhadir, K. Y. Lee, E. Alsberg, K. L. Damm, K. W. Anderson, and D. J. Mooney, "Degradation of partially oxidized alginate and its potential application for tissue engineering," *Biotechnology progress*, vol. 17, no. 5, pp. 945–950, 2001.
- [99] K. Y. Lee, H. J. Kong, and D. J. Mooney, "Quantifying interactions between cell receptors and adhesion ligand-modified polymers in solution," *Macromolecular bioscience*, vol. 8, no. 2, pp. 140–145, 2008.
- [100] N. B. Erdal, M. Hakkarainen, and A. G. Blomqvist, "Polymers, giant molecules with properties: An entertaining activity introducing polymers to young students," *Journal of Chemical Education*, vol. 96, no. 8, pp. 1691–1695, 2019.
- [101] T. Andersen, P. Auk-Emblem, and M. Dornish, "3d cell culture in alginate hydrogels," *Microarrays*, vol. 4, no. 2, pp. 133–161, 2015.
- [102] P. A. Janmey, J. P. Winer, and J. W. Weisel, "Fibrin gels and their clinical and bioengineering applications," *Journal of the Royal Society Interface*, vol. 6, no. 30, pp. 1–10, 2009.
- [103] J. Brinkmann, H. Malyaran, M. A. A. Enezy-Ulbrich, S. Jung, C. Radermacher, E. M. Buhl, A. Pich, and S. Neuss, "Assessment of fibrin-based hydrogels containing a fibrin-binding peptide to tune mechanical properties and cell responses," *Macromolecular Materials and Engineering*, vol. 308, no. 7, p. 2200678, 2023.
- [104] Q. Ye, G. Zünd, P. Benedikt, S. Jockenhoevel, S. P. Hoerstrup, S. Sakyama, J. A. Hubbell, and M. Turina, "Fibrin gel as a three dimensional matrix in cardiovascular tissue engineering," *European Journal of Cardio-Thoracic Surgery*, vol. 17, no. 5, pp. 587–591, 2000.

BIBLIOGRAPHY

- [105] M. D. Shoulders and R. T. Raines, "Collagen structure and stability," *Annual review of biochemistry*, vol. 78, no. 1, pp. 929–958, 2009.
- [106] S. R. Caliari and J. A. Burdick, "A practical guide to hydrogels for cell culture," *Nature methods*, vol. 13, no. 5, pp. 405–414, 2016.
- [107] J. R. E. Fraser, T. C. Laurent, and U. Laurent, "Hyaluronan: its nature, distribution, functions and turnover," *Journal of internal medicine*, vol. 242, no. 1, pp. 27–33, 1997.
- [108] J. A. Burdick and G. D. Prestwich, "Hyaluronic acid hydrogels for biomedical applications," *Advanced materials*, vol. 23, no. 12, pp. H41–H56, 2011.
- [109] R. J. Pelham Jr and Y.-I. Wang, "Cell locomotion and focal adhesions are regulated by substrate flexibility," *Proceedings of the national academy of sciences*, vol. 94, no. 25, pp. 13 661–13 665, 1997.
- [110] M. P. Lutolf, J. L. Lauer-Fields, H. G. Schmoekel, A. T. Metters, F. E. Weber, G. B. Fields, and J. A. Hubbell, "Synthetic matrix metalloproteinase-sensitive hydrogels for the conduction of tissue regeneration: engineering cell-invasion characteristics," *Proceedings of the National Academy of Sciences*, vol. 100, no. 9, pp. 5413–5418, 2003.
- [111] C.-C. Lin and K. S. Anseth, "Peg hydrogels for the controlled release of biomolecules in regenerative medicine," *Pharmaceutical research*, vol. 26, pp. 631–643, 2009.
- [112] C. E. Vorwald, T. Gonzalez-Fernandez, S. Joshee, P. Sikorski, and J. K. Leach, "Tunable fibrin-alginate interpenetrating network hydrogels to support cell spreading and network formation," *Acta biomaterialia*, vol. 108, pp. 142–152, 2020.
- [113] K. Ma, A. L. Titan, M. Stafford, C. hua Zheng, and M. E. Levenston, "Variations in chondrogenesis of human bone marrow-derived mesenchymal stem cells in fibrin/alginate blended hydrogels," *Acta biomaterialia*, vol. 8, no. 10, pp. 3754–3764, 2012.
- [114] C. Hwang, B. Ay, D. Kaplan, J. Rubin, K. Marra, A. Atala, J. Yoo, and S. Lee, "Assessments of injectable alginate particle-embedded fibrin hydrogels for soft tissue reconstruction," *Biomedical Materials*, vol. 8, no. 1, p. 014105, 2013.
- [115] I. Brito, G. Silva, A. Sales, C. Lobo, G. Rodrigues, R. Sousa, A. Moura, C. Calderón, M. Bertolini, C. Campello *et al.*, "Fibrin–alginate hydrogel supports steroidogenesis, in vitro maturation of oocytes and parthenotes production from caprine preantral follicles cultured in group," *Reproduction in Domestic Animals*, vol. 51, no. 6, pp. 997–1009, 2016.

- [116] X. Bocheng and R. França, “Innovative 3d bioprinting approaches for advancing brain science and medicine: a literature review,” *Biomedical Physics & Engineering Express*, 2024.
- [117] Y. Yan, X. Li, Y. Gao, S. Mathivanan, L. Kong, Y. Tao, Y. Dong, X. Li, A. Bhattacharyya, X. Zhao *et al.*, “3d bioprinting of human neural tissues with functional connectivity,” *Cell Stem Cell*, vol. 31, no. 2, pp. 260–274, 2024.
- [118] S. Naghieh, M. Sarker, N. Sharma, Z. Barhoumi, and X. Chen, “Printability of 3d printed hydrogel scaffolds: Influence of hydrogel composition and printing parameters,” *Applied Sciences*, vol. 10, no. 1, p. 292, 2019.
- [119] S. Wang, L. Bai, X. Hu, S. Yao, Z. Hao, J. Zhou, X. Li, H. Lu, J. He, L. Wang *et al.*, “3d bioprinting of neurovascular tissue modeling with collagen-based low-viscosity composites,” *Advanced Healthcare Materials*, vol. 12, no. 25, p. 2300004, 2023.
- [120] M. Tang, J. N. Rich, and S. Chen, “Biomaterials and 3d bioprinting strategies to model glioblastoma and the blood–brain barrier,” *Advanced Materials*, vol. 33, no. 5, p. 2004776, 2021.
- [121] S. J. Lee, W. Jeong, and A. Atala, “3d bioprinting for engineered tissue constructs and patient-specific models: Current progress and prospects in clinical applications,” *Advanced Materials*, p. 2408032, 2024.
- [122] K. P. Murphy, *Machine learning: a probabilistic perspective*. MIT press, 2012.
- [123] I. Castiglioni, L. Rundo, M. Codari, G. Di Leo, C. Salvatore, M. Interlenghi, F. Gallivanone, A. Cozzi, N. C. D’Amico, and F. Sardanelli, “Ai applications to medical images: From machine learning to deep learning,” *Physica medica*, vol. 83, pp. 9–24, 2021.
- [124] E. Moen, D. Bannon, T. Kudo, W. Graf, M. Covert, and D. Van Valen, “Deep learning for cellular image analysis,” *Nature methods*, vol. 16, no. 12, pp. 1233–1246, 2019.
- [125] E. Meijering, “A bird’s-eye view of deep learning in bioimage analysis,” *Computational and structural biotechnology journal*, vol. 18, pp. 2312–2325, 2020.
- [126] F. Emmert-Streib and M. Dehmer, “Taxonomy of machine learning paradigms: A data-centric perspective,” *Wiley Interdisciplinary Reviews: Data Mining and Knowledge Discovery*, vol. 12, no. 5, p. e1470, 2022.
- [127] S. Uddin, A. Khan, M. E. Hossain, and M. A. Moni, “Comparing different supervised machine learning algorithms for disease prediction,” *BMC medical informatics and decision making*, vol. 19, no. 1, pp. 1–16, 2019.

BIBLIOGRAPHY

- [128] M. J. Zaki and W. Meira Jr, *Data mining and machine learning: fundamental concepts and algorithms*. Cambridge University Press, 2020.
- [129] I. Goodfellow, Y. Bengio, and A. Courville, *Deep learning*. MIT press, 2016.
- [130] S. Russell and P. Norvig, *Artificial Intelligence: A Modern Approach*, 4th ed. Pearson, 2021.
- [131] A. M. Wichert and L. Sa-Couto, *Machine Learning-A Journey to Deep Learning: With Exercises and Answers*. World Scientific, 2021.
- [132] M. Ghafoorian, N. Karssemeijer, T. Heskes, M. Bergkamp, J. Wissink, J. Obels, K. Keizer, F.-E. de Leeuw, B. Van Ginneken, E. Marchiori *et al.*, “Deep multi-scale location-aware 3d convolutional neural networks for automated detection of lacunes of presumed vascular origin,” *NeuroImage: Clinical*, vol. 14, pp. 391–399, 2017.
- [133] J. Long, E. Shelhamer, and T. Darrell, “Fully convolutional networks for semantic segmentation,” in *Proceedings of the IEEE conference on computer vision and pattern recognition*, 2015, pp. 3431–3440.
- [134] M. Weigert, U. Schmidt, R. Haase, K. Sugawara, and G. Myers, “Star-convex polyhedra for 3d object detection and segmentation in microscopy,” in *Proceedings of the IEEE/CVF winter conference on applications of computer vision*, 2020, pp. 3666–3673.
- [135] C. Shorten and T. M. Khoshgoftaar, “A survey on image data augmentation for deep learning,” *Journal of big data*, vol. 6, no. 1, pp. 1–48, 2019.
- [136] R. Kijowski, F. Liu, F. Caliva, and V. Pedoia, “Deep learning for lesion detection, progression, and prediction of musculoskeletal disease,” *Journal of magnetic resonance imaging*, vol. 52, no. 6, pp. 1607–1619, 2020.
- [137] A. Hamidinekoo, E. Denton, A. Rampun, K. Honnor, and R. Zwiggelaar, “Deep learning in mammography and breast histology, an overview and future trends,” *Medical image analysis*, vol. 47, pp. 45–67, 2018.
- [138] C. McQuin, A. Goodman, V. Chernyshev, L. Kamentsky, B. A. Cimini, K. W. Karhohs, M. Doan, L. Ding, S. M. Rafelski, D. Thirstrup *et al.*, “Cellprofiler 3.0: Next-generation image processing for biology,” *PLoS biology*, vol. 16, no. 7, p. e2005970, 2018.
- [139] Oxford Instruments, “Imaris software,” Jan 2025, version 9.6.0. [Online]. Available: <https://imaris.oxinst.com>

- [140] S. Berg, D. Kutra, T. Kroeger, C. N. Straehle, B. X. Kausler, C. Haubold, M. Schiegg, J. Ales, T. Beier, M. Rudy *et al.*, “Illastik: interactive machine learning for (bio) image analysis,” *Nature methods*, vol. 16, no. 12, pp. 1226–1232, 2019.
- [141] P. Barbier de Reuille, A.-L. Routier-Kierzkowska, D. Kierzkowski, G. W. Bassel, T. Schüpbach, G. Tauriello, N. Bajpai, S. Strauss, A. Weber, A. Kiss *et al.*, “Morphographx: A platform for quantifying morphogenesis in 4d,” *elife*, vol. 4, p. e05864, 2015.
- [142] F. Xing, Y. Xie, H. Su, F. Liu, and L. Yang, “Deep learning in microscopy image analysis: A survey,” *IEEE transactions on neural networks and learning systems*, vol. 29, no. 10, pp. 4550–4568, 2017.
- [143] N. J. Allen and C. Eroglu, “Cell biology of astrocyte-synapse interactions,” *Neuron*, vol. 96, no. 3, pp. 697–708, 2017.
- [144] O. Russakovsky, J. Deng, H. Su, J. Krause, S. Satheesh, S. Ma, Z. Huang, A. Karpathy, A. Khosla, M. Bernstein, A. C. Berg, and L. Fei-Fei, “Imagenet large scale visual recognition challenge,” *International Journal of Computer Vision (IJCV)*, vol. 115, no. 3, pp. 211–252, 2015.
- [145] H. Wang, S. Shang, L. Long, R. Hu, Y. Wu, N. Chen, S. Zhang, F. Cong, S. Lin *et al.*, “Biological image analysis using deep learning-based methods: literature review,” *Digital Medicine*, vol. 4, no. 4, p. 157, 2018.
- [146] K. Simonyan and A. Zisserman, “Very deep convolutional networks for large-scale image recognition,” *arXiv preprint arXiv:1409.1556*, 2014.
- [147] K. He, X. Zhang, S. Ren, and J. Sun, “Deep residual learning for image recognition,” in *Proceedings of the IEEE conference on computer vision and pattern recognition*, 2016, pp. 770–778.
- [148] A. Pratapa, M. Doron, and J. C. Caicedo, “Image-based cell phenotyping with deep learning,” *Current opinion in chemical biology*, vol. 65, pp. 9–17, 2021.
- [149] W. J. Godinez, I. Hossain, S. E. Lazic, J. W. Davies, and X. Zhang, “A multi-scale convolutional neural network for phenotyping high-content cellular images,” *Bioinformatics*, vol. 33, no. 13, pp. 2010–2019, 2017.
- [150] C. Sommer, R. Hoefler, M. Samwer, and D. W. Gerlich, “A deep learning and novelty detection framework for rapid phenotyping in high-content screening,” *Molecular biology of the cell*, vol. 28, no. 23, pp. 3428–3436, 2017.
- [151] N. Pawlowski, J. C. Caicedo, S. Singh, A. E. Carpenter, and A. Storkey, “Automating morphological profiling with generic deep convolutional networks,” *BioRxiv*, p. 085118, 2016.

BIBLIOGRAPHY

- [152] A. Gupta, P. J. Harrison, H. Wieslander, N. Pielawski, K. Kartasalo, G. Partel, L. Solorzano, A. Suveer, A. H. Klemm, O. Spjuth *et al.*, “Deep learning in image cytometry: a review,” *Cytometry Part A*, vol. 95, no. 4, pp. 366–380, 2019.
- [153] R. Girshick, J. Donahue, T. Darrell, and J. Malik, “Rich feature hierarchies for accurate object detection and semantic segmentation,” in *Proceedings of the IEEE conference on computer vision and pattern recognition*, 2014, pp. 580–587.
- [154] S. Ren, K. He, R. Girshick, and J. Sun, “Faster r-cnn: Towards real-time object detection with region proposal networks,” *Advances in neural information processing systems*, vol. 28, 2015.
- [155] R. Girshick, “Fast r-cnn,” in *Proceedings of the IEEE international conference on computer vision*, 2015, pp. 1440–1448.
- [156] J. Redmon, S. Divvala, R. Girshick, and A. Farhadi, “You only look once: Unified, real-time object detection,” in *Proceedings of the IEEE conference on computer vision and pattern recognition*, 2016, pp. 779–788.
- [157] J. Terven and D. Cordova-Esparza, “A comprehensive review of yolo: From yolov1 to yolov8 and beyond,” *arXiv preprint arXiv:2304.00501*, 2023.
- [158] S. S. A. Zaidi, M. S. Ansari, A. Aslam, N. Kanwal, M. Asghar, and B. Lee, “A survey of modern deep learning based object detection models,” *Digital Signal Processing*, vol. 126, p. 103514, 2022.
- [159] F. Sadak, M. Saadat, and A. M. Hajiyavand, “Real-time deep learning-based image recognition for applications in automated positioning and injection of biological cells,” *Computers in Biology and Medicine*, vol. 125, p. 103976, 2020.
- [160] I. Suleymanova, T. Balassa, S. Tripathi, C. Molnar, M. Saarma, Y. Sidorova, and P. Horvath, “A deep convolutional neural network approach for astrocyte detection,” *Scientific reports*, vol. 8, no. 1, p. 12878, 2018.
- [161] C. B. Kayasandik, W. Ru, and D. Labate, “A multistep deep learning framework for the automated detection and segmentation of astrocytes in fluorescent images of brain tissue,” *Scientific reports*, vol. 10, no. 1, p. 5137, 2020.
- [162] G. Jocher, A. Chaurasia, and J. Qiu, “Yolo by ultralytics,” Jan 2023. [Online]. Available: <https://github.com/ultralytics/ultralytics>
- [163] S. J. A. Nugraha and B. Erfianto, “White blood cell detection using yolov8 integration with detr to improve accuracy,” *Sinkron: jurnal dan penelitian teknik informatika*, vol. 8, no. 3, pp. 1908–1916, 2023.

- [164] L. Leyendecker, J. Haas, T. Piotrowski, M. Frye, C. Becker, B. K. Fleischmann, M. Hesse, and R. H. Schmitt, “A modular deep learning pipeline for cell culture analysis: Investigating the proliferation of cardiomyocytes,” in *International Conference on Medical Imaging with Deep Learning*. PMLR, 2022, pp. 760–773.
- [165] X.-X. Yin, L. Sun, Y. Fu, R. Lu, Y. Zhang *et al.*, “U-net-based medical image segmentation,” *Journal of Healthcare Engineering*, vol. 2022, 2022.
- [166] L.-C. Chen, G. Papandreou, I. Kokkinos, K. Murphy, and A. L. Yuille, “Deeplab: Semantic image segmentation with deep convolutional nets, atrous convolution, and fully connected crfs,” *IEEE transactions on pattern analysis and machine intelligence*, vol. 40, no. 4, pp. 834–848, 2017.
- [167] Y. Wang, U. Ahsan, H. Li, M. Hagen *et al.*, “A comprehensive review of modern object segmentation approaches,” *Foundations and Trends® in Computer Graphics and Vision*, vol. 13, no. 2-3, pp. 111–283, 2022.
- [168] V. Badrinarayanan, A. Kendall, and R. Cipolla, “Segnet: A deep convolutional encoder-decoder architecture for image segmentation,” *IEEE transactions on pattern analysis and machine intelligence*, vol. 39, no. 12, pp. 2481–2495, 2017.
- [169] T. Tran, O.-H. Kwon, K.-R. Kwon, S.-H. Lee, and K.-W. Kang, “Blood cell images segmentation using deep learning semantic segmentation,” in *2018 IEEE international conference on electronics and communication engineering (ICECE)*. IEEE, 2018, pp. 13–16.
- [170] J. Daniel, J. Rose, F. Vinnarasi, and V. Rajinikanth, “Vgg-unet/vgg-segnet supported automatic segmentation of endoplasmic reticulum network in fluorescence microscopy images,” *Scanning*, vol. 2022, 2022.
- [171] O. Ronneberger, P. Fischer, and T. Brox, “U-net: Convolutional networks for biomedical image segmentation,” in *Medical Image Computing and Computer-Assisted Intervention–MICCAI 2015: 18th International Conference, Munich, Germany, October 5-9, 2015, Proceedings, Part III 18*. Springer, 2015, pp. 234–241.
- [172] U. Schmidt, M. Weigert, C. Broaddus, and G. Myers, “Cell detection with star-convex polygons,” in *Medical Image Computing and Computer Assisted Intervention–MICCAI 2018: 21st International Conference, Granada, Spain, September 16-20, 2018, Proceedings, Part II 11*. Springer, 2018, pp. 265–273.
- [173] Ö. Çiçek, A. Abdulkadir, S. S. Lienkamp, T. Brox, and O. Ronneberger, “3d u-net: learning dense volumetric segmentation from sparse annotation,” in *Medical Image Computing and Computer-*

BIBLIOGRAPHY

- Assisted Intervention–MICCAI 2016: 19th International Conference, Athens, Greece, October 17–21, 2016, Proceedings, Part II 19.* Springer, 2016, pp. 424–432.
- [174] C. Stringer, T. Wang, M. Michaelos, and M. Pachitariu, “Cellpose: a generalist algorithm for cellular segmentation,” *Nature methods*, vol. 18, no. 1, pp. 100–106, 2021.
 - [175] M. Pachitariu and C. Stringer, “Cellpose 2.0: how to train your own model,” *Nature methods*, vol. 19, no. 12, pp. 1634–1641, 2022.
 - [176] D. Eschweiler, R. S. Smith, and J. Stegmaier, “Robust 3d cell segmentation: extending the view of cellpose,” in *2022 IEEE International Conference on Image Processing (ICIP)*. IEEE, 2022, pp. 191–195.
 - [177] Y. Liu, Y. Jin, E. Azizi, and A. J. Blumberg, “Cellstitch: 3d cellular anisotropic image segmentation via optimal transport,” *BMC bioinformatics*, vol. 24, no. 1, p. 480, 2023.
 - [178] F. Isensee, P. F. Jaeger, S. A. Kohl, J. Petersen, and K. H. Maier-Hein, “nnu-net: a self-configuring method for deep learning-based biomedical image segmentation,” *Nature methods*, vol. 18, no. 2, pp. 203–211, 2021.
 - [179] K. He, G. Gkioxari, P. Dollár, and R. Girshick, “Mask r-cnn,” in *Proceedings of the IEEE international conference on computer vision*, 2017, pp. 2961–2969.
 - [180] D. J. E. Waibel, S. Shetab Boushehri, and C. Marr, “Instantdl: an easy-to-use deep learning pipeline for image segmentation and classification,” *BMC bioinformatics*, vol. 22, pp. 1–15, 2021.
 - [181] T. Sugimoto, H. Ito, Y. Teramoto, A. Yoshizawa, and R. Bise, “Multi-class cell detection using modified self-attention,” in *Proceedings of the IEEE/CVF Conference on Computer Vision and Pattern Recognition*, 2022, pp. 1855–1863.
 - [182] O. Petit, N. Thome, C. Rambour, L. Themyr, T. Collins, and L. Soler, “U-net transformer: Self and cross attention for medical image segmentation,” in *Machine Learning in Medical Imaging: 12th International Workshop, MLMI 2021, Held in Conjunction with MICCAI 2021, Strasbourg, France, September 27, 2021, Proceedings 12*. Springer, 2021, pp. 267–276.
 - [183] Y. Gao, M. Zhou, and D. N. Metaxas, “Utnet: a hybrid transformer architecture for medical image segmentation,” in *Medical Image Computing and Computer Assisted Intervention–MICCAI 2021: 24th International Conference, Strasbourg, France, September 27–October 1, 2021, Proceedings, Part III 24*. Springer, 2021, pp. 61–71.
 - [184] F. Isensee, T. Wald, C. Ulrich, M. Baumgartner, S. Roy, K. Maier-Hein, and P. F. Jaeger, “nnu-net revisited: A call for rigorous validation in 3d medical image segmentation,” in *International*

Conference on Medical Image Computing and Computer-Assisted Intervention. Springer, 2024, pp. 488–498.

- [185] S. Atwell, D. J. E. Waibel, S. S. Boushehri, S. Wiedenmann, C. Marr, and M. Meier, “Label-free imaging of 3d pluripotent stem cell differentiation dynamics on chip,” *Cell Reports Methods*, vol. 3, no. 7, 2023.
- [186] D. J. E. Waibel, U. Tiemann, V. Lupperger, H. Semb, and C. Marr, “In-silico staining from bright-field and fluorescent images using deep learning,” in *Artificial Neural Networks and Machine Learning–ICANN 2019: Image Processing: 28th International Conference on Artificial Neural Networks, Munich, Germany, September 17–19, 2019, Proceedings, Part III 28.* Springer, 2019, pp. 184–186.
- [187] C. Heinrich, S. Gascón, G. Masserdotti, A. Lepier, R. Sanchez, T. Simon-Ebert, T. Schroeder, M. Götz, and B. Berninger, “Generation of subtype-specific neurons from postnatal astroglia of the mouse cerebral cortex,” *Nature protocols*, vol. 6, no. 2, pp. 214–228, 2011.
- [188] M. Kowal, M. Skobel, A. Gramacki, and J. Korbicz, “Breast cancer nuclei segmentation and classification based on a deep learning approach,” *International Journal of Applied Mathematics and Computer Science*, vol. 31, no. 1, pp. 85–106, 2021.
- [189] P. Jevtić, L. J. Edens, L. D. Vuković, and D. L. Levy, “Sizing and shaping the nucleus: mechanisms and significance,” *Current opinion in cell biology*, vol. 28, pp. 16–27, 2014.
- [190] M.-A. P. Bray, W. J. Adams, N. A. Geisse, A. W. Feinberg, S. P. Sheehy, and K. K. Parker, “Nuclear morphology and deformation in engineered cardiac myocytes and tissues,” *Biomaterials*, vol. 31, no. 19, pp. 5143–5150, 2010.
- [191] G. Kleinberg, S. Wang, E. Comellas, J. R. Monaghan, and S. J. Shefelbine, “Usability of deep learning pipelines for 3d nuclei identification with stardist and cellpose,” *Cells & Development*, vol. 172, p. 203806, 2022.
- [192] J. C. Caicedo, A. Goodman, K. W. Karhohs, B. A. Cimini, J. Ackerman, M. Haghghi, C. Heng, T. Becker, M. Doan, C. McQuin *et al.*, “Nucleus segmentation across imaging experiments: the 2018 data science bowl,” *Nature methods*, vol. 16, no. 12, pp. 1247–1253, 2019.
- [193] K. D. Vos, “Cell counter plugin for imagej,” 2010. [Online]. Available: <https://imagej.net/ij/plugins/cell-counter.html>
- [194] L. Yang and A. Shami, “On hyperparameter optimization of machine learning algorithms: Theory and practice,” *Neurocomputing*, vol. 415, pp. 295–316, 2020.

BIBLIOGRAPHY

- [195] S. Galarza, A. J. Crosby, C. Pak, and S. R. Peyton, “Control of astrocyte quiescence and activation in a synthetic brain hydrogel,” *Advanced healthcare materials*, vol. 9, no. 4, p. 1901419, 2020.
- [196] B. L. LeSavage, N. A. Suhar, C. M. Madl, and S. C. Heilshorn, “Production of elastin-like protein hydrogels for encapsulation and immunostaining of cells in 3d,” *Journal of Visualized Experiments: Jove*, no. 135, p. 57739, 2018.
- [197] C. T. Rueden, M. C. Hiner, E. L. Evans III, M. A. Pinkert, A. M. Lucas, A. E. Carpenter, B. A. Cimini, and K. W. Eliceiri, “Pyimagej: A library for integrating imagej and python,” *Nature methods*, vol. 19, no. 11, pp. 1326–1327, 2022.
- [198] H. D. napari Work, “Napari: A multidimensional image viewer for python a guide to some of the key concepts of napari,” Dec. 2024. [Online]. Available: <https://github.com/napari/napari>



Key Resources Table

Table A.1: Complete list of materials and chemicals.

REAGENT or RESOURCE	SOURCE	IDENTIFIER
Antibodies and dyes		
Chicken anti-GFAP	Aves Labs	Cat# GFAP, RRID: AB_2313547
Rabbit anti-SOX9	Sigma-Aldrich	Cat# AB5535, RRID: AB_2239761
Anti-chicken goat, Alexa Fluor 647	Invitrogen	Cat# A-21449, RRID: AB_2535866
Anti-rabbit donkey, Alexa Fluor 594	Invitrogen	Cat# A-21207, RRID: AB_141637
Chemicals, peptides and recombinant proteins		
MVG GRGDSP	Sigma-Aldrich	Cat# 4270501
VLVG GRGDSP	Sigma-Aldrich	Cat# 4270101
Fibrinogen, bovine plasma	Sigma-Aldrich	Cat# 341573-16
Aprotinin, bovine lung	Roche	Cat# 10236632103
Thrombin, bovine plasma	Sigma-Aldrich	Cat# T4648-1KU
Calcium Chloride dihydrate	Sigma-Aldrich	Cat# 223506
DMEM/F12	GIBCO	Cat# 11320033
Fetal Bovine Serum (FBS)	PAN BIOTECH	Cat# P30-3302

Continued on next page

A. KEY RESOURCES TABLE

Table A.1 – continued from previous page

REAGENT or RESOURCE	SOURCE	IDENTIFIER
Trypsin/EDTA	GIBCO	Cat# 25300054
D-(+)-Glucose	Sigma-Aldrich	Cat# G8769
GlutaMAX	GIBCO	Cat# 35050061
Penicillin-Streptomycin (P/S)	GIBCO	Cat# 15140122
B27	GIBCO	Cat# 17504044
HEPES	GIBCO	Cat# 15630080
HBSS	GIBCO	Cat# 14025092
Bovine Serum Albumine (BSA)	Sigma-Aldrich	Cat# A2153
Triton X-100	Sigma-Aldrich	Cat# T9284
Propidium Iodide 20X	Invitrogen	Cat# BMS500PI
Calcein-AM	BD Pharmingen	Cat# 564061
Poly-D-Lysine Hydrobromide	Sigma-Aldrich	Cat# P6407
Trypan blue	Thermo Fisher	Cat# 15250061
Culture plates and materials		
μ-plate 24 well	IBIDI	Cat# 82426
Silicone sheet	Electron Microscopy Sciences	Cat# 70338-05
Dialysis membrane	Spectrum Laboratories	Cat# 15370752
Experimental models: Mice lines		
WT mice		
Actin::GFP mice		
Software		
ZEN Software	Carl Zeiss	RRID:SCR_013672
Black ZEN Software	Carl Zeiss	RRID:SCR_018163
Leica Application Suite X (LAS-X)	Leica Microsystems	RRID:SCR_013673
Fiji	N/A	RRID:SCR_002285
Cell Counter Plugin for ImageJ	N/A	RRID:SCR_025376

B

Additional Methods

B.1 PDL Coating

Glass coverslips in 24-well plates or glass-bottom 24-well plates were incubated in standard conditions (37°C, 5% CO₂) with 0.5 mL of PDL coating solution (1x PBS, 2% PDL). The incubation was carried out for a period of either 120 minutes or overnight, depending on the specific experimental requirements.

After the incubation, the wells were washed three times with distilled water to remove any unbound PDL. The plates were then allowed to dry for 20 minutes at 22°C, room temperature, under a laminar flow hood, ensuring that the coated surface was dry but not exposed to any contaminants.

Once dry, the coated 24-well plates were carefully stored at -4°C to preserve the PDL coating until they were required for further use. Proper storage conditions at low temperature help maintain the integrity of the PDL coating over time.

B.2 Fabrication of Glass-bottom Silicone Mini-wells

To facilitate hydrogel casting and subsequent analysis using an upright confocal microscope (LSM710 laser-scanning confocal, Carl Zeiss), glass-bottom silicon mini-wells with a 5 mm diameter were manually fabricated, as previously described in [196]. The fabrication process commenced with the preparation of silicone sections from silicone sheets measuring $130 \times 180 \times 0.5$ mm (Electron Microscope Sciences). These sheets were cut into 0.8×0.8 mm² squares. Using a punch tool with 5 mm diameter, the mini-well structure was created by perforating centrally each silicone square (Figure B.1). The silicone sections and 12 mm diameter glass cover slips were surface-treated in a plasma cleaner (Harrick Plasma PDC001HP) for 2 minutes. This surface activation facilitated bonding between the silicone and glass components, which were pressed together immediately after plasma cleaning. To strengthen the bond, the assembled mini-wells underwent thermal treatment by baking at 80 °C for 90 minutes. Following the baking process, the mini-wells were autoclaved to ensure sterility and then stored at -4 °C until needed for further use.

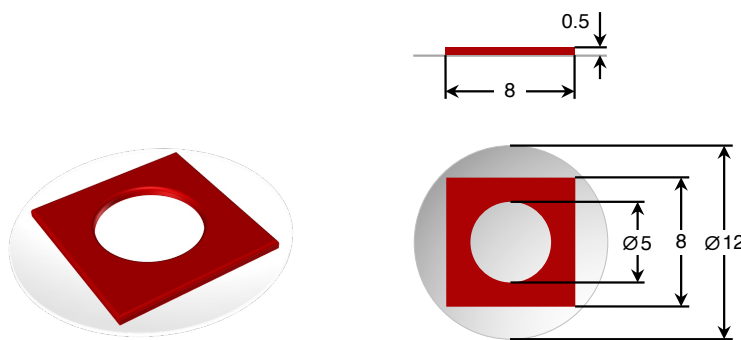
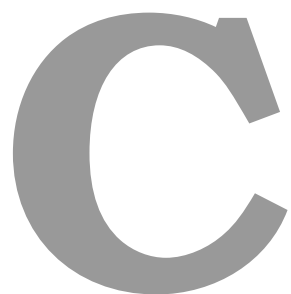


Figure B.1: Technical drawing of mini-well construction. In grey is represented the glass cover slip, Ø 12 mm, and in red the silicone sheet. Units mm.



GUI User Guide

The GUI was developed in Python and is available in a GitHub repository. The repository is intended to create a user-friendly and clean code for GUI generation to be used by biologists to do proper image annotation.

Table C.1: Comparison of the functionalities in *GUI v1.0* and *GUI v2.0*.

Features	<i>GUI v1.0</i>	<i>GUI v2.0</i>
Image visualization	✓	✓
Bounding boxes loading from .csv	✓	✓
Bounding boxes visualization	✓	✓
Semiautomatic prediction of expression markers	✓	✓
Export of data as .csv	✓	✓
Improved interface	✗	✓
Load image specific .csv	✗	✓
Manual addition of missing instances	✗	✓
Supported image types	.tif	.tif and .czi
Stability	stable	performance bugs

The version available in the repository does not have yet all the functionalities listed in Section 5.2 functional. Nevertheless, is the most stable version created to the date. Moreover the functionalities comparison between *GUI v1.0* – the one available – and *GUI v2.0* – the one previously described – is as listed in Table C.1.

C.1 Instalation

The instalation of the package requires loading from the GitHub repository through the command line. The installation follow four simple steps: **(1)** Opening the command line, **(2)** Cloning the repository from GitHub, **(3)** Installing requirements in a new environment (making sure to have conda installed), and **(4)** Runing the app. A detailed step-by-step guide is demonstrated on Listing C.1.

Listing C.1: Step-by-step guided instalation.

```
1      # Cloning repository
2      git clone -b dev-beatriz https://github.com/Amirhk-devBounding-Box-Validator-
         for-Fluorescence-Images.git
3      cd Bounding-Box-Validator-for-Fluorescence-Images
4
5      # Installing requirements
6      conda create --name bb-validator python=3.9
7      conda activate bb-validator
8      pip install -r requirements.txt
9
10     # running the app
11     cd Main
12     python bounding\boxes\validation.py
```

C.2 Usage

After the first instalation, the GUI can simply be run by activating its environment and running the main script as illustrated on Listing C.2.

Once the main window is open, select the mode **Astrocyte** (deprecated on *GUI v2.0*), and load an image to analyse (.tif extension). Since in the *GUI v1.0* the interface is loaded with the correspondent bounding boxes file (.csv), there is no need to load this file as well. Furthermore, the images need to be stored in a specific format, within a dataset, for apropiate data loading.

Listing C.2: Step-by-step to run the GUI after the first instalation.

```
1 conda activate bb-validator
2 cd Bounding-Box-Validator-for-Fluorescence-Images/Main
3 git pull
4 python bounding_boxes_validation.py
```

A dataset is characterized by the fluorescent markers used for the staining. On the other hand, the image sizes and type (int8, int16) can vary within the dataset. The images must always be saved in a dataset folder which follows the following nomenclature:

[DATASET NAME]_[MARKER_1]_[...]_[MARKER_N].

Thus, the name of the folder of a group of images stained with GFAP, SOX9 and DAPI should be named DATASET001_GFAP_SOX9_DAPI. The folder structure should be as in Listing C.3.

Listing C.3: Dataset folder structure.

```
1 DATASET001_GFAP_SOX9_DAPI/
2   |-- images/
3     |-- image_1.tif
4     |-- image_2.tif
5     |-- ...
6     |-- image_n.tif
```

To annotate the image, simply click on *Show Bounding Boxes Version* and begin. Each cell instance has a unique set of labels. Each instance should be annotated individually. After finishing all annotations click on *Finish/Save*.

To export the results of the annotations, go to the directory where you have made the instalation. The results are saved under:

.../Results/Morphology_results/nunet/detected_regions_on_all_images.csv.

C.3 Shortcuts

A number of shortcuts was created within the GUI to guarantee ease of use and efficiency in data annotation process. *GUI v2.0* includes additional shortcuts for faster image inspection and annotation.

C. GUI USER GUIDE

On Table C.2 are comprised their functionalities and sequence.

Table C.2: Shortcuts for *GUI v1.0* and *GUI v2.0*.

Features	<i>GUI v1.0</i>	<i>GUI v2.0</i>
Load Image	l	N/A
Bounding Boxes Window	b	N/A
Next/Previous Layer	n / p	< / >
Next/Previous Instance	d / a	SHIFT + < / SHIFT + >
Navigate Markers	N/A	SPACE key
Change Marker Label	N/A	ENTER key

D

Additional Methods for Nuclei Segmentation

D.1 Dataset Processing and Annotation for Baseline Solution

D.1.1 Image Processing using Fiji

The images underwent preprocessing using Fiji [31] via an automated pipeline designed to diminish background noise and fine-tune contrast levels (Figure D.1A). This preprocessing pipeline was scripted with Python, using version 2.14.0 of the Fiji python package, pyimagej [197]. Preprocessing serves as a crucial step in preparing the images for manual annotation, which is essential for training our models effectively. However, our end goal is to enable advanced deep learning models to independently extract valuable features straight from the raw images. Ultimately, we aim to empower these models to discern and utilize critical patterns and information without relying on preprocessing steps.

The initial steps of the preprocessing pipeline involve splitting the color channels and normalizing the histograms. This process effectively doubles the original dataset, creating two distinct sets of images,

D. ADDITIONAL METHODS FOR NUCLEI SEGMENTATION

each corresponding to a specific wavelength. Meanwhile, considering the inherent limitations of depth imaging in 2D cultures, an analysis to address the diminishing fluorescent signal in function of the depth was conducted. Previous works undertook a similar assessment of wavelength-dependent intensity decay concerning imaging depth, by computing the relative average fluorescence intensity (RAFI) across varying depths [185]. By assuming that the average image intensity should remain consistent with imaging depth, they derived the imaging-depth decay rate using linear regression and subsequently applied the necessary correction.

In this project, the RAFI was determined by comparing the average signal intensity (measured in the 8 bit scale) at a particular depth with the minimum average signal intensity of the cell culture. The findings indicated an absence of a significant decay trend illustrated by the overall low variance of slices mean intensity per stack (Figure D.1B and D.1C). Overall, the mean RAFI of the DAPI channel was 1.218 ± 0.049 and the mean RAFI of the GFAP channel was 1.353 ± 0.268 . These results lead to the conclusion that no adjustments were required for the signal intensity.

Optimal contrast is achieved through histogram analysis of each z-stack, wherein minimum and maximum pixel values for the images are set. Through the global analysis of the dataset histogram, it is noticeable that the data is shifted towards lower intensities and high intensity pixels are less frequent (Figure D.1D and D.1E). The assessment of individual image histograms revealed heterogeneity across the dataset. Therefore, for accurate analysis, the contrast adjustment has to be performed manually for each image. It is important to note that contrast adjustments do not necessarily alter pixel values but optimize the visual spectrum (Figure D.1F and D.1G). Consequently, this step is not mandatory for the preprocessing phase and was reserved solely for image annotations.

To suppress high frequencies in the image and minimizing spatial spread, there were also applied filters to the image. In a trial preprocessing approach there were only tested the mean and the bidimensional Gaussian filters, with radius, r , or standard deviation, σ , equal to 1 pixel, respectively (Figures D.1H and D.1I). Changing the filters' parameters can also serve as a potential data augmentation strategy to expand the training dataset for further analysis. However, this procedure must be approached cautiously to prevent blurring of low-intensity nuclei.

Depending on the learning task that is being addressed, some configurations of input training images might be more suitable than others. To prepare the training datasets for the proposed tasks, four different datasets were built: two for 2D and two for 2D analysis (Table D.1). The tridimensional images encompass one z-stack of only the DAPI channel (*3d nuclei* dataset), and one composite of the GFAP and DAPI channels (*3d composite* dataset). The *3d nuclei* dataset will be used to assess nuclei specific characteristics, such as cell nuclei count and cell nuclei volume. On the other hand, the *3d composite* dataset will be useful for quantifying astrocyte related characteristics such as astrocyte count, astrocyte type classification, multinucleated astrocyte state classification, and attemptitively the astrocyte territory.

D.1 DATASET PROCESSING AND ANNOTATION FOR BASELINE SOLUTION

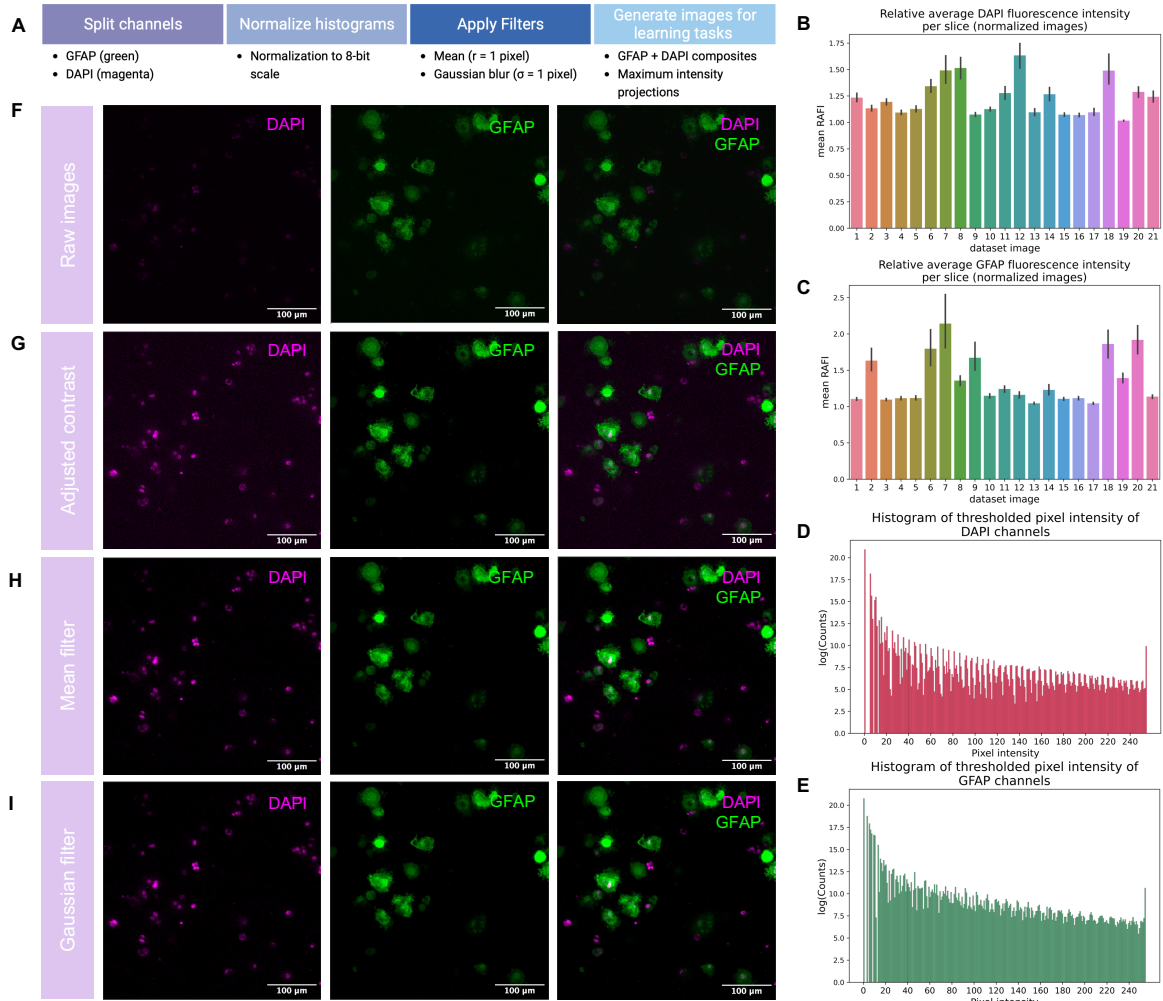


Figure D.1: Fiji preprocessing. **(A)** Fiji preprocessing pipeline to adjust contrast, apply filters, and obtain final input images for each learning task; **(B)** Mean of the relative average DAPI fluorescence intensity calculated per slice in normalized images; **(C)** Mean of the relative average GFAP fluorescence intensity calculated per slice in normalized images; **(D)** Histogram of the logarithm of the sum of all images pixels in DAPI channel; **(E)** Histogram of the logarithm of the sum of all images pixels in GFAP channel; **(F)** Raw maximum intensity projections of image 2; **(G)** Raw maximum intensity projections of image 2 with adjusted contrast; **(H)** Maximum intensity projection after the application of the mean filter ($r = 1$ pixel) to image 2; **(I)** Maximum intensity projection after the application of the gaussian filter ($\sigma = 1$ pixel) to image 2.

For the 2D analysis, there were performed maximum intensity projections of the 2D datasets. Every resulting preprocessed image was manually validated to guarantee the correct preprocessing.

D.1.2 2D Nuclei Segmentation

The nuclei segmentation was performed manually in the maximum intensity projection images of the DAPI channel, the *2d nuclei* dataset (Figure D.2A). The segmentation was performed using the Fiji's free hand selection tool (Figure D.2B), after contrast adjustment in the maximum intensity projections.

D. ADDITIONAL METHODS FOR NUCLEI SEGMENTATION

Table D.1: Annotation and description of the secondary datasets obtained from the original dataset through channel selection and maximum intensity projection manipulations.

Dataset	Annotation	Description
<i>2d nuclei</i>	Nuclei instance and semantic segmentation using Fiji free hand selection tool.	Manually annotated maximum intensity projection of the DAPI channel for segmentation tasks.
<i>3d nuclei</i>	Nuclei instance and semantic segmentation using Fiji free hand selection tool.	Manually annotated z-stacks of the DAPI channel for 2D segmentation tasks.
<i>2d composite</i>	Classification labels regarding the type of cell (astrocyte or not), astrocyte type, and the multinucleated state.	Manually annotated maximum intensity projection of composite images of DAPI and GFAP channels.
<i>3d composite</i>	Classification labels regarding the type of cell (astrocyte or not), astrocyte type, and the multinucleated state.	Manually annotated z-stack composites images of DAPI and GFAP channels.

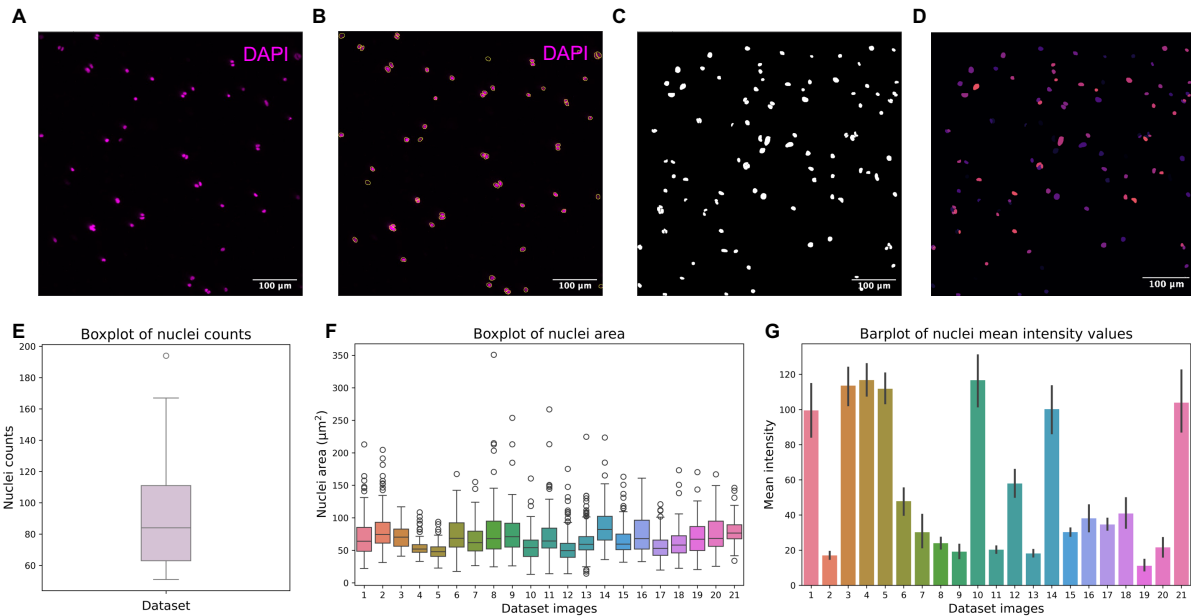


Figure D.2: 2D nuclei profiling and statistics. **(A)** Maximum intensity projection of image 11 from the *2d nuclei* dataset; **(B)** Manual segmentation of nuclei using Fiji using the hand selection tool; **(C)** Semantic segmentation resulting from the manual segmentation using Fiji; **(D)** Instance segmentation resulting from the manual segmentation using Fiji; **(E)** Boxplot of nuclei counts over the entire dataset; **(F)** Boxplot of nuclei area, in μm^2 , for each image in the dataset; **(G)** Barplot of nuclei mean intensity values, using the mean as estimator.

The number of masks obtained are equivalent to the number of nuclei present in each image, and therefore encompass a straightforward method to count the number of cells in each image.

The masks obtained are fed to the learning networks to compare its predictions to the groundtruth and fine-tune the learning model as well as to assess the models' performance on a testing set. After manually segmenting the nuclei, a semantic segmentation mask (Figure D.2C) can be accessed, as well as individual instance segmentation masks (Figure D.2D).

Given the resulting masks, consider the following statistics pertaining to the nuclei characteristics across images. Over the 21 images, a total of 2034 nuclei were identified, giving an average of approximately 96.86 nuclei per image. However, the standard deviation is quite high, with a value of 42.12, which illustrates the high heterogeneity of cell density across the images. Furthermore, median number of nuclei per image is 84 supporting that most images have lower cell counts, however there are a few that deviate substantially from the mean. A candidate outlier, image 13, was also identified, presenting a cell count of 194 (Figure D.2E).

On the other hand, the segmented nuclei area as an approximately stable median value around $69.05 \mu\text{m}^2$. However, there could be identified several outliers across the images (Figure D.2F). This can be caused by the misclassification of the segmentation masks resulting from the difficulty of identifying the nuclei borders in some instances. Analysing the mean intensity values of the segmented nuclei of each image, its perceptible the high contrast heterogeneity across images (Figure D.2G).

D.2 3D Nuclei Segmentation and Preparation for nnU-Net Input

Napari [198], a Python-based interactive visualization tool, was employed for image segmentation. The software was installed via pip, ensuring all necessary dependencies were met. The StarDist 2D plugin, specifically designed for nuclei segmentation, is integrated into Napari, with its instalation through the Napari's plugin manager.

The DAPI channel images were imported into Napari through the graphical interface and an initial segmentation was conducted using the StarDist 2D plugin, which generates instance-labeled images. To each nuclei segmentation was assigned a unique color-label ranging from 1 to N, corresponding to individual nuclei. The background represented as 0.

After completing all the nuclei segmentation annotations, the segmented images were postprocessed to adhere to the label conventions required by nnU-Net, which requires semantic labeling instead of instance labeling performed with Napari. For this, on a first step, the boundaries were delineated using a morphological dilation followed by subtraction. There was used a dilatation of 3 pixels on every X, Y, Z directions. Afterwards, the image was further reformatted into a label map with the following encoding: 0 – background, 1 – nuclei boundary, and 2 – nuclei interior. A different notation might have been chosen here. Finally, the final processed images were saved in the .nii.gz format, compatible with nnU-Net.

